Graphenised Lithium Iron Phosphate and Lithium Manganese Silicate Hybrid Cathode Systems for Lithium-Ion Batteries

UNIVERSITY *of the*
WESTERN CAPE

By

Zolani Myalo

(BSc Honours, Cum Laude)

A mini-thesis submitted in partial fulfilment of the requirements for the degree of

Magister Scientiae in Nanoscience

Faculty of Natural Science

University of the Western Cape

Bellville, Cape Town, South Africa

Supervisor: Dr. Chinwe Ikpo

Co-supervisor: Prof. Emmanuel Iwuoha

December 2017

Graphenised Lithium Iron Phosphate and Lithium Manganese Silicate Hybrid Cathode Systems for Lithium-Ion Batteries

Keywords

Energy

Lithium Ion Batteries

Cathode

Hybrid Cathode

Lithium Iron Phosphate

Lithium Manganese Orthosilicate

Graphene Nanosheets

Sol-Gel Synthesis

Cyclic Voltammetry

Electrochemical Impedance Spectroscopy

Abstract

Graphenised Lithium Iron Phosphate and Lithium Manganese Silicate Hybrid Cathode Systems for Lithium-Ion Batteries

Zolani Myalo

MSc Nanoscience mini-thesis, Department of Chemistry, University of the Western Cape

December 2017

This research was based on the development and characterization of graphenised lithium iron phosphate-lithium manganese silicate ($LiFePO_4$-Li_2MnSiO_4) hybrid cathode materials for use in Li-ion batteries. Although previous studies have mainly focused on the use of a single cathode material, recent works have shown that a combination of two or more cathode materials provides better performances compared to a single cathode material. The $LiFePO_4$-Li_2MnSiO_4 hybrid cathode material is composed of $LiFePO_4$ and Li_2MnSiO_4. The Li_2MnSiO_4 contributes its high working voltage ranging from 4.1 to 4.4 V and a specific capacity of 330 mA h g^{-1}, which is twice that of the $LiFePO_4$ which, in turn, offers its long cycle life, high rate capacity as well as good electrochemical and thermal stability. The two cathode materials complement each other's properties however they suffer from low electronic conductivities which were suppressed by coating the hybrid material with graphene nanosheets. The synthetic route entailed a separate preparation of the individual pristine cathode materials, using a sol-gel protocol. Then, the graphenised $LiFePO_4$-Li_2MnSiO_4 and $LiFePO_4$-Li_2MnSiO_4 hybrid cathodes were obtained in two ways: the hand milling (HM) method where the pristine cathodes were separately prepared and then mixed with graphene using a pestle and mortar, and the *in situ* sol-gel (SG) approach where the Li_2MnSiO_4 and graphene were added into the $LiFePO_4$ sol, stirred and calcined together. These materials were characterized using various microscopic, spectroscopic, thermogravimetric and electrochemical techniques. The pristine $LiFePO_4$ and Li_2MnSiO_4 cathodes both had spherical nanoparticles with particle sizes of 20 and 25 ηm, respectively. The $LiFePO_4$ showed better thermal stability indicated by only 8 % weight loss compared to 18 % of Li_2MnSiO_4 which can be attributed to the presence of the strong covalent bond between P-O in the $[PO_4]^n$ unit. The graphene nanosheets were successfully prepared from graphene oxide as confirmed by the reduced number of nanosheets observed in HRTEM and HRSEM, and the shifting of the D and G bands to lower frequencies indicated by Raman studies of this material. The slightly bell shaped peak of the pair-distance distribution function (PDDF) curves from small angle scattering X-ray

technique confirmed spherical shaped nanoparticles with diameters of 36, 30, 37 and 23 ηm corresponding to $LiFePO_4$-Li_2MnSiO_4 HM, graphenised $LiFePO_4$-Li_2MnSiO_4 HM, $LiFePO_4$-Li_2MnSiO_4 SG and graphenised $LiFePO_4$-Li_2MnSiO_4 SG, respectively. These finding are evidence that the presence of graphene in the graphenised samples helped to decrease particle sizes in these samples. The $LiFePO_4$-Li_2MnSiO_4 SG hybrid cathode showed the smallest particle size and this is attributed to the better mixing offered by the sol-gel method. Electrochemical studies using cyclic voltammetry showed that all the prepared hybrid cathodes had three peaks attributed to the oxidation and reduction pair of manganese and a reduction peak of iron in 1.0 M $LiClO_4$ electrolyte. The graphenised samples showed higher currents which is associated with improved capacities of these materials compared to those without graphene. The graphenised $LiFePO_4$-Li_2MnSiO_4 HM and $LiFePO_4$-Li_2MnSiO_4 HM hybrid cathodes had specific capacities of 3.408 and 2.804 mA h g^{-1} compared to those of 2.524 and 4.056 mA h g^{-1} corresponding to graphenised $LiFePO_4$-Li_2MnSiO_4 SG and $LiFePO_4$-Li_2MnSiO_4 SG, respectively. The results showed better performance of the hybrid cathodes prepared by the *in situ* sol-gel approach. However, the hand mill-prepared graphenised $LiFePO_4$-Li_2MnSiO_4 and $LiFePO_4$-Li_2MnSiO_4 hybrid cathodes showed fast diffusion of Li-ions with diffusion coefficients of 1.574 x 10^{-12} and 2.450 x 10^{-13} cm^2 s^{-1}, respectively compared to those of the graphenised $LiFePO_4$-Li_2MnSiO_4 (1.529 x 10^{-13} cm^2 s^{-1}) and $LiFePO_4$-Li_2MnSiO_4 (7.547 x 10^{-13} cm^2 s^{-1}) prepared using the *in situ* sol-gel approach. Finally, EIS studies revealed that these materials have a capacitive behaviour indicated by the inclined line of the Nyquist plot without a depressed semicircle in the high frequency region.

Declaration

I hereby declare that "*Graphenised Lithium Iron Phosphate and Lithium Manganese Silicate Hybrid Cathode Systems for Lithium-Ion Batteries*" is my own work, that it has not been submitted for any degree or examination in any other university, and that all the sources I have used or quoted have been indicated and acknowledged by complete references.

Full name : Zolani Myalo Date December 2017

Signed : 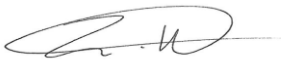

Dedication

This work is dedicated to my beloved parents; Mr Mxolisi Patrick Myalo and Ms Nombulelo Mcutha for their continued love and support. Finally to my son Qhawe Ayola Myalo, "you are my hero and inspiration to achieve greatness".

Acknowledgements

"God is good all the time, and all the time God is good" Indeed He is because I am where I am today not because of my liking but because of His favour upon me.

I wish to express my sincere appreciation to my research supervisor, Dr. Chinwe Ikpo for her guidance, wisdom, mentorship and patient instructions throughout my research. I truly appreciate the love and support that she had shown me.

I convey a special gratitude to my co-supervisor Prof. Emmanuel Iwuoha for his guidance, encouragement and the wonderful opportunity to be part of SensorLab research group.

To all the members of staff in the Chemistry department, thank you so much for your encouragement and support. I would like to express my deepest appreciation to Prof. Farouk Ameer for his words of wisdom and mentorship since my second year as a student in the Department. "Your wise words and teaching will always be highly appreciated". To Dr Rachel Ajayi, "thank you for encouraging me to be a well-rounded person and continue with my involvement in student development programmes".

To my newly found family, SensorLab research group: I am grateful for the support and encouragement from all the senior researchers: Dr Tesfaye Waryo, Dr Milua Masikini, Dr Natasha Ross, Dr Meryck Ward, Dr Francis Muya, Dr Lindsay Wilson, Dr Usisipho Feleni, Dr Unathi Sidwaba, Dr Lisebo Phelane and Sinazo Qakala. A special thanks goes to my mentors: Ezo Nxusani, Wonderboy Hlongwa and Miranda Ndipingwi. Research is challenging, but you have always taught me to look on the positive side.

To the 2016 Nanoscience class: I will always honour and cherish the memorable moments that we've shared together especially the challenging ones in the lab/classroom, because they have united and kept us going.

I would like to thank all my family members, especially my mom Nombulelo Mcutha and dad Mxolisi Patrick Myalo for their prayers and continued love which gave me the energy to keep going at all times. To my aunts, Nondumiso Myalo and Nomfazi Mcutha thank you for your encouragements. To my brothers and sisters, Mphilisi Myalo, Siseko Myalo, Sikelela Myalo, Ntando Myalo, Sakhumzi Mcutha and Vuyisile Mcutha, and Pumla Myalo, Pheliswa Myalo, Onele Myalo, Ncebakazi Myalo, Onke Myalo, Yonela Mcutha and Sivuyisiwe Mcutha, "thank you for believing in me". A big thanks to my friends, Sikhangele Rozani and Nikuxolo Chiliza for being there for me at all times. Finally, to my sweetheart, Ncebakazi

Mazwi, “thank you for being my source of happiness and being there for me throughout this journey. I would have not come this far without your love and support.”

I would also like to acknowledge the Nanoscience and Nanotechnology Postgraduate Teaching and Training Platform (NNPTTP) at the University of the Western Cape for accepting me into the programme, constant support and encouragement. Finally this research, the research exposure and trainings attended would not have been possible without the financial support from the Department of Science and Technology.

Table of Contents

Acronyms and Abbreviations

Li-ion	Lithium Ion
XRD	X-ray Diffraction
HRSEM	High Resolution Scanning Electron Microscopy
HRTEM	High Resolution Transmission Electron Microscopy
EDS	Energy Dispersive X-ray Spectroscopy
FTIR	Fourier Transform Infrared Spectroscopy
TGA	Thermogravimetric Analysis
SAXS	Small Angle X-ray Scattering
CV	Cyclic Voltammetry
EIS	Electrochemical Impedance Spectroscopy
HM	Hand Milling Method
SG	Sol-Gel Method
LFP	$LiFePO_4$/Lithium Iron Phosphate
LMS	Li_2MnSiO_4/Lithium Manganese Silicate
LFP-LMS	$LiFePO_4$-Li_2MnSiO_4 Hybrid Cathode
LFP-LMS-G	Graphenised $LiFePO_4$-Li_2MnSiO_4 Hybrid Cathode

List of Figures

List of Tables

CHAPTER 1

Chapter Overview

This chapter is an introduction laying the background behind this study. It starts by outlining the dependency of the global community for its energy production on non-renewable fossil fuels and some of the disadvantages associated with these energy sources. In addition, the need for an adjustment from the use of fossil fuels to renewable energy sources is also outlined in this chapter. However, renewable energy sources are intermittent and unreliable. In line with that, electrochemical energy storage devices are highlighted as a possible technology that can help promote and sustain the use of renewable sources. The literature presented in this chapter focuses on Li-ion batteries, specifically its cathode materials, their advantages, limitations and some of the avenues that can be used to improve their shortcomings. The last section of this chapter highlights the aim of this work and the research objectives needed to achieve this aim.

1. Introduction

1.1. Background: Energy and Environmental Crisis - the greatest challenge facing mankind

A greater portion of the world's energy consumption comes from the use of fossil fuels. These fossil fuels (coal, natural gas and oil) have to be burnt in order to produce consumable energy which is usually in the form of fuel or electricity. Although this energy is needed to make our day-to-day activities easier, the required conversion reactions that are used to retrieve energy from the carbon that is contained/stored in fossil fuels often result into the production of greenhouse gasses such as carbon dioxide (CO_2), nitrogen oxides (NOx) and sulphur oxides (SOx) which ultimately steer to global warming [1]. On the list of commonly used fossil fuels, coal emits the highest amount of CO_2 which then makes it the biggest contributor of greenhouse gasses into the atmosphere [2]. Even more dangerous is methane,

another by-product of coal which has more environmental side effects than CO_2 with a global warming potential factor that is 21 times greater than that of CO_2 shown by studies projected over a period of 100 years [2, 3]. Livestock farming has become one of the fast growing contributors of this gas which is caused by the worldwide increased production from this sector.

In 2005, the world power consumption was 13 terawatts (TW) which is equivalent to 87 million barrels of oil [1]. Figure 1A shows that 81 % of the world's energy consumed in 2005 came from fossil fuels and the remaining 19 % was shared amongst renewable energy sources and nuclear energy. In 2010, the world's energy consumption remained the same as it was in 2005 (Fig. 1 B) [4]. These findings show the lack of improvement in terms of the energy sector trying to balance the distribution in the usage amongst the different sources of energy. South Africa is amongst other countries that are still trailing behind with the implementation of renewable energy sources and are still continuing to build more coal-fired power stations [5]. There is a negative impact associated with energy production being focused only on non-renewable fossil fuels, as these are the main producers of greenhouse gases and ultimately global warming [2].

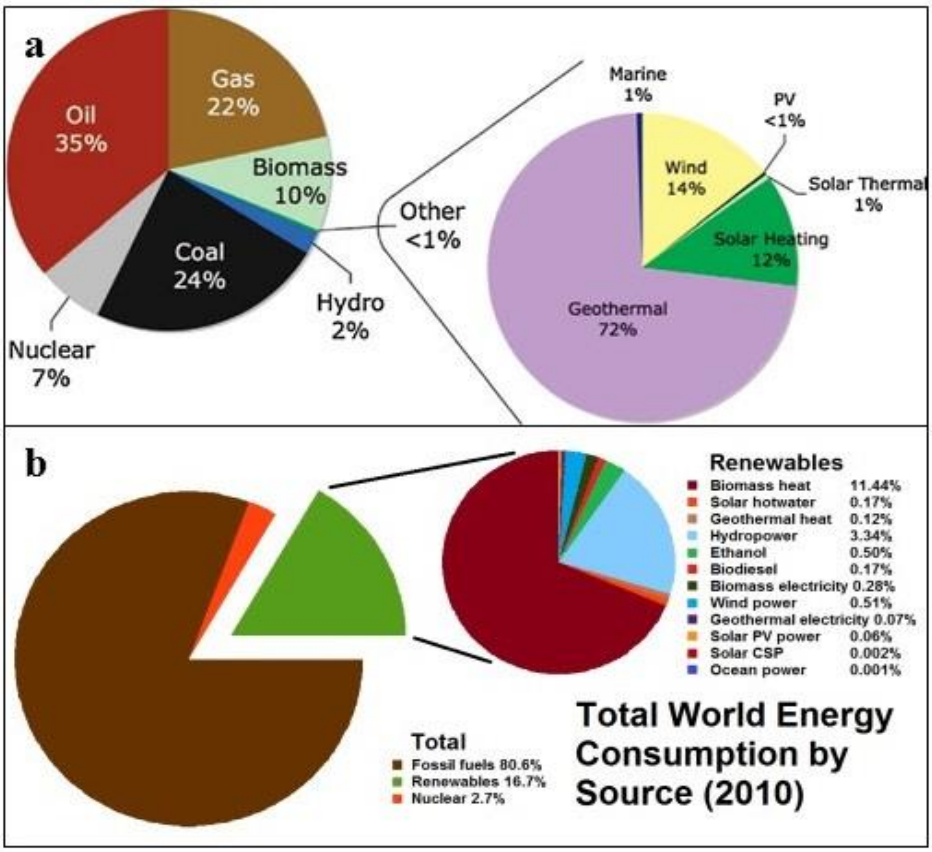

Figure 1: World energy consumption by source for the year (a) 2005 and (b) 2010

The global community is currently concerned about the continual/steady centralization of energy production that is mainly focused on fossil fuels. Climate change and the frequent occurrence of environmental hazards (e.g. landslides, melting of ice caps, drought, etc…) are alarming issues that every nation cannot ignore. Over the past decades, climate has changed drastically as evidenced by the increase in global temperatures. Consequently, this has caused melting of ice-caps which has threatened a number of aquatic species whose lives are now in danger of being extinct [6]. In addition, the burning of fossil fuels has caused acid rain through emission of sulphur and nitrogen oxides, which has damaged buildings and forests, and has contaminated water bodies [7]. Furthermore, fly-ash is another dangerous pollutant. It contains heavy metals (e.g. U, Hg, Pb, Cd, As, etc…) which pollutes the air and poses serious health risks to humans and marine life. There are also some heavy metals that are non-biodegradable, hence they do accumulate on the food chain over time and become carcinogenic to human beings [8].

The transportation sector is a very huge industry and another major contributor towards air pollution. Although there might be few exceptions to this, generally almost all modes of transport contribute towards pollution into the environment. This problem originates from the type of fuel that is being used to power these machines [9]. According to historical records the very first vehicles were powered by steam engines. These were then followed by internal combustion engines and later electric vehicles, all developed in this particular order. The introduction of electric vehicles into the market in 1890 was warmly welcomed [10, 11]. This type of car was popular because they emitted less noise, were cleaner and more economic than other types of vehicles. Hence, they dominated the road transportation sector during this period of time.

However, this dominance was short-lived due to the revolution of science and technology in the car manufacturing industry in the year 1908 [11]. The knowledge, brought by the two, promised to bring solutions to the world's problems through the improvement of available resources in order to produce materials that would suit the needs of the world's population. In addition, it triggered people to desire fast and affordable cars which would enable them to transport and trade goods from one location to another. At about this period in time, one of the leading internal combustion vehicle manufacturers started to improve their engines and concurrently reduced the costs in the process. This led investors in the manufacturing industry to fund this technology. Consequently, the electric and steam engine powered vehicles could not compete with the technology and they trailed behind the combustion vehicles.

Tourism records have shown that amongst other forms of transport, the introduction of fast-moving cars has contributed enormously on people's mobility from one country to another as well as within their regions [12, 13]. This has helped to improve tourism as well as trading partnerships on a global scale. However, the increasing number of vehicles on the road has been a fundamental cause of major environmental issues; such as traffic jams that are associated with noise pollution and emission of greenhouse gases (e.g. CO_2, traces of CO, NO_x, $H_2O_{(g)}$ and C_xH_y) which causes air pollution and contributes towards the greenhouse effect. These gases absorb and trap infrared radiation, therefore forming a blanket that prevents radiation from escaping the earth's atmosphere leading to gradual increase of the earth's average temperatures. These processes cause drastic environmental issues: for

example droughts, climate change, heavy rains and floods which have threatened the lives of many species [13].

The above-mentioned environmental issues that the global community faces are the results of activities made by humans who, in the process of attempting to address their basic needs, have instead triggered them. An example for this is the use of fossil fuels to generate energy for human consumption which has led to the occurrence of natural disasters, waste disposals resulting in water and air pollution. Moreover, the use of fossil fuels is done at a much faster rate than the earth can regenerate them due to fast growing human population [14]. The latter is a pressing issue that needs serious intervention in order reduce the strain on natural resources as the world population is currently at 7.5 billion from 6.6 billion in 2007 [15, 16].

The reserves for fossil fuels are being slowly depleted, therefore putting pressure on researchers to come up with urgent solutions so that the world does not run-out of energy supply [5]. An appealing alternative to this predicament is the use of renewable energy sources (such as wind, solar, geothermal and hydropower) to create a balance in energy supply both from fossil fuels and renewable energy sources [17, 18]. The advantages of renewable energy production are that not only they generate little-to-no greenhouse gases during harvest, but they also benefits future generations as the technology is sustainable and provides employment opportunities and energy security for the country [19].

South Africa has a great potential to benefit from renewable energy sources. Most provinces in the country receive on average not less than 2 500 hours of solar radiation per year, and the radiation energy provided ranges between 4.5 to 6.5 kW h m^{-2} per day [20]. However, the development of hydropower plants has been quite slow due to water scarcity coupled with the fact that most provinces are not suitable for generating this energy, except Eastern Cape and KwaZulu Natal [20]. These two provinces have potential to develop hydropower plants that can provide an estimated power of about 10 MW of energy.

Furthermore, the wind levels are fairly reasonable and also reliable to generate large amounts of energy especially along the coastline of the Eastern and Western Cape provinces. These winds are coming from the oceans and, as they blow towards the continent, they create waves which can be used to generate wave power [7, 20, 21]. Some of these technologies are still in

their early stages of development and are showing great potential to solve energy problems in certain provinces in South Africa. Investing in these technologies will benefit these provinces in a number of ways; such as creating employment opportunities and also meeting the energy needs.

Even though renewable energy sources are greener and environmentally friendly their feasibility and/or practicability has raised a lot of concerns such as (i) the small amount of energy that they produce, (ii) cost implications associated with the technology and its installation, (iii) their intermittent nature and, (iv) geographical constraints [18, 22]. These challenges are the main reasons behind the slow implementation of renewable energy sources because most developed countries are not ready to move away from the use of fossil fuels. These may not be compatible with greener technologies; however their high power density gives them a competitive advantage over renewable energy sources [23]. Global competitiveness is another factor that causes the slow implementation of renewable energy resources in such a way that countries promote more production and less expenditure in order to ensure a stable and sturdy economy [24].

In the case of coal-rich countries like South Africa, the challenge lies in their energy policies which favour the use of coal over the development of renewable energy sources. South Africa does not have a well-conceived strategy in terms of energy security. Hence, the energy production is dominated by the coal-fired power plants which make 70% of its primary energy sources, and more than 93% of electricity production is generated mainly from coal [5]. As a consequence, South Africa has been ranked as one of the leading emitters of greenhouse gases in the midst of developing and developed countries in the world [5, 18, 25]. Changes in the energy sector can be brought about by developing well-conceived strategies that can be adopted and implemented in order to move away from the use of fossil fuels. Therefore, such strategies must include a form of energy which is sustainable to benefit future generations. Thus far, renewable energy sources are likely to be the only sustainable source of energy that can be used as a potential solution to the current challenges**.**

1.1.1. The Essence for Energy Storage

Indeed, renewable energy sources form part of a sustainable energy source, however they are not reliable due to their intermittent nature [26]. Hence, there is a further need for energy storage systems that will capture and store the energy produced by these sources during their most effective hours of the day. For example these storage systems can be used to store energy produced by solar panels during the day and later used in the evening in the absence of sunlight which serves as a primary source of energy. The advantage of having such systems would help prioritise and make renewable energy sources a reliable source of energy. A success into this technology would result in better electricity facilities for the developing countries and an improved standard of living for citizens [26-28].

At the same time pursuing this technology will also benefit developed countries in the following ways: (i) reduction of fuel consumption for energy production, (ii) provision of security for energy supply and (iii) reduction of environmental hazards as these energy sources are known to be greener [22, 29]. However, the full transition from traditional fossil fuels into renewable energy sources has been slowed down by the fact that fossil fuels have a high power density as opposed to renewable energy sources. Table 1 compares the power densities of commonly used renewable and non-renewable energy sources. It can be observed that the power density of fossil fuels is approximately 100 times higher than most of these renewable energy sources [23, 29].

Table 1: Power densities of commonly used energy sources

Fuel	**Power Density (W m^{-2})**
Non-renewable	
Gas	200 – 2 000
Coal	100 – 1 000
Renewable	
Solar (concentrating)	4 – 10
Solar (PV)	4 – 9
Wind	0.5 – 1.5
Wood	0.5 – 0.6

Electrochemical energy storage systems, amongst other storage systems are being developed to ensure a safer transition from non-renewable to renewable energy powered systems [26]. Part of this transition involved the search for low cost, safe, environmentally friendly and sustainable materials that can be used to make or incorporated into these energy systems [26, 28]. This field of research has attracted a lot of interest because of the capability of these systems to reduce energy costs and, in some cases, be used as primary energy sources [30]. This vision is going to take some times to realise, but a starting point is the application of these systems in small devices which do not require high power densities. As research that focuses on power density progresses, they can be slowly introduced into other applications that require energy sources with high power density.

1.1.2. Electrochemical Energy Storage

Renewable energy sources are limited to certain parts of the world and this makes it difficult to transport the produced energy to other regions that need energy supply. This process is

challenging because the generated energy needs conversion, storage into a different form of energy and then transportation [22, 26, 31]. Various systems (such as mechanical, thermal, magnetic, chemical and electrochemical) have been developed to simplify the transportation issues with energy generated from these energy sources [13, 30].

Electrochemical energy storage devices (for example rechargeable batteries and supercapacitors) have been the focus of interest because they are portable and at the same time can be assembled into large stacks. These devices can store energy in stand-alone electricity grids which, in turn, can provide easy access to energy in remote areas [32]. In addition, their development is also driven by the fast growing use of electronic devices as well as electric and hybrid-electric vehicles. However, despite the significant growth in this technology over the last decade, their energy density and power density, and lifespan needs to be improved [33].

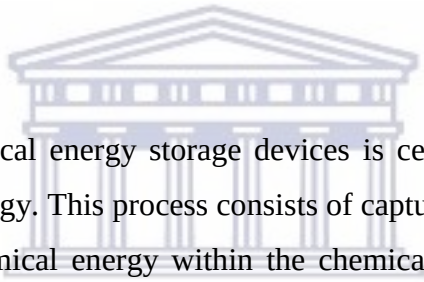

The interest into electrochemical energy storage devices is centred on their simplicity and convenient way of storing energy. This process consists of capturing and converting electrical energy, and storing it as chemical energy within the chemical bonds of the electrodes. In order to use this energy (during peak hours), the chemical energy is spontaneously converted back to electricity without applying heat or any other form of energy [26, 34, 35]. This principle is only applicable to rechargeable batteries and supercapacitors. Fuel cells on the other hand are slightly different because they are not electrochemical energy storage devices, but rather electrochemical energy conversion devices. In a typical battery or supercapacitor the chemical components (electrode materials) that store and release the energy are kept inside the device, whereas in a fuel cell the electrode materials are also inside the device, but the fuel is supplied from an external source [36, 37].

Although these electrochemical energy storage devices may be different in their storage and conversion abilities, they all have two electrodes immersed in an electrolyte solution. Thus, their redox reactions are the same. The negative electrode produces electrons which flow through the external circuit to the positive electrode. Simultaneously, the positive electrode produces cations which diffuse through the electrolyte into the negative electrode in order to produce electricity [36, 37].

Rechargeable batteries are one of the oldest technologies used for storing chemical energy. The energy is converted and produced in the form of electrical energy. Storing is achieved through charging processes, whereas the energy is produced via discharge processes taking place in these devices. These reactions occur without causing any harmful emissions or noises [13].

Various rechargeable batteries have been developed for different applications. These include matured lead-acid, nickel-based, sodium-sulphur and the fast growing lithium-ion batteries [38]. The Li-ion batteries are considered to be the most advantageous storage devices for large-scale applications, because of their light weight, durable cycle-life, wide temperature range, environmentally benign, low self-safety discharge rates, no memory effect and higher out-put power compared to other rechargeable batteries [34, 39]. They are the most used in portable electronics and, at the same time, are being gradually incorporated into electric and hybrid-electric vehicles. Their advantages have contributed largely towards their usage in many other devices.

1.2. Lithium ion (Li-ion) Batteries

Li-ion batteries are well-known for revolutionising the communication and transportation industries, which are the world's great and fast changing industries. The communication industry has produced one of the finest and super-slim smartphones, while the transportation industry has made tremendous progress on hybrid and electric vehicles that can travel reasonable distances [40]. These industries are still promising to offer more sophisticated technologies such as flexible smartphones and autonomous (self-driven) vehicles. Their small size, light weight, high energy density, longer cycle life and non-memory effect are some of the qualities that give Li-ion batteries a cutting edge over the rest [40, 41]. The application of these batteries is not only limited to electronics and electric vehicles, they have also started spreading into power tools and stationary power grid storage applications [42].

Furthermore, Li-ion batteries are recognised for their high energy density which ranges from 150 to over 200 W h kg^{-1} and a cell potential of 3.7 V [26]. The use of Li-ions gives these

batteries a fundamental advantage over its counterparts. Li-ion is the lightest and smallest charged ion with a molecular weight and density of 6.94 g mol^{-1} and 0.53 g m^{-3}, respectively [43]. These factors contribute towards the battery's high gravimetric and volumetric capacity. In addition, Li-ion has the most negative reduction potential (Li^+/Li = -3.04 V) which contributes towards the possibility of higher potentials in all Li-ion batteries. Furthermore, the low molecular weight of this metal contributes towards its high electrochemical capacity of 3.86 A h g^{-1} [43, 44]. Finally, a battery's energy capacity is a product of its voltage and capacity therefore it is clear from the above mentioned properties that Li-ion batteries will offer improved energy density.

A typical Li-ion battery is made up of three components; the anode (negative electrode), cathode (positive electrode) and a conducting electrolyte, which enables ion transfer between these electrodes [45]. These batteries operate on a principle of intercalation and de-intercalation of Li-ions between the two electrodes in the presence of an electrolyte which serves as a conducting medium for these ions [46] as shown in Fig. 2. The positive electrode is usually a lithiated metal oxide (such as $LiCoO_2$) which allows extraction and insertion of Li-ions [26, 47]. On the other hand, the negative electrode is usually made-up of carbon layered compounds such as graphite (C_6) which serves as a host for guest Li-ions [48]. Finally, the electrolyte can be a liquid, gel or solid polymer, and the majority of Li-ion batteries make use of liquid/aqueous electrolytes that are made up of lithium salts dissolved in a mixture of organic solvents [26].

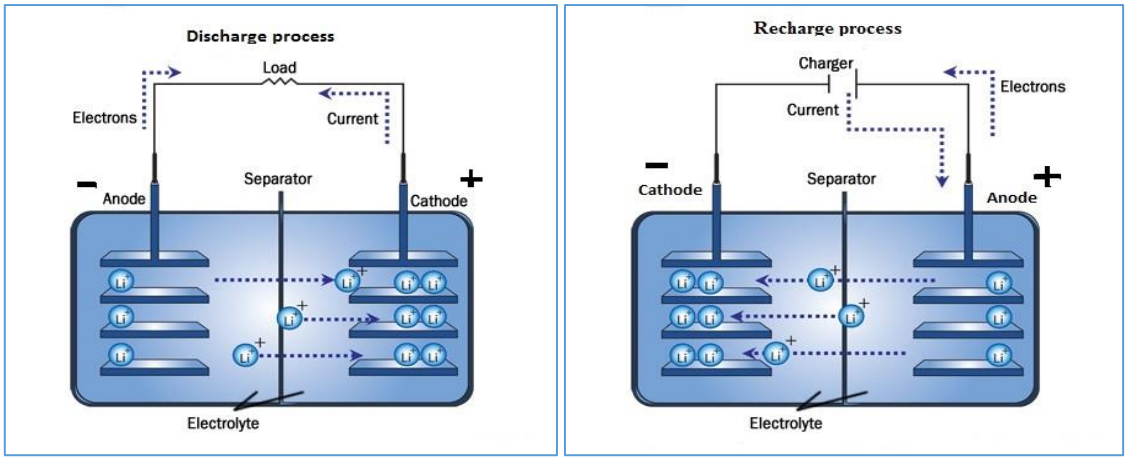

Figure 2: The operating principle of Li-ion batteries is depicted by intercalation/de-intercalation process of Li-ions between the two electrodes immersed in a conducting electrolyte medium (image taken from [49])

Figure 2 illustrates the operating principle of Li-ion batteries. When the battery is in use (during discharge) it is in a galvanic cell mode and electrons spontaneously flow via the external circuit from the negative (anode) to positive (cathode) electrodes. Simultaneously, Li-ions diffuse through the electrolyte in the same direction to complete the circuit [48] as it is illustrated by Equation 1. The current on the other hand flows in the opposite direction. In this process the negative electrode serves an electron source and undergoes oxidation (anodic reaction) [36].

The entire process is reversed when the battery is being charged and the reactions are non-spontaneous. Therefore, the battery is operating in an electrolytic cell mode. The convention used during discharge also changes when the battery undergoes discharge, therefore the anode becomes the cathode and the cathode becomes the anode. However, the positive electrode remains the positive electrode and the negative electrode remains the negative electrode [50]. The electrons flow from the positive electrode to reduce the negative electrode as indicated by Equation 2. The battery serves as an energy storage device and the energy supplied from an external source is stored and reserved for future use [46, 51].

Anode reaction:

$$Li_xC_6 \underset{\text{Charge}}{\overset{\text{Discharge}}{\rightleftharpoons}} xLi^+ + xe^- + C_6 \quad (1)$$

Cathode reaction:

$$Li_{1-x}CoO_2 + xLi^+ + xe^- \underset{\text{Charge}}{\overset{\text{Discharge}}{\rightleftharpoons}} LiCoO_2 \quad (2)$$

Cell reaction:

$$LiC_6 + CoO_2 \underset{\text{Charge}}{\overset{\text{Discharge}}{\rightleftharpoons}} LiCoO_2 + C_6 \quad (3)$$

(where $0 < x \leq 1$) and the overall reaction (Equation 3) lead to potentials between 3.6 and 4.0 V at room temperature [52, 53].

1.3. Components of Li-ion batteries

Li-ion batteries are very diverse compared to other rechargeable batteries; they make use of a range of electrodes and electrolyte materials which some will be reviewed in this chapter [29]. Some of these materials are already available in the market and are used in a vast range of applications, however others are still at their development stages [54].

1.3.1. Electrolytes

An electrolyte is generally referred to as a solution made up of a salt (s) dissolved in a solvent to impact ionic conductivity. Electrolytes play a crucial role of linking the negative and positive electrodes and also facilitate the transfer of charged ions between these electrodes [54]. For any material to qualify as an electrolyte it must show feasible stability against the electrodes and remain inert during operation. Other characteristics include: (i) a large electrochemical window to allow less electrolyte degradation within the working potential range of both the negative and positive electrodes; (ii) it must be an electronic insulator (σ_e $<10^{-10}$ S cm^{-1}) with good ionic conductivity ($\boldsymbol{\sigma_{Li}}$ $>10^{-4}$ S cm^{-1}) to prevent electron transport and allow facile ion (Li-ion in the case of Li-ion batteries) transport; (iii) be thermally stable, in the case of liquid electrolytes their melting and boiling points should be outside the operating temperatures; (iv) be of low toxicity and low cost; (v) preferably non-flammable and non-explosive if short-circuited and (vi) must be based on sustainable chemistries so that it is easy to produce and the production process in environmentally friendly [54].

There is a variety of electrolytes used in Li-ion battery research and industry. They include: (i) aqueous electrolytes - made up of lithium salts which are dissolved in water; (ii) non-aqueous electrolytes - these consist of lithium salts dissolved in an organic (or mixture of organic and inorganic) solvent; (ii) ionic liquids - mainly organic salts with an added lithium salt; (iv) polymer electrolytes – is described as a thick gel or solid polymer electrolyte that is made-up of polymers and lithium salts and (v) hybrid electrolytes – are nanocomposites derived from organic and inorganic materials or ionic liquids combined with nanoparticles [54-56]. Each electrolyte offers a unit set of properties which allows them to function at different conditions (such as temperature) for different battery applications.

Aqueous electrolytes have received a lot of attention since the development of aqueous Li-ion batteries by Li, McKinnon and Dahn [54, 57, 58]. The interest towards these materials is caused by their low cost and non-flammable nature which makes them safer than other electrolytes [57, 59]. In addition, they also offer high ionic conductivities (about two orders of magnitude higher than those of the organic electrolytes) which result to high power operation [60, 61]. The use of water to dissolve lithium salts for these electrolytes is essential

to reduce their cost. However, water has a narrow electrochemical stability window (1.23 V) which has a negative impact on the application of these electrolytes in aqueous Li-ion batteries [54, 59]. The simplicity and low cost of these electrolytes makes them a preferred choice for use in Li-ion battery research [62].

Lithium perchlorate ($LiClO_4$) was the preferred electrolyte in this study because of its low cost and tendency to form highly conductive electrolyte solutions more especially when dissolved in alkyl carbonate solvents. This electrolyte has been one of widely used electrolytes in battery research due to its high solubility when dissolved in aprotic solvents, high ionic conductivity, and high thermal and electrochemical stabilities [62]. $LiClO_4$ electrolyte is not yet commercialized in Li-ion battery applications due to the formation of its highest oxidation state of Cl^{VII} which makes it a very strong oxidising agent and dangerous explosive [62, 63]. Even though that might be the case, this material remains one of the best and popularly used electrolytes for Li-ion battery research.

1.3.2. Anodes

Many Li-ion batteries feature graphitic carbon as their anode material. This in no surprise because this material has good electrical conductivity, large reversible Li-ion storage properties and is relatively easy to produce [64]. However, there are some challenges that the material is faced with such as its low specific capacity (372 mA h g^{-1}) and a sluggish performance which affect the overall battery performance [64]. Li-ion batteries are anticipated to power high-power tools (such as electric and hybrid electric vehicles) and to support the use of renewable energy sources. This has triggered a search for alternative materials or additives to be incorporated into the existing graphite material. As such, materials like metal alloys (Li_xM, where M = In, Si, Pb or Sn) [65], metal oxides (SnO_2, FeO, NiO and CoO) [66] and graphite derivatives have emerged as potential anode materials for Li-ion batteries [64].

Metal alloys offer much higher specific capacity (> 1000 mA h g^{-1}) compared to graphitic carbon, but the challenge with these anodes is that they undergo drastic volume changes

during the intercalation/de-intercalation processes of Li-ions. These changes results to cracking and total structural distraction of the material which is followed by severe capacity fade [65, 66]. Indeed these materials offer pleasant specific capacities, but their feasibility is limited by the weak structure. Therefore, controlling the morphology in these materials seems to address the issue of structural defects, but their cycling behaviour remains unsatisfactory. Furthermore, incorporating electrochemically active nanoparticles into these materials is a promising strategy to stabilise the cyclic behaviour [65].

On the other hand, the introduction of metal oxides has also reduced some of the challenges encountered with metal alloys as they tend to be more stable during insertion/extraction of Li-ions. When a metal oxide such as SnO_2 is negatively polarised it undergoes an irreversible reaction (Equation 4) which results to the formation of metal Sn particles floating in the Li_2O matrix [65]. The Li_2O surrounding Sn particles form a favourable environment that facilitates the alloy formation-decomposition process leading to the formation of $Li_{4.4}Sn$ [65, 66], shown by Equation 5. Furthermore, the availability of Li_2O around Sn particles creates enough space to reduce the mechanical stresses experienced by the metal during the alloy formation process, therefore improving the cycle performance of the material [65].

$$SnO_2 + 4Li \Rightarrow Sn + 2Li_2O \quad (4)$$

$$Sn + 4.4Li \Leftrightarrow Li_{4.4}Sn \quad (5)$$

Graphite is a better anode material due to the high number of Li-ion insertion sites that it can offer [64]. But, there are other alternative carbon architectures that promise more active sites for Li-ion storage than this material [51, 64]. These include graphene, carbon nanofibers, and single-walled and multi-walled carbon nanotubes (SWCNTs and MWCNTs). These materials show high electronic conductivity and increased capacity which can be attributed to their unique structuring. Graphene is a two-dimensional layer of sp^2-hybridised carbon that is one atom thick and is well known for its excellent electrical conductivity, large surface area and rapid electron mobility [64]. On the other hand, CNTs are made up of graphene nanosheets that have been rolled into single, double or multi layers. MWCNTs, amongst the different

forms of CNTs offer the highest capacity (575 mA h g^{-1}) which is associated with their long and stable cycle life, and are now the preferred anodes for Li-ion batteries [67].

1.3.3. Cathode Materials

Cathode materials are the third most important component in Li-ion batteries. The majority of these materials are made up of transition metal oxides that have specific sites for hosting Li-ions [68]. These materials are the main source of Li-ions and they initiate the de-intercalation and intercalation processes. Therefore, lithium transportation rates depend entirely on these materials and ultimately determine the efficiency, storage capability, cell voltage and capacities in Li-ion batteries [68, 69]. Cathode materials are the most active materials in Li-ion batteries, but they offer very low capacities compared to the anode materials [69]. Hence, more emphasis is directed towards the improvement of these materials in order to enhance performance deliverables in these batteries. There are different types of cathode material which can be classified into various families such as the layered, spinel, olivine, silicate, tavorite and borate compounds [69]. The silicates, tavorites and borates are relatively new compared to the other class of cathode materials and they've gain tremendous interest due to their promising theoretical properties which are a perfect match for next generation of Li-ion batteries.

For any material to qualify as a cathode for use in Li-ion batteries it must have the following features: (i) the material must not undergo any chemical reactions with the electrolyte to maintain long cycle life and safety. (ii) must have stable structural and chemical properties that can withstand repeated discharge and charge processes in order to produce high cycle life. (iii) the intercalated or de-intercalated Li-ions must have high diffusion coefficients in order to provide high rate capabilities. (iv) it must also have high energy density which needs to tally with its high free energy and finally (v) the precursors used to prepare these materials must be of low cost and easily available in order to help reduce the price for the final products [51].

1.4. Types of Cathode materials

1.4.1. Layered-based Compounds

The most commonly used cathode materials in today's Li-ion batteries is the layered lithium cobalt oxide ($LiCoO_2$) material which was first introduced by Goodenough and co-workers in 1980 and later commercialized in 1990 [44, 52, 65]. This material forms part of layered lithium transition metal oxides which have the formula, $LiMO_2$ (M = Co, Mn and Ni) [70]. This material offers interesting properties such as low self-discharge, good cycling performance, relatively high theoretical specific capacity (274 mA h g^{-1}), high working potential (3.6 – 4.0 V vs Li/Li^+) and high ionic conductivity that can be associated with its layered structures [44, 71].

However, the formation of unstable cobalt dioxide during charging, and low thermal stability and fast capacity fading during deep cycling (de-lithiation above 4.2 V) are the major obstacles hindering the exploitation/exploration of the material's full capacity [44]. There are also irreversible phases that are formed when the battery is charged at large potential differences which may result to self-ignition, therefore questioning the safety of these materials [71]. The material's high cost and threat to human health due to the use of Co metal are some of the reasons behind the search for alternative materials (with low cost, harmless and environmentally friendly properties) that can replace or dope the Co metal in these batteries.

Different types of metals (Al, Ge, Fe, Mg, Mn, Ti and Cr) have been successfully used as dopants for Co metal to reduce some of the issues encountered with the layered $LiCoO_2$ cathode materials [44]. Several research groups have successfully synthesised doped-$LiCoO_2$ cathode nanomaterials such as $Li[Cr_xCo_{1-x}]O_2$, $Li[Cr_xMn_{1-x}]O_2$ and $Li[Li_yCr_xMn_{1-x-y}]O_2$ by Pan *et al.*, [72] $Li_{1-x}(Ni_{1-y-z}Co_yM_z)O_2$ (M = Al, Mg) by Albrecht *et al.*, [73] and $LiNi_{0.8}Co_{0.2}O_2$, $LiNi_{0.8}Co_{0.2}O_{1.95}F_{0.05}$ and $LiNi_{0.75}Co_{0.2}Mg_{0.05}O_2$ by Zhong, Zhao and Cao [74], and their performances are better than the parent material. Another strategy that has been adopted to improve the stability and performance of these cathode materials is the use of various metal oxides such as TiO_2, Al_2O_3 and ZrO_2 which serve as a coating layer on the surface of these materials. Metal oxides are well-known for high mechanical and chemical

stabilities which help reduce structural changes and undesired side reaction of $LiCoO_2$ with the electrolyte [44].

1.4.2. Spinels

The spinel structured cathode materials demonstrate a robust structure which is suitable for hosting Li-ions. They are relatively cheap and environmentally friendly, therefore a perfect fit for use in high-rate Li-ion battery research and applications [69]. These materials have a cubic spinel-structure characterized by the formula $LiMn_2O_4$ in which the Li and Mn atoms are located at the 8a tetrahedral and 16d octahedral sites of the cubic closed-packed oxygen atoms, respectively [75]. Apart from the superior cycling capacity, high rate capability and high discharge plateau, they offer the lowest theoretical specific capacity (142 mA h g^{-1}) and operates at relatively low potentials (3.0 V vs Li/Li^+) [64, 76]. In addition, these materials also suffer from the Jahn-Teller distortion which causes the transformation in their cubic structure into a tetragonal phase. This transformation is associated with an estimated 6.5 % volume increase which causes fast capacity fade during the charge/discharge processes [75].

To solve this problem, many researchers have come up with various methods such as doping and coating of the material. Surface coating is usually performed using metal oxides and provides a protective layer which inhibits the material from reacting with the electrolyte, one of the factors that fasten the dissolution process of Mn to effect structural changes [77]. Another approach that has proven to be effective at reducing the Jahn-Teller distortion is the doping process. This is achieved by substituting Mn with Ni to produce $LiMn_{2-x}Ni_xO_4$, which is more stable than the parent material [69]. The high oxidation states offered by Ni (Ni^{2+} to Ni^{4+}) have contributed towards the increased operating voltage of these batteries from 3.0 to 4.7 V. Even though that might be the case currently electrolyte materials cannot accommodate such high voltages [69].

1.4.3. Polyanion-based Compounds

The exploration of new cathode materials has led to a development of a new class of compounds called polyanions [6, 44, 70, 78]. These materials are characterised by the

presence of a large polyanions of the form $(XO_4)^{y-}$ (X = P, Si, S, As, Mo or W) into the lattice structures of a metal resulting in a formation of intercalation compounds with increased redox potentials and structural stabilities [6, 44, 70]. In addition, these compounds demonstrate impressive thermal and oxidative stabilities which are not altered by high charging voltages. Such stabilities are associated with the presence of $(XO_4)^{y-}$ unit which forms a strong covalent bond between X-O.

1.4.3.1. Phosphates

The $LiFePO_4$ cathode was developed by Goodenough and co-workers, and is now one of the leading cathode materials used in the Li-ion battery market [79]. The development of such iron-based cathodes has always been the desire for scientists because iron is one of the abundant metals on the earth's crust, low cost and more environmentally friendly compared to Co, Ni and Mn [80, 81]. $LiFePO_4$ has a relatively high theoretical capacity of 170 mA h g^{-1} with a discharge potential of about 3.45 V vs Li/Li^+. In addition, it has high thermal and mechanical stabilities which are desirable for large scale Li-ion battery applications [82].

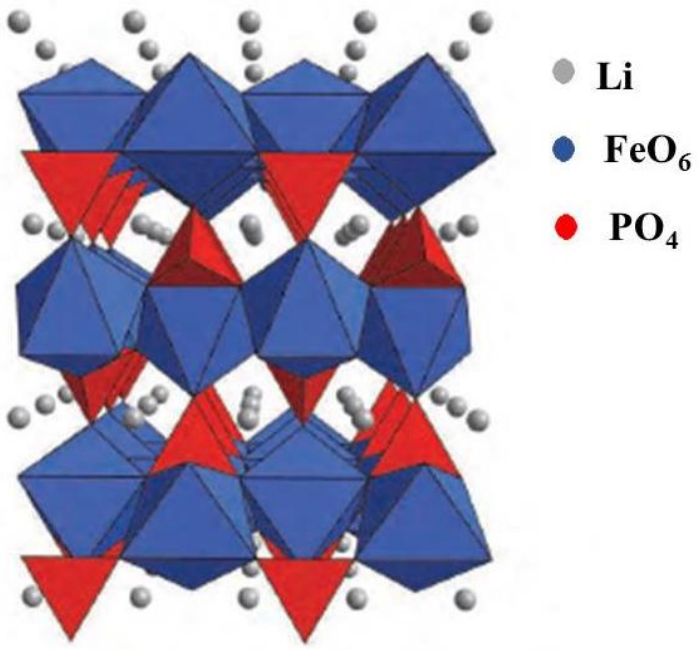

Figure 3: The crystal structure of $LiFePO_4$, showing the sites for Li, FeO_6 octahedra, PO_4 tetrahedral (image taken from [80])

The structural arrangement of atoms in $LiFePO_4$ is significantly different compared to that of other cathodes. This material is defined by an olivine-structure with a *Pmnb* space group which has a distorted hexagonally close-packed backbone where the octahedral and tetrahedral sites of FeO_6 and PO_4, respectively share edges and faces [83, 84] as shown in Fig. 3. The shared faces and edges create a tunnel where the Li-ions can be located, but still remain mobile for insertion and de-intercalation in the framework [84]. Thorough studies on the electrochemical properties of this material have shown that it has an insulating behaviour which is caused by low electronic conductivity (ranging between 10^{-9} and 10^{-11} S cm^{-1}), low chemical diffusion coefficient (10^{-11} to 10^{-13} cm^2 s^{-1}), poor rate capability and low capacity [18, 85].

The above mentioned challenges are also associated with the material's structural arrangements. The observed low ionic conductivity is linked to the one-dimensional movement of Li-ions that are located in between the octahedral and tetrahedral sites. Another issue is the lack of mixed valency that is observed due to low solubility between lithiated $LiFePO_4$ and de-lithiated $FePO_4$ resulting in poor electronic conductivities [85]. These challenges make it difficult to achieve the required number of Li-ions that make it possible to exploit the full capacity of this material. As a result, a number of strategies have been adopted to help improve the electrochemical performance of olivine-structured $LiFePO_4$ cathode materials. These include, but not limited to reducing their particle size or modifications in their structural and morphological properties [85].

Higher electrochemical performance of $LiFePO_4$ can be achieved by coating the nanoparticles with conductive carbon layers which contribute toward the increase in the chemical stability of the material [80]. Gao *et.al.*, [86] prepared nano-sized $LiFePO_4$ coated with 8.6 wt% of gelatin via a gelatin-based sol-gel method. Electrochemical studies of the nanocomposite exhibited good cycle stability with a steady capacity of 151.4 mA h g^{-1} after 100 cycles, at 0.2 C. It has also been observed that carbon coating is essential in these materials because it formulates a stable solid electrolyte interphase which protects the material from reacting with the electrolyte [87].

Zhao *et al.*, [88] prepared magnesium doped $LiFePO_4$ ($Li_{1-2x}Mg_xFePO_4$ (x = 0.00 – 0.05)) nanoparticles via a sol-gel approach. Their findings showed that the doping process did not alter the material's structural framework and there were no impurities observed in the final products. Electrochemical studies showed that the prepared $Li_{0.94}Mg_{0.03}FePO_4$ nanocomposite (x = 0.03) performed better than the other nanocomposites having the highest capacity of 158 mA h g^{-1}. In an attempt to produce higher capacities, other authors performed studies on a combination of both coating and doping. Tian *et al.*, [89] synthesized graphene coated $LiFePO_4$ nanoparticles co-doped with Nb^{5+} and Ti^{4+} via a sol-gel approach. The prepared nanocomposite, $Li_{0.99}Nb_{0.001}Fe_{0.97}Ti_{0.003}PO_4$/graphene maintained a high discharge capacity of 163 mA h g^{-1} for 30 cycles, at 0.1C. The enhanced electrochemical performances were attributed to graphene coating and doping with Nb^{5+} and Ti^{4+}.

1.4.3.2. Silicates

More recently, the silicates (Li_2MSiO_4 (M = Mn, Fe, Co)) have received a lot of attention as a new class of polyanion cathode materials for use in Li-ion batteries [28]. These compounds have the potential for reversible intercalation/de-intercalation of two Li-ions per formula unit [90]. In fact this results in high theoretical capacities of 333 mA h g^{-1} for Li_2MnSiO_4, 325 mA h g^{-1} for Li_2CoSiO_4 and 166 mA h g^{-1} for Li_2FeSiO_4 [91]. Similar to the olivine-structures compounds these materials show an insulating behaviour caused by very low electronic conductivities of 5 x 10^{-16} S cm^{-1} for Li_2MnSiO_4 and 6 x 10^{-14} S cm^{-1} for Li_2FeSiO_4 [18, 92, 93].

One of the most attractive materials in this family is Li_2MnSiO_4 because of the availability of precursors (manganese and silicon) used during its synthesis and the safety of this material during its operation. The material also has the potential to deliver the highest capacity and energy densities compared to other cathodes within and/or outside the silicate family [94, 95]. In line with this, Li_2MnSiO_4 shows a potential to deliver a capacity of 333 mA h g^{-1} through the use of Mn^{2+}/Mn^{3+} and Mn^{3+}/Mn^{4+} electrochemical redox couples to yield an extraction of two Li-ions per formula unit [90, 94]. Theoretically speaking this should also be possible with Li_2FeSiO_4 and Li_2CoSiO_4, however they can only extract one Li-ion per formula unit. This is because the Fe^{3+}/Fe^{4+} and Co^{3+}/Co^{4+} redox couples that are responsible for the

extraction of the second Li-ion are outside the working potential of the commonly used electrolytes [90, 94]. Therefore, an electrolyte with a wide operation window is still required in order to tap into the high capacities of these materials.

The silicates, including Li_2MnSiO_4 exhibit a variety of structural polymorphs grouped as orthorhombic (*Pmn2*$_1$ and *Pmnb*) or monoclinic (*P2*$_1$ and *Pn*) as shown in Fig. 4. The cations (Li, Mn and Si) in these polymorphs are arranged in a tetrahedral co-ordination in a distorted hexagonally closed-packed oxygen assemble [90, 96]. The most popular form is the orthorhombic structure and is characterized by two-dimensional pathways for Li-ion diffusion. On the other hand, the monoclinic form has a structural framework where the Li-ion positions are interconnected in three dimensions [90, 96]. This is a clear indication that the various pathways for diffusion of Li-ions through the crystal lattice and the different linkages in Mn and Si tetrahedral will result in potentially different electrochemical performances of these structural forms [90].

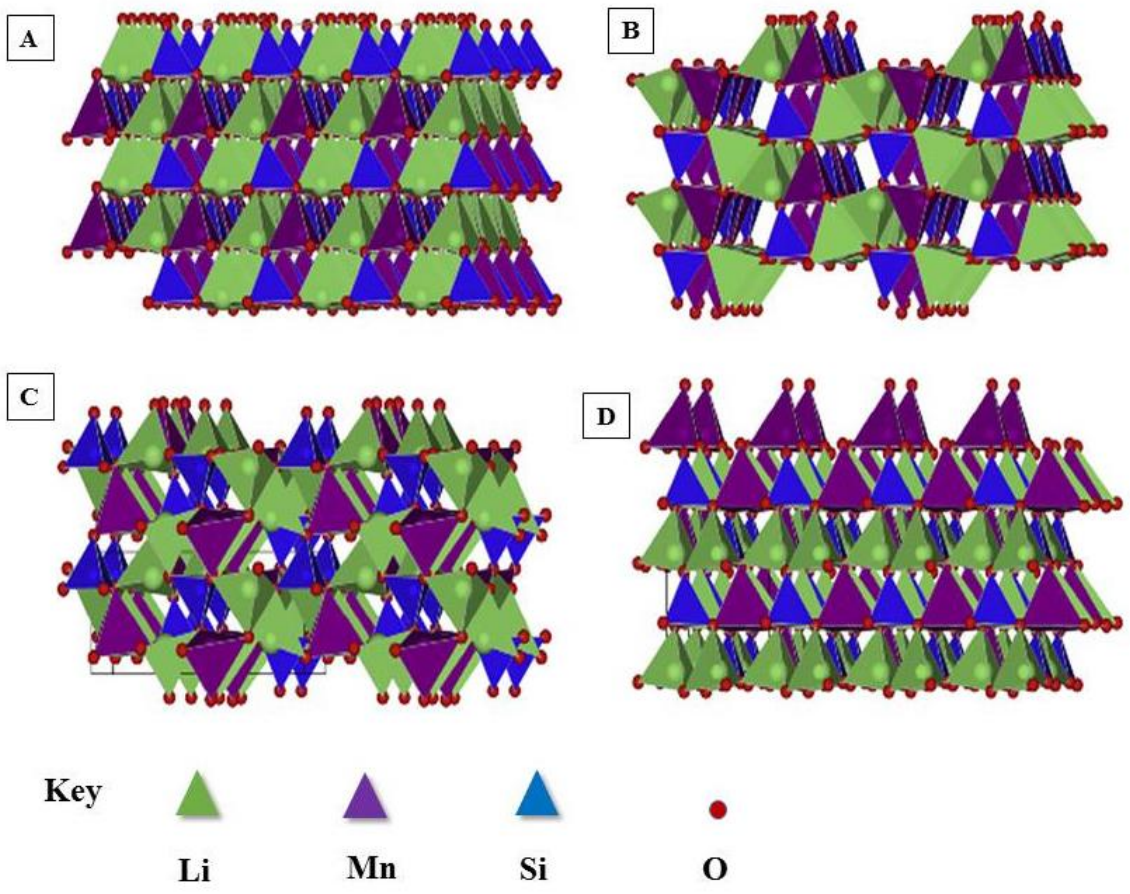

Figure 4: The crystal structures of Li_2MnSiO_4 cathode material (a) *Pmn2₁*, (b) *Pmnb*, (c) *P2₁* and (d) *Pn*, where the green, purple and blue tetrahedral shapes represent Li, Mn and Si, respectively. Finally, the red sphere represents the oxygen atoms (images taken from [94])

Several authors have reported on the synthesis of orthorhombic forms of Li_2MnSiO_4 having a few impurity phases of MnO and Li_2SiO_3 which seem not so easy to avoid [97, 98]. Another challenge is that the *Pmn2₁* and *Pmnb* polymorphs have the same thermodynamic stabilities which make it difficult to prepare pure individual polymorphs of these materials [99]. The preparation of Li_2MnSiO_4 with monoclinic form was first prepared by Politaev *et al.*, [99] by firing its precursor powder for two hours at 1150 ºC. The instabilities observed with the monoclinic structural form resulted in a transformation into the orthorhombic *Pmn2₁* polymorph which is proof that indeed it is difficult to isolate pure-phase Li_2MnSiO_4 [100]. A possible solution that has proved to be effective in improving the stability and maintenance of a single-phase of these materials is the substitution of Mn with Mg or Li with Na [94].

Another setback with Li_2MnSiO_4 is that the extraction of more than one Li-ion per formula unit causes drastic volume changes which lead to amorphization and structural collapse [18]. Eventually a capacity fade is observed for the subsequent electrochemical charge/discharge processes [18, 95, 101]. This has opened a lot of research opportunities within the Li-ion battery research and strategies such as particle size reduction, doping and carbon coating have proven to be effective to counteract some of the challenges encountered with Li_2MnSiO_4 and other cathode materials in general.

1.5. Avenues to Enhance Electrochemical Performance of Cathodes

Li-ion batteries have become a battery of choice in many portable electronic devices and automotive applications, and are slowly immerging as a possible solution for energy storage purposes. These batteries offer impressive properties compared to other existing rechargeable batteries. The cathode material is an important component in these batteries and its optimum performance is affected by a number of issues such as structural changes (volume expansion, sometimes leading to structural collapse) during the intercalation and de-intercalation processes [75], low electronic conductivity [85, 93] and slow Li-ion diffusion within their structural framework [18]. These issues affect the performance of these batteries by reducing their capacity, especially when they are operated at high currents [102]. Avenues such as coating, doping, particle size reduction and blending have proven to be effective techniques for improving the performance of these materials.

1.5.1. Reduction of Particle Size

The influence of particle size reduction on the performance of cathode materials can be explained using the diffusion formula [103]:

$$t = \frac{L^2}{2D} \tag{6}$$

where t is the diffusion time, L is the diffusion distance and D is the diffusion coefficient. Reduced particle size will result in a shorter diffusion time leading to accelerated kinetics for Li-ion transport [84]. At the same time this will also result in a decreased structural strain that is usually experienced by these materials during the intercalation/de-intercalation of Li-ions and an increased cycle life. In addition, nanosized particles have large surface-to-volume ratios which can help increase the rate capability of the material [66, 69]. There are several methods that are used to produce nanostructured cathode materials such as sol-gel, hydrothermal, solvothermal, co-precipitation, spray pyrolysis, combustion, mechanochemical, solid-state and emulsion-drying processes [104]. These methods can be modified by incorporating conductive carbon materials (such as carbon nanotubes, graphene and polymers) into the precursors of these materials which will help further reduce the size of the nanoparticles.

Particles size reduction is an effective way of improving the diffusion kinetics of Li-ions in and out of the cathode materials, but it comes with its own challenges such as the increased number of side reactions between the electrode surface and the electrolyte material, resulting in lower thermodynamic stabilities, high self-discharge and poor cycle life [66]. Nanostructured cathode materials can be obtained using complex synthesis methods and fine tuning a number of parameters which could increase the manufacturing costs [66].

1.5.2. Carbon Coating

Surface coating provides a conductive layer which extends the performance of cathode materials by preventing them from side reactions with the electrolyte, suppress structural changes and preserve the cations in their crystal sites thereby improving the structure and cycle stability in these cathode materials [105]. Carbon coating is the most economic and effective way compared to other coating techniques and materials [105]. This is no surprise because carbon materials have good electronic conductivities and are essential for enhancing electron and ion transfer kinetics. These improvements are needed to increase the charge mobility on the surface of these cathode materials [105, 106]. In addition, these materials are mostly focused on improving the conductivities of low conductive materials (semiconductors or insulators) such as phosphates and silicates in the case of Li-ion battery applications.

Graphene serves as a building block of most carbon forms. This material is a two-dimensional one-atom-thick sheet made up of sp^2 carbon atoms [107, 108]. In addition, the graphene nanosheets can be rolled to form single or multi-walled carbon nanotubes, can also be wrapped to form spherically shaped bulky balls or stacked into layers (more than ten layers) which form three-dimensional graphite structure [107]. The popularly used technique for the preparation of graphene is the exfoliation and reduction of graphite oxide. The synthesis is initiated by oxidising graphite to form graphite oxide, usually via the modified Hummer's method [109]. Then the produced graphite oxide sheets are chemically or thermally reduced in order to remove oxygen-containing functional groups and further exfoliate the sheets to form graphene [33]. The chemical reduction method is usually preferred over thermal reduction because of the ease to control the degree of reduction and dispersibility by making use of different reducing agents or the same reducing agent but different concentrations [33].

Graphene is characterized by its high electronic and thermal conductivities, large surface area (2630 m^2 g^{-1}), chemical stability and sp^2 carbon atoms that are organised in a hexagonal two-dimensional structure [33, 110]. These properties make the material to be a suitable additive in Li-ion batteries to enhance the conductivity of cathode materials. The material's large surface area, large number of active sites on its surface as well as the fast electron kinetics contributes greatly on the electrochemistry of graphenised cathode materials resulting into high energy and power dense Li-ion batteries [33].

The main drawback with carbon coating is that it decomposes at high temperatures and this compromise the performance of the coated cathode material. The decomposition process generates strong reducing agents such as H_2 and CO_2. These facilitate the reduction of metal oxides to form undesired valence state of the metal and alters the crystal structure of the cathode material [105].

1.5.3. Doping with Inorganics

Doping was first introduced by Woodyard in his work with semiconductors and was later adopted into Li-ion batteries to improve the performance of cathode materials [111, 112]. There are two types of doping techniques, substitutional and interstitial doping illustrated by Equations 7 and 8, respectively:

$$LM_2O_4 \rightarrow LM_{1.7}N_{0.3}O_4 \quad (7)$$

$$LM_2O_4 \rightarrow L_{1.1}M_2O_4 \quad (8)$$

where LM_2O_4 represents a typical spinel cathode material used to demonstrate the doping process ($LiMn_2O_4$). Both techniques are used to improve the performance of cathode materials, however, as it can be seen from Equations 7 and 8 these may result in different structural changes or modifications. Interstitial doping may change the structural framework of the cathode material because the ions in the doped nanocomposite sit in the interstitial sites making it difficult to locate their precise positions. However, substitutional-doped nanocomposites maintain the structure of the pristine material because the added ions occupy the space of the substituted ions and can be precisely located within the structural framework of the material [112].

1.5.4. Blending of Cathode Materials

Another strategy to improve the performance of Li-ion batteries is through the mixing of two or more lithium insertion compounds that complement each other's properties with an expectation that they will compensate their disadvantages [113]. These compounds are called blended or hybrid cathode materials and their performances are better than the individual cathode materials [113]. These materials were developed because a single cathode material does not meet the requirements of a superior cathode material which includes, but not limited

to high theoretical capacity, good rate performance, long cycle stability, high operating voltage and good electrochemical and thermal stabilities [39].

Hybrid cathode materials have been successfully prepared by synthesising one cathode material and then modifying it with another cathode material via processes such as the sol-gel, solid-state or mechanical milling methods. Sadeghi and co-workers [114] prepared $LiMn_2O_4$-$LiFePO_4$ hybrid cathode material by taking already-prepared $LiMn_2O_4$ nanoparticles and coated them with $LiFePO_4$ via the sol-gel method. The hybrid cathode material showed better cyclic stability than the unmodified $LiMn_2O_4$. Qui *et al*., [115] used manufactured pristine $LiMn_2O_4$ and $LiFePO_4$ cathode materials and mixed them together using both hand and ball milling methods to produce $LiMn_2O_4$-$LiFePO_4$ hybrid cathode materials. They used different mass ratios of the pristine materials and tested the electrochemistry of the hybrid materials. Their results showed that the hybrid cathode with a 1:1 mass ratio gave better performances than the other mass ratios. In addition, the hand milling technique gave uniform $LiMn_2O_4$-$LiFePO_4$ hybrid cathode materials whereas the ball milling approach produced agglomerated nanoparticles with decreased electrochemical performance.

Sadeghi *et al.* [114] and Yun *et al*. [116] have also prepared these hybrid cathodes in a slightly different manner where they used one cathode as the parent (main material) and the other as the coating or modifying material. Therefore, the parent is in higher ratio than the coating material. In some cases there is no parent cathode material, the pristine cathode materials are mixed in equal mass or equimolar ratios to form a hybrid cathode material with better performances than the two individual cathode materials [117-119]. As previously stated, most cathode materials have low electronic conductivities and blending them together does not really improve their conductivity. Therefore, these materials are further coated by another material which will improve their conductivities and overall battery performance.

1.6. Rationale of Study

A typical Li-ion battery is made up of a negative electrode (anode) and a positive electrode (cathode) immersed in a Li-ion conducting material that is impermeable to electrons (electrolyte material). The performance of any Li-ion battery is largely influenced by its cathode material which is an essential component in these batteries [120]. Lithium iron phosphate ($LiFePO_4$) cathode material is characterized by its high theoretical capacity (170 mA h g^{-1}), excellent thermal and structural stabilities, cycle stability and flat operating voltage (~3.5 V vs Li/Li^+) through the Fe^{2+}/Fe^{3+} redox couple [86, 121-123]. Similarly, lithium manganese orthosilicate (Li_2MnSiO_4) cathode material has attracted a lot of researchers due to its environmentally friendliness, safety, cost effectiveness, high cell voltage (4.2 V vs Li/Li^+) and high theoretical capacity (333 mA h g^{-1}) associated with the possibility to extract more than one electron per formula unit [96, 97, 101, 124, 125]. A mixture (or a blend) of the two cathode materials would result in a hybrid cathode material with much better properties than the individual materials

The concept of blending cathode materials is a new strategy that is used to address some of the challenges that prevent the optimum performance of individual cathode materials [39, 126]. The mixture of two or more cathode materials that complement each other's properties will yield hybrid cathode materials with enhanced performances [127]. In line with this, a $LiFePO_4$-Li_2MnSiO_4 hybrid cathode material can be obtained by blending pristine $LiFePO_4$ and Li_2MnSiO_4. The pristine cathode materials are polyanion compounds and are characterised by the presence of the $(XO_4)^n$ unit which is associated with their high stability and better performance compared to other transition metal oxides [81, 94, 128-130]. In addition, these stabilities are attributed to the presence of strong covalent bonds between P-O and Si-O in $LiFePO_4$ and Li_2MnSiO_4, respectively [131-134].

Furthermore, the olivine $LiFePO_4$ offers its high theoretical capacity, stable charge/discharge curves, high voltage (3.4 V vs Li/Li^+) and long cycle stability [131, 132]. Meanwhile, Li_2MnSiO_4 contributes its high voltage (4.2 V vs Li/Li^+) and high theoretical capacity of 333 mA h g^{-1} (almost double that of the $LiFePO_4$) which is achieved by assuming reversible extraction of two moles of Li-ion per formula unit through the use of $Mn^{2+/}Mn^{3+}$ and Mn^{3+}/Mn^{4+} redox couples [96, 99, 135]. The hybrid cathode material is further coated using

graphene because of its large surface area, chemical stability, superior electric and thermal stability which contribute towards improving its performance [33]. The raw materials (iron, manganese, silicon and phosphorous) are non-toxic and relatively cheap because they are produced here in South Africa [136, 137]. Additionally, the use of low cost, sustainable and easily available precursors is promoted for the research and development of Li-ion batteries in order to reduce the cost of these batteries [90, 138].

1.7. Problem Statement

There are shortcomings that prevent these cathode materials from reaching their optimum performances. For instance, the full potential of $LiFePO_4$ is affected by its low Li-ion diffusivity that takes place during charge/discharge processes and poor electronic conductivity (10^{-9} to 10^{-10} S cm^{-1}) which result in low specific capacity and poor performance [86, 121]. Similarly, the performance of Li_2MnSiO_4 is affected by its low electronic conductivity (~10^{-16} S cm^{-1}), low Li-ion diffusion, rapid capacity fade and poor cycling stability that is caused by the Jahn-Teller distortion experienced by Mn^{3+} [124].

1.8. Research Aim and Objectives

The aim of this study is therefore to enhance the electrochemical and physical properties of li-ion batteries in order to provide sufficient energy and power density in modern batteries by synthesizing graphenised lithium iron phosphate-lithium manganese orthosilicate hybrid cathode materials. The outlined aim will be achieved by following these research objectives:

- Preparation of graphene oxide followed by chemical reduction in order to obtain reduced graphene oxide nanosheets.
- Functional group, morphology and structural characterization of the nanosheets to be performed with Fourier transform infrared spectroscopy (FTIR), Raman Spectroscopy, High Resolution Transmission and Scanning Electron Microscopy (HRTEM and HRSEM), X-ray diffraction (XRD) and Solid State Nuclear Magnetic Resonance Spectroscopy (SS NMR).

- Synthesis of both pristine lithium iron phosphate and lithium manganese orthosilicate and perform functional group, morphology and structural analysis using the above mentioned techniques.
- Synthesis of $LiFePO_4$-Li_2MnSiO_4 and graphenised $LiFePO_4$-Li_2MnSiO_4 hybrid cathode materials via hand milling and *in situ* sol-gel methods.
- Perform functional group, morphology and structural analysis using the above mentioned techniques.
- Electrochemical characterization of the as-prepared graphene nanosheets, pristine cathode nanomaterials and the hybrid cathode materials using Cyclic Voltammetry, Square Wave Voltammetry and Electrochemical Impedance Spectroscopy (EIS).

REFERENCES

1. Dillon, A., *Carbon nanotubes for photoconversion and electrical energy storage.* Chemical reviews, 2010. **110**(11): p. 6856-6872.
2. Rodhe, H., *A comparison of the contribution of various gases to the greenhouse effect.* Science, 1990. **248**(4960): p. 1217-1219.
3. Dessus, B., B. LaPonche, and H. Le Treut, *Global warming: The significance of methane.* Unpublished Manuscript, 2008: p. 1-7.
4. Fuller, T. *Renewable Fuels 2: Biomass*. 2016; Available from: https://thelukewarmersway.wordpress.com/2016/01/04/renewable-fuels-2-biomass/.
5. Menyah, K. and Y. Wolde-Rufael, *Energy consumption, pollutant emissions and economic growth in South Africa.* Energy Economics, 2010. **32**(6): p. 1374-1382.
6. Song, M.-K., S. Park, F.M. Alamgir, J. Cho, and M. Liu, *Nanostructured electrodes for lithium-ion and lithium-air batteries: the latest developments, challenges, and perspectives.* Materials Science and Engineering: R: Reports, 2011. **72**(11): p. 203-252.
7. Banks, D. and J. Schaffler, *The potential contribution of renewable energy in South Africa*. 2006, RAPS Consulting (Pty) Ltd and Nano Energy (Pty) Ltd: Johannesburg, South Africa. p. 93.

8. Alexander, C. and J.O. Reno, *From biopower to energopolitics in England's modern waste technology.* Anthropological Quarterly, 2014. **87**(2): p. 335-358.
9. Colvile, R.N., E.J. Hutchinson, J.S. Mindell, and R.F. Warren, *The transport sector as a source of air pollution.* Atmospheric Environment, 2001. **35**(9): p. 1537-1565.
10. Wakefield, E.H., *History of the Electric Automobile*. 1993, United States of America: Society of Automotive Engineers: Hybrid Electric Vehicles. 332.
11. Matulka, R. *The history of the electric car*. 2014; Available from: https://energy.gov/articles/history-electric-car.
12. Mammadov, R., *The importance of transportation in tourism sector.* 7th Silk Road International Conference "Challenges and opportunities of sustaible economic development in Eurasian countries", 2012: p. 381-386.
13. Hannan, M.A., M.M. Hoque, A. Mohamed, and A. Ayob, *Review of energy storage systems for electric vehicle applications: Issues and challenges.* Renewable and Sustainable Energy Reviews, 2017. **69**: p. 771-789.
14. Pimentel, D., X. Huang, A. Codova, and M. Pimentel, *Impact of a growing population on natural resources: The challenge for environmental management.* Frontiers: The Interdisciplinary Journal of Study Abroad, 1997. **3**(2): p. 105-31.
15. Carl Haub, K.P. and B. Curney, *2007 World Population Data Sheet*. 2007, Population Refenerence Bureau: 1875 Connecticut Avenue, NW, Washington, DC 20009, United States of America. p. 15.
16. Kaneda, T. and G. Dupuis, *2017 World Population Data Sheet with a special focus on youth*. 2017, Population Reference Bureau: 1875 Connecticut Ave., NW, Suite 520, Washington, DC 20009, United States of America. p. 21.
17. Wang, T., Y. Gong, and C. Jiang, *A review on promoting share of renewable energy by green-trading mechanisms in power system.* Renewable and Sustainable Energy Reviews, 2014. **40**: p. 923-929.
18. Chen, J., *Recent progress in advanced materials for lithium ion batteries.* Materials, 2013. **6**(1): p. 156-183.
19. Apergis, E. and N. Apergis, *The role of rare earth prices in renewable energy consumption: The actual driver for a renewable energy world.* Energy Economics, 2017. **62**: p. 33-42.
20. *Renewable Energy*. Available from: http://www.energy.gov.za/files/renewables_frame.html.

21. *Electricity technologies*. 2017; Available from: http://www.eskom.co.za/AboutElectricity/ElectricityTechnologies/Pages/Electricity_Technologies.aspx.
22. Kousksou, T., P. Bruel, A. Jamil, T. El Rhafiki, and Y. Zeraouli, *Energy storage: Applications and challenges.* Solar Energy Materials and Solar Cells, 2014. **120**: p. 59-80.
23. Vaclav, S., *Energy in Nature and Society: General energetics of complex systems*. 2008, United States of America: MIT press. 480.
24. Lorot, P. and J.-F. Lethu, *2015 Choiceul Energy Index*. 2015, Institut Choiseul Paris, France. p. 26.
25. Winkler, H., *Energy policies for sustainable development in South Africa.* Energy for Sustainable Development, 2007. **11**(1): p. 26-34.
26. Yang, Z., J. Zhang, M.C. Kintner-Meyer, X. Lu, D. Choi, J.P. Lemmon, and J. Liu, *Electrochemical energy storage for green grid.* Chemical reviews, 2011. **111**(5): p. 3577-3613.
27. Kingsbury, R.S., K. Chu, and O. Coronell, *Energy storage by reversible electrodialysis: The concentration battery.* Journal of Membrane Science, 2015. **495**: p. 502-516.
28. Li, Y., Y. Lu, C. Zhao, Y.-S. Hu, M.-M. Titirici, H. Li, X. Huang, and L. Chen, *Recent advances of electrode materials for low-cost sodium-ion batteries towards practical application for grid energy storage.* Energy Storage Materials, 2017.
29. Goodenough, J.B., H.D. Abruna, and M.V. Buchanan, *Basic Research Needs for Electrical Energy Storage*. 2007, Report of the Basic Energy Sciences Workshop on Electrical Energy Storage, April 2-4, 2007: United States. p. 186.
30. Mahlia, T.M.I., T.J. Saktisahdan, A. Jannifar, M.H. Hasan, and H.S.C. Matseelar, *A review of available methods and development on energy storage; technology update.* Renewable and Sustainable Energy Reviews, 2014. **33**: p. 532-545.
31. Aguado, J., S. de la Torre, and A. Triviño, *Battery energy storage systems in transmission network expansion planning.* Electric Power Systems Research, 2017. **145**: p. 63-72.
32. Divya, K. and J. Østergaard, *Battery energy storage technology for power systems - An Overview.* Electric Power Systems Research, 2009. **79**(4): p. 511-520.

33. Lv, W., Z. Li, Y. Deng, Q.-H. Yang, and F. Kang, *Graphene-based materials for electrochemical energy storage devices: opportunities and challenges.* Energy Storage Materials, 2016. **2**: p. 107-138.
34. Rui, X., Q. Yan, M. Skyllas-Kazacos, and T.M. Lim, *$Li_3V_2(PO_4)_3$ cathode materials for lithium-ion batteries: a review.* Journal of Power Sources, 2014. **258**: p. 19-38.
35. Chen, K. and D. Xue, *Materials chemistry toward electrochemical energy storage.* Journal of Materials Chemistry A, 2016. **4**(20): p. 7522-7537.
36. Koohi-Kamali, S., V.V. Tyagi, N.A. Rahim, N.L. Panwar, and H. Mokhlis, *Emergence of energy storage technologies as the solution for reliable operation of smart power systems: A review.* Renewable and Sustainable Energy Reviews, 2013. **25**(0): p. 135-165.
37. Winter, M. and R.J. Brodd, *What Are Batteries, Fuel Cells, and Supercapacitors?* Chemical Reviews, 2004. **104**(10): p. 4245-4270.
38. Zhao, H., Q. Wu, S. Hu, H. Xu, and C.N. Rasmussen, *Review of energy storage system for wind power integration support.* Applied Energy, 2015. **137**: p. 545-553.
39. Wei, C., W. He, X. Zhang, J. Shen, and J. Ma, *Recent progress in hybrid cathode materials for lithium ion batteries.* New Journal of Chemistry, 2016. **40**(4): p. 2984-2999.
40. Evarts, E.C., *Lithium batteries: To the limits of lithium.* Nature, 2015. **526**(7575): p. S93-S95.
41. Zuo, D., G. Tian, X. Li, D. Chen, and K. Shu, *Recent progress in surface coating of cathode materials for lithium ion secondary batteries.* Journal of Alloys and Compounds, 2017. **706**: p. 24-40.
42. Palomares, V. and T. Rojo, *Synthesis processes for Li-ion battery electrodes–from solid state reaction to solvothermal self-assembly methods*, in *Lithium ion batteries - New developments*. 2012, InTech: Slavka Krautzeka 83/A, 51000 Rijeka, Croatia. p. 22.
43. Treptow, R.S., *Lithium batteries: A practical application of chemical principles.* Journal of Chemical Education, 2003. **80**(9): p. 1015-1020.
44. Nitta, N., F. Wu, J.T. Lee, and G. Yushin, *Li-ion battery materials: Present and Future.* Materials today, 2015. **18**(5): p. 252-264.
45. Whittingham, M.S., *Lithium batteries and cathode materials.* Chemical reviews, 2004. **104**(10): p. 4271-4302.

46. Sehrawat, P., C. Julien, and S. Islam, *Carbon nanotubes in Li-ion batteries: A Review.* Materials Science and Engineering: B, 2016. **213**: p. 12-40.
47. Mohri, M., N. Yanagisawa, Y. Tajima, H. Tanaka, T. Mitate, S. Nakajima, M. Yoshida, Y. Yoshimoto, T. Suzuki, and H. Wada, *Rechargeable lithium battery based on pyrolytic carbon as a negative electrode.* Journal of Power Sources, 1989. **26**(3-4): p. 545-551.
48. T, J.R., K. Xu, O. Borodin, and M. Ue, eds. *Electrolytes for Lithium and Lithium-Ion Batteries*. 2014, Springer: Springer New York Heidelberg Dordrecht London. 488.
49. Oberhofer, A. and P. Meisen, *Energy Storage Technologies & Their Role in Renewable Integration*. 2012, Suite 308, San Diego, California 92120, United States of America: Global Energy Network Institute (GENI). 38.
50. Dell, R.M. and D.A.J. Rand, *Understanding Batteries*. 2001, Thomas Graham House, Science Park, Milton Road, Cambridge CB4 0WF, United Kingdom: Royal Society of Chemistry. 223.
51. Bazzi, K., *Nanostrucured Lithium Iron Phosphate As Cathode Material For Lithium Ion-Batteries*. 2014, Wayne State University: Detroit, Michigan, United States. p. 160.
52. Mizushima, K., P. Jones, P. Wiseman, and J.B. Goodenough, *Li_xCoO_2 (0< x<-1): A new cathode material for batteries of high energy density.* Materials Research Bulletin, 1980. **15**(6): p. 783-789.
53. Tarascon, J.-M. and M. Armand, *Issues and challenges facing rechargeable lithium batteries.* Nature, 2001. **414**(6861): p. 359-367.
54. Li, Q., J. Chen, L. Fan, X. Kong, and Y. Lu, *Progress in electrolytes for rechargeable Li-based batteries and beyond.* Green Energy & Environment, 2016. **1**(1): p. 18-42.
55. Marcinek, M., J. Syzdek, M. Marczewski, M. Piszcz, L. Niedzicki, M. Kalita, A. Plewa-Marczewska, A. Bitner, P. Wieczorek, T. Trzeciak, M. Kasprzyk, P.Łężak, Z. Zukowska, A. Zalewska, and W. Wieczorek, *Electrolytes for Li-ion transport – Review.* Solid State Ionics, 2015. **276**(Supplement C): p. 107-126.
56. Goodenough, J.B. and Y. Kim, *Challenges for rechargeable Li batteries†.* Chemistry of Materials, 2009. **22**(3): p. 587-603.
57. Alias, N. and A.A. Mohamad, *Advances of aqueous rechargeable lithium-ion battery: A review.* Journal of Power Sources, 2015. **274**: p. 237-251.
58. Li, W., W.R. McKinnon, and J.R. Dahn, *Lithium intercalation from aqueous solutions.* Journal of The Electrochemical Society, 1994. **141**(9): p. 2310-2316.

59. Wessells, C., R. Ruffo, R.A. Huggins, and Y. Cui, *Investigations of the electrochemical stability of aqueous electrolytes for lithium battery applications.* Electrochemical and Solid-State Letters, 2010. **13**(5): p. A59-A61.

60. Chang, Z., C. Li, Y. Wang, B. Chen, L. Fu, Y. Zhu, L. Zhang, Y. Wu, and W. Huang, *A lithium ion battery using an aqueous electrolyte solution.* Scientific Reports, 2016. **6**: p. 1-6.

61. Kim, H., J. Hong, K.-Y. Park, H. Kim, S.-W. Kim, and K. Kang, *Aqueous rechargeable Li and Na ion batteries.* Chemical reviews, 2014. **114**(23): p. 11788-11827.

62. T, R.J., K. Xu, O. Borodin, and M. Ue, *Electrolytes for lithium and lithium-ion batteries*. Modern Aspects of electrochemistry, ed. W. Ralph E. Vol. 58. 2014, New York, Heidelberg Dordrecht, London: Springer. 476.

63. Marom, R., O. Haik, D. Aurbach, and I.C. Halalay, *Revisiting $LiClO_4$ as an electrolyte for rechargeable lithium-ion batteries.* Journal of the Electrochemical Society, 2010. **157**(8): p. A972-A983.

64. Armstrong, M.J., C. O'Dwyer, W.J. Macklin, and J.D. Holmes, *Evaluating the performance of nanostructured materials as lithium-ion battery electrodes.* Nano Research, 2014. **7**(1): p. 1-62.

65. Scrosati, B., *Recent advances in lithium ion battery materials.* Electrochimica Acta, 2000. **45**(15): p. 2461-2466.

66. Manthiram, A., A.V. Murugan, A. Sarkar, and T. Muraliganth, *Nanostructured electrode materials for electrochemical energy storage and conversion.* Energy & Environmental Science, 2008. **1**(6): p. 621-638.

67. Chew, S.Y., S.H. Ng, J. Wang, P. Novák, F. Krumeich, S.L. Chou, J. Chen, and H.K. Liu, *Flexible free-standing carbon nanotube films for model lithium-ion batteries.* Carbon, 2009. **47**(13): p. 2976-2983.

68. Xu, B., D. Qian, Z. Wang, and Y.S. Meng, *Recent progress in cathode materials research for advanced lithium ion batteries.* Materials Science and Engineering: R: Reports, 2012. **73**(5): p. 51-65.

69. Chen, R., T. Zhao, X. Zhang, L. Li, and F. Wu, *Advanced cathode materials for lithium-ion batteries using nanoarchitectonics.* Nanoscale Horizons, 2016. **1**(6): p. 423-444.

70. Ellis, B.L., K.T. Lee, and L.F. Nazar, *Positive electrode materials for Li-ion and Li-batteries.* Chemistry of Materials, 2010. **22**(3): p. 691-714.

71. Yaroslavtsev, A.B., T. Kulova, and A.M. Skundin, *Electrode nanomaterials for lithium-ion batteries.* Russian Chemical Reviews, 2015. **84**(8): p. 826.

72. Pan, C., Y.J. Lee, B. Ammundsen, and C.P. Grey, *^{6}Li MAS NMR studies of the local structure and electrochemical properties of Cr-doped lithium manganese and lithium cobalt oxide cathode materials for lithium-ion batteries.* Chemistry of materials, 2002. **14**(5): p. 2289-2299.

73. Albrecht, S., J. Kümpers, M. Kruft, S. Malcus, C. Vogler, M. Wahl, and M. Wohlfahrt-Mehrens, *Electrochemical and thermal behavior of aluminum-and magnesium-doped spherical lithium nickel cobalt mixed oxides $Li_{1-x}(Ni_{1-y-z}Co_yM_z)O_2$ (M = Al, Mg).* Journal of power sources, 2003. **119**: p. 178-183.

74. Zhong, Y., X. Zhao, and G. Cao, *Characterization of solid-state synthesized pure and doped lithium nickel cobalt oxides.* Materials Science and Engineering: B, 2005. **121**(3): p. 248-254.

75. Xia, H., Z. Luo, and J. Xie, *Nanostructured $LiMn_2O_4$ and their composites as high-performance cathodes for lithium-ion batteries.* Progress in Natural Science: Materials International, 2012. **22**(6): p. 572-584.

76. Xia, H., Z. Luo, and J. Xie, *Nanostructured LiMn 2 O 4 and their composites as high-performance cathodes for lithium-ion batteries.* Progress in Natural Science: Materials International, 2012. **22**(6): p. 572-584.

77. Lee, M.-J., S. Lee, P. Oh, Y. Kim, and J. Cho, *High performance $LiMn_2O_4$ cathode materials grown with epitaxial layered nanostructure for Li-ion batteries.* Nano letters, 2014. **14**(2): p. 993-999.

78. Nanjundaswamy, K., A. Padhi, J. Goodenough, S. Okada, H. Ohtsuka, H. Arai, and J. Yamaki, *Synthesis, redox potential evaluation and electrochemical characteristics of NASICON-related-3D framework compounds.* Solid State Ionics, 1996. **92**(1-2): p. 1-10.

79. Padhi, A.K., K.S. Nanjundaswamy, and J.B. Goodenough, *Phospho-olivines as positive-electrode materials for rechargeable lithium batteries.* Journal of the electrochemical society, 1997. **144**(4): p. 1188-1194.

80. Molenda, J. and M. Molenda, *Composite Cathode Material for Li-Ion Batteries Based on LiFePO4 System*, in *Metal, Ceramic and Polymeric Composites for Various Uses*. 2011, InTech: Slavka Krautzeka 83/A, 51000 Rijeka, Croatia. p. 16.

81. Wu, B., Y. Ren, and N. Li, *$LiFePO_4$ Cathode Material*, in *Electric Vehicles - The Benefits and Barriers*, S. Soylu, Editor. 2011, InTech: Slavka Krautzeka 83/A, 51000 Rijeka, Croatia. p. 16.

82. Nytén, A., *Low-Cost Iron-Based Cathode Materials for Large-Scale Battery Applications*. 2006, Uppsala University: Uppsala, Sweden. p. 54.

83. Jugović, D. and D. Uskoković, *A review of recent developments in the synthesis procedures of lithium iron phosphate powders.* Journal of Power Sources, 2009. **190**(2): p. 538-544.

84. Zhang, Y., Q.-y. Huo, P.-p. Du, L.-z. Wang, A.-q. Zhang, Y.-h. Song, Y. Lv, and G.-y. Li, *Advances in new cathode material $LiFePO_4$ for lithium-ion batteries.* Synthetic Metals, 2012. **162**(13): p. 1315-1326.

85. Bi, Z., X. Zhang, W. He, D. Min, and W. Zhang, *Recent advances in $LiFePO_4$ nanoparticles with different morphology for high-performance lithium-ion batteries.* RSC Advances, 2013. **3**(43): p. 19744-19751.

86. Gao, M., N. Liu, Z. Li, W. Wang, C. Li, H. Zhang, Y. Chen, Z. Yu, and Y. Huang, *A gelatin-based sol–gel procedure to synthesize the $LiFePO_4$/C nanocomposite for lithium ion batteries.* Solid State Ionics, 2014. **258**: p. 8-12.

87. Eftekhari, A., *$LiFePO_4$/C nanocomposites for lithium-ion batteries.* Journal of Power Sources, 2017. **343**: p. 395-411.

88. Zhao, X., D.-H. Baek, J. Manuel, M.-Y. Heo, R. Yang, J.K. Ha, H.-S. Ryu, H.-J. Ahn, K.-W. Kim, and K.-K. Cho, *Electrochemical properties of magnesium doped $LiFePO_4$ cathode material prepared by sol–gel method.* Materials Research Bulletin, 2012. **47**(10): p. 2819-2822.

89. Tian, Z., Z. Zhou, S. Liu, F. Ye, and S. Yao, *Enhanced properties of olivine $LiFePO_4$/graphene co-doped with Nb^{5+} and Ti^{4+} by a sol–gel method.* Solid State Ionics, 2015. **278**: p. 186-191.

90. Islam, M.S., R. Dominko, C. Masquelier, C. Sirisopanaporn, A.R. Armstrong, and P.G. Bruce, *Silicate cathodes for lithium batteries: alternatives to phosphates?* Journal of Materials Chemistry, 2011. **21**(27): p. 9811-9818.

91. Ferrari, S., M.C. Mozzati, M. Lantieri, G. Spina, D. Capsoni, and M. Bini, *New materials for Li-ion batteries: synthesis and spectroscopic characterization of Li_2(Fe MnCo)SiO_4 cathode materials.* Scientific Reports, 2016. **6**: p. 1-12.

92. Dominko, R., *Li_2MSiO_4 (M = Fe and/or Mn) cathode materials.* Journal of Power Sources, 2008. **184**(2): p. 462-468.

93. Aravindan, V., K. Karthikeyan, S. Ravi, S. Amaresh, W.S. Kim, and Y.S. Lee, *Adipic acid assisted sol–gel synthesis of Li_2MnSiO_4 nanoparticles with improved lithium storage properties.* Journal of Materials Chemistry, 2010. **20**(35): p. 7340-7343.

94. Gummow, R. and Y. He, *Recent progress in the development of Li_2MnSiO_4 cathode materials.* Journal of Power Sources, 2014. **253**: p. 315-331.

95. Gummow, R.J., *Li_2MnSiO_4 Nanostructured Cathodes for Rechargeable Lithium-Ion Batteries*, in *Nanomaterials in Advanced Batteries and Supercapacitors*, K.I. Ozoemena and S. Chen, Editors. 2016, Springer International Publishing: Switzerland. p. 29.

96. Gummow, R.J. and Y. He, *Recent progress in the development of Li_2MnSiO_4 cathode materials.* Journal of Power Sources, 2014. **253**: p. 315-331.

97. Dominko, R., M. Bele, M. Gaberšček, A. Meden, M. Remškar, and J. Jamnik, *Structure and electrochemical performance of Li_2MnSiO_4 and Li_2FeSiO_4 as potential Li-battery cathode materials.* Electrochemistry Communications, 2006. **8**(2): p. 217-222.

98. Nytén, A., S. Kamali, L. Häggström, T. Gustafsson, and J.O. Thomas, *The lithium extraction/insertion mechanism in Li_2FeSiO_4.* Journal of Materials Chemistry, 2006. **16**(23): p. 2266-2272.

99. Arroyo-deDompablo, M., R. Dominko, J. Gallardo-Amores, L. Dupont, G. Mali, H. Ehrenberg, J. Jamnik, and E. Moran, *On the energetic stability and electrochemistry of Li_2MnSiO_4 polymorphs.* Chemistry of Materials, 2008. **20**(17): p. 5574-5584.

100. Gummow, R.J., N. Sharma, V.K. Peterson, and Y. He, *Synthesis, structure, and electrochemical performance of magnesium-substituted lithium manganese orthosilicate cathode materials for lithium-ion batteries.* Journal of Power Sources, 2012. **197**: p. 231-237.

101. Kokalj, A., R. Dominko, G. Mali, A. Meden, M. Gaberscek, and J. Jamnik, *Beyond One-Electron Reaction in Li Cathode Materials: Designing $Li_2Mn_xFe_{1-x}SiO_4$.* Chemistry of Materials, 2007. **19**(15): p. 3633-3640.

102. Prosini, P.P., M. Lisi, D. Zane, and M. Pasquali, *Determination of the chemical diffusion coefficient of lithium in $LiFePO_4$.* Solid State Ionics, 2002. **148**(1): p. 45-51.

103. Levi, M.D. and D. Aurbach, *Diffusion coefficients of lithium ions during intercalation into graphite derived from the simultaneous measurements and modeling of electrochemical impedance and potentiostatic intermittent titration characteristics of*

thin graphite electrodes. The Journal of Physical Chemistry B, 1997. **101**(23): p. 4641-4647.

104. Bensalah, N. and H. Dawood, *Review on Synthesis, Characterizations, and Electrochemical Properties of Cathode Materials for Lithium Ion Batteries.* Jounal of Material Science & Engineering, 2016. **5**(4): p. 1-22.
105. Chen, Z., Y. Qin, K. Amine, and Y.-K. Sun, *Role of surface coating on cathode materials for lithium-ion batteries.* Journal of materials chemistry, 2010. **20**(36): p. 7606-7612.
106. Zuo, D., G. Tian, X. Li, D. Chen, and K. Shu, *Recent progress in surface coating of cathode materials for lithium ion secondary batteries.* Journal of Alloys and Compounds, 2017.
107. Geim, A.K. and K.S. Novoselov, *The rise of graphene.* Nature materials, 2007. **6**(3): p. 183-191.
108. Brownson, D.A., D.K. Kampouris, and C.E. Banks, *An overview of graphene in energy production and storage applications.* Journal of Power Sources, 2011. **196**(11): p. 4873-4885.
109. Hummers Jr, W.S. and R.E. Offeman, *Preparation of graphitic oxide.* Journal of the American Chemical Society, 1958. **80**(6): p. 1339-1339.
110. Kucinskis, G., G. Bajars, and J. Kleperis, *Graphene in lithium ion battery cathode materials: A review.* Journal of Power Sources, 2013. **240**: p. 66-79.
111. Woodyard, J.R., *Nonlinear circuit device utilizing germanium*. 1950, Google Patents.
112. Kamarulzaman, N. and M.H. Jaafar, *Synthesis and Stoichiometric Analysis of a Li-Ion Battery Cathode Material*, in *Stoichiometry and Materials Science - When Numbers Matter*. 2012, InTech: Slavka Krautzeka 83/A, 51000 Rijeka, Croatia. p. 16.
113. Julien, C.M., A. Mauger, J. Trottier, K. Zaghib, P. Hovington, and H. Groult, *Olivine-Based Blended Compounds as Positive Electrodes for Lithium Batteries.* Inorganics, 2016. **4**(2): p. 1-12.
114. Sadeghi, B., R. Sarraf-Mamoory, and H. Shahverdi, *Surface modification of $LiMn_2O_4$ for lithium batteries by nanostructured $LiFePO_4$ phosphate.* Journal of Nanomaterials, 2012. **2012**: p. 1-7.
115. Qiu, C., L. Liu, F. Du, X. Yang, C. Wang, G. Chen, and Y. Wei, *Electrochemical performance of $LiMn_2O_4$/$LiFePO_4$ blend cathodes for lithium ion batteries.* Chemical Research in Chinese Universities, 2015. **31**(2): p. 270-275.

116. Yun, J.-S., S. Kim, B.-W. Cho, K.-Y. Lee, K.Y. Chung, and W. Chang, *Synthesis and electrochemical properties of $Li_3V_2(PO_4)_3$-$LiMnPO_4$ composite cathode material for lithium-ion batteries.* Bulletin of the Korean Chemical Society, 2013. **34**(2): p. 433-436.

117. Myung, S.-T., M.H. Cho, H.T. Hong, T.H. Kang, and C.-S. Kim, *Electrochemical evaluation of mixed oxide electrode for Li-ion secondary batteries: $Li_{1.1}$ $Mn_{1.9}O_4$ and $LiNi_{0.8}Co_{0.15}Al_{0.05}O_2$.* Journal of power sources, 2005. **146**(1): p. 222-225.

118. Makhonina, E., A. Medvedeva, V. Dubasova, V. Pervov, and I. Eremenko, *$LiFePO_4$–$LiMn_2O_4$ composite cathode materials for lithium-ion batteries.* Inorganic Materials, 2015. **51**(12): p. 1264-1269.

119. Ren, H., Y. Guo, Z. Chen, X. Zhang, Z. Zhang, Y. Li, Q. Zhang, Q. Wu, and J. Li, *Synergetic effects of blended materials for Lithium-ion batteries.* Science China Technological Sciences, 2016. **59**(9): p. 1370-1376.

120. Aurbach, D., B. Markovsky, G. Salitra, E. Markevich, Y. Talyossef, M. Koltypin, L. Nazar, B. Ellis, and D. Kovacheva, *Review on electrode - Electrolyte solution interactions, related to cathode materials for Li-ion batteries.* Journal of Power Sources, 2007. **165**(2): p. 491-499.

121. Miao, C., P. Bai, Q. Jiang, S. Sun, and X. Wang, *A novel synthesis and characterization of $LiFePO_4$ and $LiFePO_4$/C as a cathode material for lithium-ion battery.* Journal of Power Sources, 2014. **246**: p. 232-238.

122. Jegal, J.-P. and K.-B. Kim, *Carbon nanotube-embedding $LiFePO_4$ as a cathode material for high rate lithium ion batteries.* Journal of Power Sources, 2013. **243**: p. 859-864.

123. Gong, C., Z. Xue, S. Wen, Y. Ye, and X. Xie, *Advanced carbon materials/olivine $LiFePO_4$ composites cathode for lithium ion batteries.* Journal of Power Sources, 2016. **318**: p. 93-112.

124. Zhu, H., H. He, X. Xin, X. Ma, L. Zan, and Y. Zhang, *Facile synthesis of Li_2MnSiO_4/C/graphene composite with superior high-rate performances as cathode materials for Li-ion batteries.* Electrochimica Acta, 2015. **155**: p. 116-124.

125. Dominko, R., M. Bele, A. Kokalj, M. Gaberscek, and J. Jamnik, *Li_2MnSiO_4 as a potential Li-battery cathode material.* Journal of Power Sources, 2007. **174**(2): p. 457-461.

126. Whitacre, J., K. Zaghib, W. West, and B. Ratnakumar, *Dual active material composite cathode structures for Li-ion batteries.* Journal of Power Sources, 2008. **177**(2): p. 528-536.
127. Chikkannanavar, S.B., D.M. Bernardi, and L. Liu, *A review of blended cathode materials for use in Li-ion batteries.* Journal of Power Sources, 2014. **248**: p. 91-100.
128. Wang, F., J. Chen, C. Wang, and B. Yi, *Fast sol–gel synthesis of mesoporous Li_2MnSiO_4/C nanocomposite with improved electrochemical performance for lithium-ion batteries.* Journal of Electroanalytical Chemistry, 2013. **688**: p. 123-129.
129. Bini, M., S. Ferrari, C. Ferrara, M.C. Mozzati, D. Capsoni, A.J. Pell, G. Pintacuda, P. Canton, and P. Mustarelli, *Polymorphism and magnetic properties of Li_2MSiO_4 (M = Fe, Mn) cathode materials.* Scientific Reports, 2013. **3**: p. 1-7.
130. Zeng, Y., *Role of PO_4 tetrahedron in $LiFePO_4$ and $FePO_4$ system.* Microscopy research and technique, 2015. **78**(6): p. 462-471.
131. Iltchev, N., Y. Chen, S. Okada, and J.-i. Yamaki, *$LiFePO_4$ storage at room and elevated temperatures.* Journal of power sources, 2003. **119**: p. 749-754.
132. Qin, X., X. Wang, H. Xiang, J. Xie, J. Li, and Y. Zhou, *Mechanism for hydrothermal synthesis of LiFePO4 platelets as cathode material for lithium-ion batteries.* The Journal of Physical Chemistry C, 2010. **114**(39): p. 16806-16812.
133. Oghbaei, M., F. Baniasadi, and S. Asgari, *Lithium iron silicate sol–gel synthesis and electrochemical investigation.* Journal of Alloys and Compounds, 2016. **672**: p. 93-97.
134. Zhang, S., C. Deng, F.L. Liu, Q. Wu, M. Zhang, F.L. Meng, and H. Gao, *Impacts of in situ carbon coating on the structural, morphological and electrochemical characteristics of Li_2MnSiO_4 prepared by a citric acid assisted sol–gel method.* Journal of Electroanalytical Chemistry, 2013. **689**: p. 88-95.
135. Hwang, C., T. Kim, J. Shim, K. Kwak, K.M. Ok, and K.-K. Lee, *Fast ultrasound-assisted synthesis of Li_2MnSiO_4 nanoparticles for a lithium-ion battery.* Journal of Power Sources, 2015. **294**: p. 522-529.
136. Steenkamp, J. and J. Basson, *The manganese ferroalloys industry in southern Africa.* Journal of the Southern African Institute of Mining and Metallurgy, 2013. **113**(8): p. 667-676.
137. *Facts and Figures 2016*, R. Baxter, Editor. 2017, Chamber of Mines of South Africa: 5 Hollard Street, Johannesburg 2001, South Africa. p. 40.

138. Xie, M., R. Luo, R. Chen, F. Wu, T. Zhao, Q. Wang, and L. Li, *Template-Assisted Hydrothermal Synthesis of Li_2MnSiO_4 as a Cathode Material for Lithium Ion Batteries.* ACS applied materials & interfaces, 2015. **7**(20): p. 10779-10784.

CHAPTER 2

Chapter Overview

This chapter looks at the methodologies used to synthesise the pristine cathode materials, graphene nanosheets and blending of these materials to form graphenised hybrid cathode materials. The selected characterization techniques were used to study the structural, morphological and electrochemical properties of the prepared nanomaterials. The results obtained from these characterization techniques are discussed in the next chapter.

2. Methodology

2.1. Introduction

The battery technology has developed into being a very essential part of our lives. It promotes the generation of clean energy supply, also featured/used in electric and hybrid-electric vehicles, and many electronic devices would not be viable without batteries [1]. Another interesting aspect about this technology is the integration of green and sustainable precursors that were not used before. The use of toxic elements such Ni and Cd is being replaced with more environmentally friendly materials such as Fe and Mn.

Different synthetic methods have been developed and utilised to prepare various cathode materials such as sol-gel, hydrothermal, solvothermal, solid-state reaction, co-precipitation, spray pyrolysis, emulsion-drying and microwave method. These techniques produce unique nanoarchitectures with different physical and chemical properties [2]. The sol-gel approach offers better mixing of reagents which leads to homogeneous particle size distribution in the final product [3]. In addition, the technique allows the ease to control stoichiometry, produce nanoparticles with uniform size and morphology, and the obtained products show higher purity compared to those prepared by other methods [4-7]. This technique was adopted for the preparation of pristine $LiFePO_4$, Li_2MnSiO_4, $LiFePO_4$-Li_2MnSiO_4 and graphenised $LiFePO_4$-Li_2MnSiO_4 hybrid cathode materials due to its simplicity, less energy consumption

and there is no expensive equipment required during synthesis. For comparative studies, the hybrid cathode materials were also prepared using a hand milling approach.

Mechanical milling is a convenient way of blending, synthesising and reducing particle size of nanomaterials [8]. This technique enables mixing of powder samples using a high energy mill in a suitable medium such as a solvent or gas flow [9]. During the milling process, the balls roll or freely fall inside the chamber to impact the powder samples underneath. Optimum results are obtained by tuning reaction parameters such as milling speed, temperature, time, size distribution of the balls and the type of milling machine [8]. This is a time consuming process and high energy mills may alter the structure and morphology of the products. Alternatively, this study explores the use of a hand milling approach to prepare the hybrid cathode material. This technique is simpler and softer than mechanical milling.

2.2. Chemical Reagents

Graphite powder (<20 μm, synthetic), Sulfuric acid (H_2SiO_4, ACS reagent, 95.0 – 98.0 %), Potassium manganese oxide ($KMnO_4$, ACS reagent, ≥99.0 %), Hydrogen peroxide (H_2O_2, contains inhibitor, 30 wt. % in H_2O), Hydrochloric acid (HCl, 36.5 – 38 %) Sodium borohydride ($NaBH_4$, granular, 10 – 40 mesh, 98 %), Lithium acetate ($LiOOCH_3$, 99.95% trace metals basis), Iron (II) acetate ($Fe(OOCH_3)_2$, ≥99.99 % trace metal basis), Ammonium phosphate dibasic ($(NH_4)_2HPO_4$, reagent grade, ≥98.0 %), Tetraethyl orthosilicate ($Si(OC_2H_2CH_3)_4$, ≥99.0 % (GC)), Manganese acetate tetrahydrate ($(CH_3COO)_2Mn•4H_2O$, 99.99 % trace metals basis), Ammonia solution (2.0 M in methanol), Lithium perchlorate ($LiClO_4$, ≥98.0 %) and N-Methyl-2-pyrolidone (C_5H_9NO, anhydrous, 99.5 %) were all purchased from Sigma-Aldrich South Africa, except Alumina (0.05, 0.3 and 1.0 μm) which were purchased from Buehler and used as received.

2.3. Synthesis of Pristine $LiFePO_4$

The synthesis of pristine $LiFePO_4$ (LFP) nanoparticles was carried out using the sol-gel method [6]. Three solutions of 0.005 mol $Fe(OOCCH_3)_2$, $(NH_4)_2HPO_4$ and $Li(OOCCH_3)$ were prepared using a mixture of water and ethanol in a ratio of 3:1 (V/V). The iron (II) acetate solution was slowly added (over a period of 5 min) to that of ammonium phosphate dibasic and vigorously stirred for 30 min under N_2 gas flow. This was followed by another slow addition of lithium acetate and continued stirring of the mixture for 2.5 h while maintaining N_2 gas flow. A gel was formed by slow evaporation of the solvent at 70 ºC using an oil-bath over a period of 24 h. The formulated gel was then dried in a vacuum oven at 80 ºC overnight. Pristine $LiFePO_4$ nanoparticles were obtained by grounding the dried powder and calcining at 700 ºC for 7 h.

2.4. Synthesis of Pristine Li_2MnSiO_4

Pristine Li_2MnSiO_4 (LMS) nanoparticles were also prepared by following the sol-gel approach. Three solutions were prepared by dissolving 0.01 mol $Li(OOCCH_3)$, 0.005 mol $(CH_3COO)_2Mn•4H_2O$ and 0.005 mol $Si(OC_2H_5)_4$ in 25 mL of a mixture of water and ethanol in a ratio of 3:1 (V/V). The lithium acetate solution was mixed with the one for manganese acetate tetrahydrate and stirred for 30 min under N_2 gas flow. This was followed by slow addition of tetrataethyl orthosilicate and 1.0 mL of ammonia solution. A sol was formed by stirring the mixture for 2.5 h still maintaining the N_2 gas flow. The sol was then evaporated at 70 ºC overnight to form a thick gel. The desired product, pristine LMS was obtained by drying the gel in a vacuum oven at 80 ºC overnight, grounded the powder and then calcination at 700 ºC for 6 h.

2.5. Synthesis of Graphene Nanosheets

The graphene oxide nanosheets were synthesized from graphite powder by following a modified Hummer's method [10]. The synthesis was initiated by adding 2.0 g of graphite powder into 40 mL of concentrated H_2SO_4 into a clean dry conical flask and stirred at room

temperature for 1 h. The flask was cooled to a temperature below 5 ºC in an ice bath and then followed by slow addition of 7.0 g of $KMnO_4$. The mixture was allowed to warm-up to room temperature (without using heat) and then immersed in a warm water bath to raise the temperature to 35 ºC. Thereafter, the mixture was stirred for 2 h and returned back to the ice bath, followed by slow addition of 100 mL of de-ionised water and 10 mL of hydrogen peroxide until gas evolution ceased. The flask was removed from the ice bath and stirred for 0.5 h at room temperature. The resultant suspension was washed thoroughly with de-ionised water to remove residues of un-exfoliated graphite. Finally, graphene oxide nanosheets were obtained by drying the resultant suspension at 65 ºC in an oven overnight.

Reduced graphene oxide (graphene) was prepared by dispersing 200 mg of graphene oxide into 100 mL of deionised water using an ultrasonic bath for 1 h. This was followed by two successive slow additions of 200 mg of $NaBH_4$ with a 30 min difference in between while the mixture was stirred at room temperature. The mixture was refluxed at 125 ºC for 4 h under stirring. The formulated black suspension was allowed to cool to room temperature and isolated using a centrifuge. Thereafter, properly washed with deionised water and dried overnight at 65 ºC in a vacuum oven.

2.6. Synthesis of Hybrid Cathode Materials

2.6.1. *In situ* Sol-Gel Method

A 1:1 mass of $LiFePO_4$-Li_2MnSiO_4 hybrid cathode material was synthesized by dissolving equimolar amounts (0.0025 mol) of $Li(OOCCH_3)$, $(Fe(OOCCH_3)_2)$ and $((NH_4)_2HPO_4)$ into 25 mL of a mixture of water and ethanol in a ratio of 3:1 (V/V). A sol was formed as described before and into this, 200 mg of the already prepared LMS were added. The mixture was vigorously stirred at room temperature for 1 h and then the temperature was increased to 70 ºC overnight in order to evaporate the solvent and form a thick gel. The gel was dried in a vacuum oven at 80 ºC for 24 h. Finally, the hybrid cathode material denoted as LFP-LMS SG was obtained by grinding the powder and calcining at 700 ºC for 7 h. Graphenised $LiFePO_4$-Li_2MnSiO_4 (LFP-LMS-G SG) was prepared the same way as LFP-LMS with an addition of 25 mg of graphene.

2.6.2. Hand Hilling Method

A 1:1 mass ratio of $LiFePO_4$-Li_2MnSiO_4 (denoted as LFP-LMS HM) hybrid cathode material was obtained by grinding equal masses (200 mg) of pristine $LiFePO_4$ and Li_2MnSiO_4 using a pestle and a mortar for 15 min. The finely grounded powder was calcined at 350 ºC for 4 h. The graphenised Li_2MnSiO_4-$LiFePO_4$ (denoted as LFP-LMS-G HM) hybrid cathode material was prepared the same as LFP-LMS HM hybrid cathode, but with the addition of 25 mg of graphene.

2.7.Material Characterization

2.7.1. High Resolution Scanning Electron Microscopy

Scanning electron microscopy (SEM) is an essential imaging technique used not only to investigate topographic and morphological properties, but also microstructural composition of a sample. The information is obtained by scanning the surface of a sample with a high beam of electrons. Unlike conventional microscopes, SEM creates 3D images using electrons rather than light waves [11, 12].

An electron gun is used to generate a beam of high energy electrons which are focused on the specimen using a series of magnification lenses. When the beam of electrons strikes the surface of the sample, they bounce back in the form of backscattered electrons, secondary electrons, x-rays, light and heat, and carry with them crucial information about the surface of the specimen undergoing analysis. The secondary and backscattered electrons are used for imaging and the created images appear black and white, because they are created using electrons rather than light waves. The scattered x-rays are used to identify elemental composition and are captured using a technique called energy dispersive x-ray spectroscopy, to be discussed in the sub-sessions (EDS) [11].

The samples were placed on carbon tapes supported by a specimen pins and sputter-coated using fine graphite pencil to improve their conductivity. These samples were analysed using Zess Geminin Auriga Field Emission Scanning Electron Microscopy.

2.7.2. High Resolution Transmission Electron Microscopy

Transmission electron microscopy is another valuable imaging technique similar to SEM. However, this technique uses very high energized electrons that penetrate through an ultra-thin specimen. The interaction of the sample and electrons produces vital information about the specimen being studied. The transmitted electrons carry information about the morphologic, crystallographic and compositional properties of the sample [11].

The operating principle in TEM is similar to that of an optical microscope, but uses electrons instead of a light source. The resolution of an optical microscope is very poor and this is imposed by high wavelengths of visible light (400 – 700 ηm). Therefore, nanoparticles that are separated by a very short distance (nanometer scale) will not be resolved by these instruments [13]. These limitations were eliminated by introducing TEM, a technique which uses electrons to study the properties of a sample. The wavelength of electrons is much lower than that of light therefore making the resolution of TEM instrument to be thousand times better than that of a light microscope.

Electrons are generated in a thermionic gun by a process called thermionic-discharge. They are then accelerated and focused on a sample by an electric field and magnetic field, respectively [13]. Some of these electrons are transmitted, while others are scattered depending on the thickness of the sample. The transmitted electrons are magnified and focused onto an imaging device such as a fluorescent screen or charge coupled device for viewing the image of the specimen. The screen will show dark and light regions which represent an image of the specimen. The dark areas represent a dense portion of the specimen and electrons are absorbed, and the lighter areas are regions where the specimen is less dense and electrons are able to penetrate through.

The samples were dispersed in ethanol and drop-coated on a Cu-Ni grid and dried under a UV lamp for 5 min. Analysis were performed using a Tecnai G2 F20 X-Twin MAT 200 kV Field Emission TEM instrument.

2.7.3. Energy Dispersive X-ray Spectroscopy

Energy dispersive X-ray spectroscopy (EDS) is an analytical tool used for elemental analysis for a material. It gives the relative proportions of each element in a sample undergoing investigation. The technique is used in conjugation with SEM and TEM, and utilises the X-rays spattered by a sample when bombarded by a beam of electrons. The different elements are easily identified, because each element on the periodic table has a distinctive electronic structure and triggers a unique response to the electromagnetic waves [13].

Samples that are composed of elements with higher molecular weights are easily detected with most instruments as opposed to low molecular weight elements like Li. Elements with molecular weights lower than Beryllium (Be) are barely detected in most EDS techniques. In some cases elements with an atomic mass that is below that of sodium (Na) cannot be detected due to the use of Si-Li detectors covered by beryllium window [11]. As highlighted above; the technique is in conjugation with SEM and TEM, therefore the preparation technique is the same.

2.7.4. X-ray Diffraction (XRD)

X-ray diffraction (XRD) is a non-contact and non-destructive characterization technique that is commonly used for investigating the crystal structure, size and interplane distance between atoms of a material. This technique is also a perfect fit for identification of impurity phases that could change the structure, thereby affecting performance deliverables of a material [12].

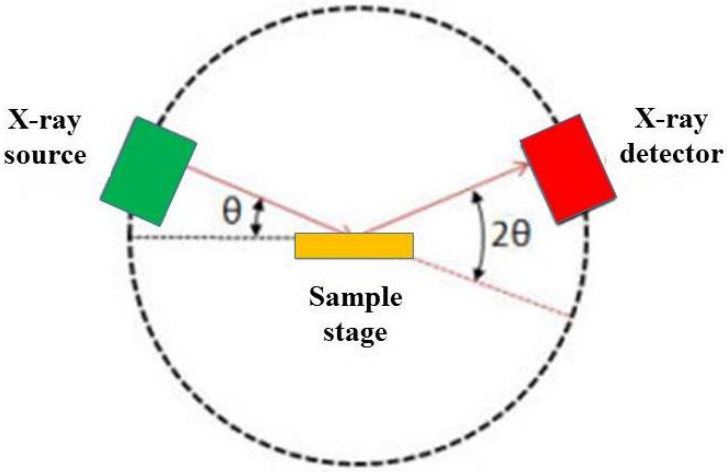

Figure 5: Basic components of an X-ray diffractometer

A typical X-ray diffractometer consist of (i) an X-ray source, (ii) specimen stage (iii) receiving optics and (iv) X-ray detector as shown in Fig. 5. For XRD analysis, the X-ray source produces a beam of X-ray which is incident on the sample at different angles [14]. The atoms in a sample will cause scattering of the beams and if these (scattered beams) are in phase will interfere constructively. This leads to diffraction peaks which are characteristic to the structure of the material [15]. Precisely, XRD works on the principle of Bragg's Law [16]:

$$2d_{\mathrm{hkl}} \sin\theta = n\lambda \tag{9}$$

where, d_{hkl} is the interplanar spacing between two consecutive planes characterized by Miller indices (*h k l*), Θ is the diffraction angle, *n* is the order of diffraction and λ is the wavelength of the reflected X-ray. The crystallite size can also be calculated using the Scherrer equation [17]:

$$\beta\cos(\theta) = \frac{\kappa\lambda}{D_{\mathrm{v}}} \tag{10}$$

where D_v is the crystallite size, β is the full-width-at-half-maximum (FWHM) of the reflected XRD peak and k is Scherrer constant which is influenced by how the width is determined, crystal shape, and size distribution.

The X-ray diffraction patterns of the synthesized samples were characterized using a D8 Advanced diffractometer from Bruker AXS using an X-ray tube with copper K-alpha radiation operated at 40 kV and 40 mA and a position sensitive detector Vantec_1 used for fast acquisition of data.

2.7.5. Fourier Transform Infrared (FTIR) Spectroscopy

The structure and functional group analysis of the prepared samples were obtained by using Fourier Transform Infrared (FTIR) spectroscopy. This technique takes advantage of the covalent bonds of both organic and inorganic compounds which absorb different frequencies of radiation in the infrared (IR) region of the electromagnetic spectrum.

For IR analysis, IR radiation is incident on the sample and some of this energy (in the form of frequency) will be transmitted and the remaining will be absorbed. The absorbed frequencies are quantised, therefore will differ for each molecule. Each molecule will absorb a unique set of frequencies (like a fingerprint, no two molecules, unless they are the same will have the same infrared spectrum) depending on their structure, which is the arrangement of atoms around the nucleus [18-20]. This makes IR spectroscopy a powerful technique for structural analysis. Furthermore, the bands that are observed in the IR spectrum represent the stretching and bending vibration modes which are attributed to covalent bonds and functional groups that are found in that compound or sample of interest [18-20].

The functional group analysis of the prepared nanomaterials was performed using Perkin Elmer spectrum 100 series attenuated total reflection (ATR) FTIR spectrometer. Potassium bromide (KBr) was finely grounded and pressed under high pressures to produce a KBr pellet (clear/glass-like flat pellet) which served as the background for all sample runs. Each powder

sample were mixed with KBr, grounded and pressed under high pressures to produce pellets which were analysed. The data was extracted and plotted using Origin software.

2.7.6. Raman Spectroscopy

Raman spectroscopy is an essential analytical technique used for identification of vibrational (phonon) states of a material through inelastically scattered radiation. In Raman spectroscopy, a monochromatic light source (laser beam) is used to excite molecules of a sample from their ground vibrational state to the virtual (excited) state, as illustrated in Fig. 6. The molecules that instantly return back to their ground state represent Rayleigh scattering and their excitation energy is equal to the emitted energy. Sometimes the molecules are excited to the virtual state and when relaxation occurs they fall on the vibrational states (Stokes scattering) and are characterised by low emission energy compared to the incident photon. While majority of the molecules undergo Rayleigh scattering, a small fraction of them undergoes Raman/Anti-Stokes scattering (inelastic scattering) and are characterised by loss of energy (emission of higher energy than the incident photon) [11, 21].The inelastically scattered light carries information characteristic to the vibrational modes of a molecule.

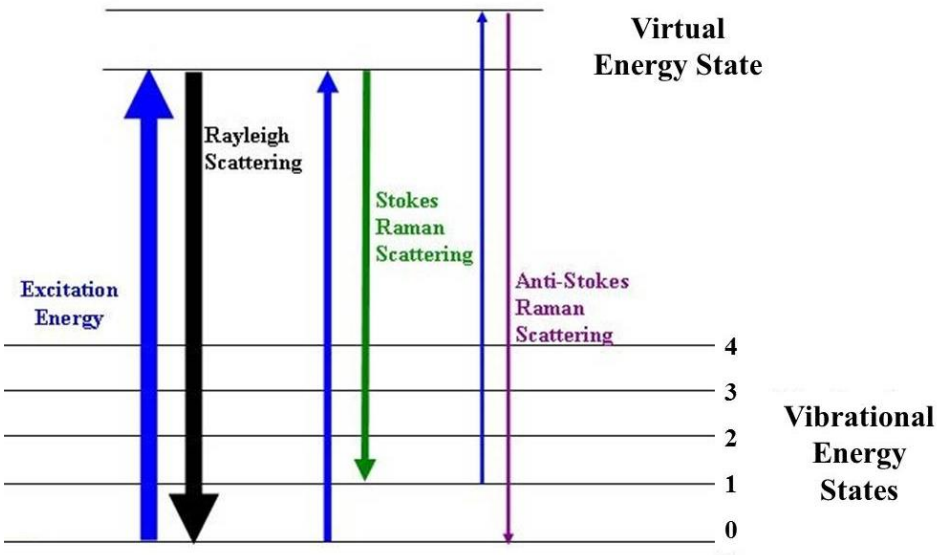

Figure 6: Principle of Raman spectroscopy

Raman spectroscopy studies are closely related to those of FTIR Spectroscopy because both techniques give information about the vibrational states of a molecule. Vibrations that produce strong signals in one technique will produce weak signals in the other. Raman spectroscopy works well with non-polar functional groups, however gives insignificant signals for molecules with a dipole moment. The opposite is true for FTIR spectroscopy [21].

The powder samples were held on a glass slide using greece and left to dry for 1 hr before analysis with XploRA one Raman Microscope (Horiba Scientific) controlled using VisionPro software.

2.7.7. Thermogravimetric Analysis

Thermogravimetric Analysis (TGA) is used to measure the amount and rate of change in the mass of a material as a function of temperature or time while the sample is subjected to a controlled temperature program and atmospheric conditions. TGA measurements are used to determine the composition and thermal stabilities of a material [22].

Thermogravimetric analysers are equipped with a sensitive analytical balance (thermo-balance), temperature programmable furnace, gas purge system (for providing desired atmospheric conditions) and a microprocessor for controlling the instrument and data acquisition. The detection limits of a thermo-balance can be as high as 0.1 μg, and the instrument only requires a small amount of sample ranging between 1 to 100 mg [23]. Furthermore, the latest furnace is capable of heating the sample to temperatures up to 1600 ºC at a variety of heating rates with 1 to 20 ºC min^{-1} being the most commonly used. Finally, the environment inside the furnace is controlled by purging gas (usually N_2 or Ar) at a flow rate of 50 - 100 mL min^{-1} to provide an atmospheric pressure of roughly 10^{-3} to 10^{-4} Pa [23].

TG measurements are conducted by adding a sample into the pan and placing it inside the furnace. The furnace is heated using a temperature programme and the various changes associated with mass loss or gain are monitored throughout the experiment. Majority of the samples will undergo mass loss because they are heated and processes such as dehydration, decomposition, sublimation and in some cases, reduction of metal oxides to metals are bound

to happen. Mass gain can also be observed even though a sample is heated. This is associated with chemical reactions between the material and the gas inside the testing environment [23].

The acquired data is obtained in the form of a thermogravimetric (TG) curve which is a plot of mass loss as a function of temperature or time. Thermogravimetric curves provide crucial information about a material's reaction mechanism, reaction intermediates and final reaction products that are formed after the decomposition process. The power of this is enhanced by coupling it with other technique such as FTIR to confirm the functional groups of the compounds that have been ruptured during treatment with high temperatures.

The thermal stabilities of the prepared powder samples were analysed using a TGA Analyser 4000 (Perkin Elmer) controlled by Pyris software under N_2 atmosphere in the temperature range of 30 to 900 ºC at a heating rate of 20 ºC min^{-1}.

2.7.8. Small Angle X-ray Scattering (SAXS)

Small angle X-ray scattering (SAXS) is a non-intrusive technique used for investigating the structure, morphology and particle size of nanomaterials. This technique gives precise information (nanoparticle shape, size, size distribution and surface structure) of a material in their natural environment [24]. It is also complementary to direct imaging and structural characterization techniques such as scanning and transmission electron microscopy (SEM and TEM) [25]. SAXS is unique and more advantageous than these techniques. Sample analysis using SEM and TEM is only limited to a specific area where the image was taken. As a result the image is usually used to generalise the representation of the entire sample. The advantage of using SAXS is that it provides information about the entire sample rather than just focusing on a single spot which is usually a challenge for the above mentioned microscopic techniques [24].

A SAXS instrument consists of an X-ray source, collimation system, sample holder, beam stop and a detector system, as shown in Fig. 7. During sample analysis a beam of X-ray is produced by the X-ray source and then narrowed by the collimator before reaching the sample [26]. When the beam of X-ray reaches the sample it gets scattered by nanoparticles in

the sample resulting to scattering patterns that are characteristic to the nanoparticle's shape, size and internal structure [27]. Before the X-rays reach the detectors they are surfed by a "beam stop" to prevent the passage of high intensity X-rays which might damage these detectors. In addition, the high intensity X-rays may also overshadow weak scattering produced by a material, therefore leading to poor results [26].

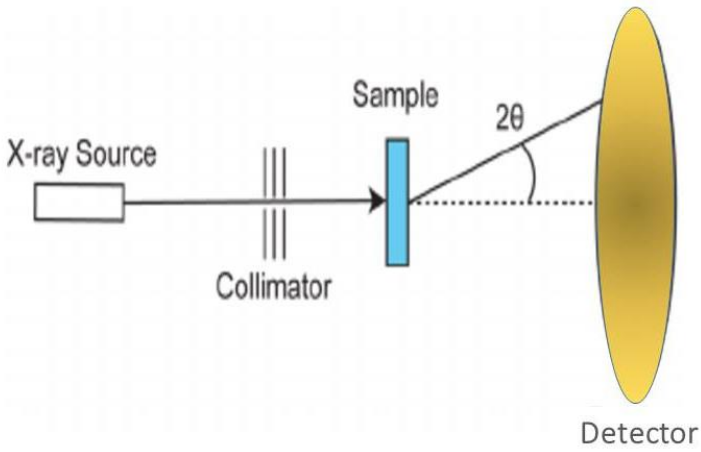

Figure 7: Schematic diagram of SAXSpace instrument

The finely grounded powders were prepared in between two layers of sticky tape, trimmed and fitted into the sample holder. SAXS measurements were obtained using a 1 mm diameter quartz capillary positioned at a distance of 317 mm from the SDD camera and temperature controlled at 20 ºC. Measurements were carried out using SAXSpace instrument (Anton Paar, GmbH, Australia) in line-collimation mode with an accessible q range of 0.0732 – 1.66 ηm. For each measurement, there were six frames obtained at 100 s exposure time and averaged. Data analysis was performed using the generalized indirect Fourier transformation (GIFT) software in order to determine the particle size and size distribution of the dispersions.

2.7.9. Electrochemical Characterization

2.7.9.1. Cyclic Voltammetry (CV)

Cyclic voltammetry (CV) is one of the simple and popularly used electrochemical techniques in the fields of analytical, physical and inorganic electrochemistry [28]. The technique is used as a preliminary step to determine the redox processes in a given analyte. These include, but not limited to the redox potentials, kinetics of an electron transport process and the number of electrons transferred by a material immobilised on the surface of an electrode or in a solution during an electrochemical reaction [29].

A typical CV experimental set-up consists of three electrodes; working, reference and counter electrode which are connected to a potentiostat. The potentiostat is used to control the potential on the counter electrode versus the working electrode so that the potential difference between the working and reference electrode is well defined and corresponds to the specified values [30]. During the experiment, a potential is applied on the working electrode and is varied from an initial value (E_i) to a final value E_f, (also known as a switching potential) at a constant scan rate leading to a single linear sweep. Once the E_f is reached, the potential can be reversed back to the Ei while maintaining the same scan rate to complete a cycle which consists of the forward and reverse sweeps [28], as indicated in Fig. 8.

These cycles can be repeated several times depending on the type of information needed by the analyst. As the potential is cycled (scanned back and forth) within a selected potential window the material will undergo either oxidation or reduction depending on the direction of the potential. When the scan is initiated from the negative potential to the positive potential the analyte will undergo oxidation. This is the region where the analyte's anodic peak current (I_{pa}) and potential (E_{pa}) are observed. The reverse scan will lead to the reduction of the analyte which is defined by the cathodic peak current (I_{pa}) and potential (E_{pa}) [29, 31].

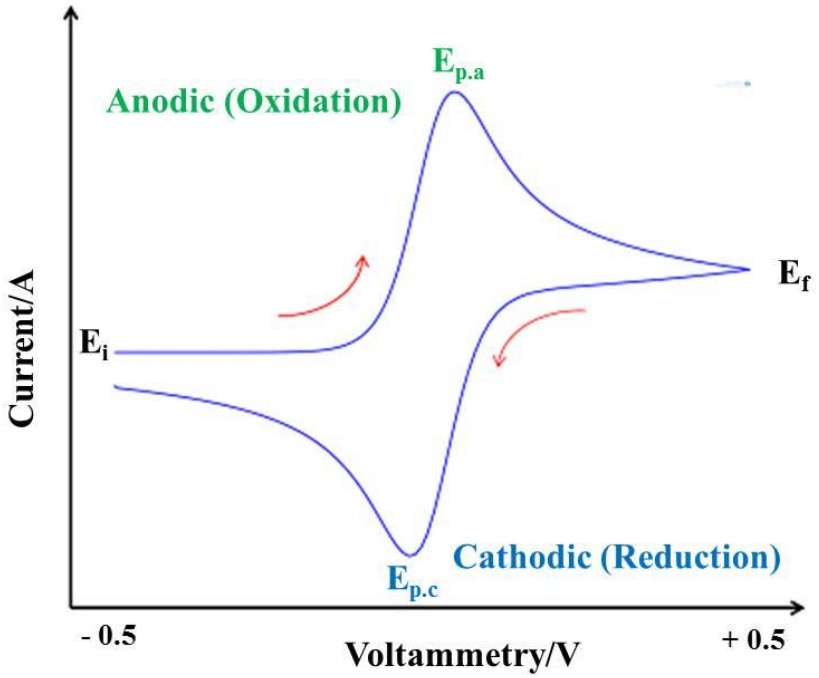

Figure 8: A typical cyclic voltammogram depicting oxidation and reduction peaks of an analyte between specified values of E_i and E_f (in this case -0.5 to 0.5 V)

There are several parameters that can be used to determine the reversibility of a given system. Reversibility refers to how fast a reaction can maintain the concentration of oxidised and reduced species in equilibrium at the surface of the electrode [29]. One of these parameters is the formal reduction potential and is obtained by taking the average of the forward and reverse potentials from the cyclic voltammogramms as defined by Equation 11.

$$E^{o} = \frac{(E_{pa} + E_{pc})}{2} \qquad (11)$$

Cyclic voltammograms can assume various shapes due to the nature of different redox processes of an analyte on the surface of the electrode. The shape of these curves (Fig. 9) is associated with the reversibility of the electrochemical process on the surface of an electrode.

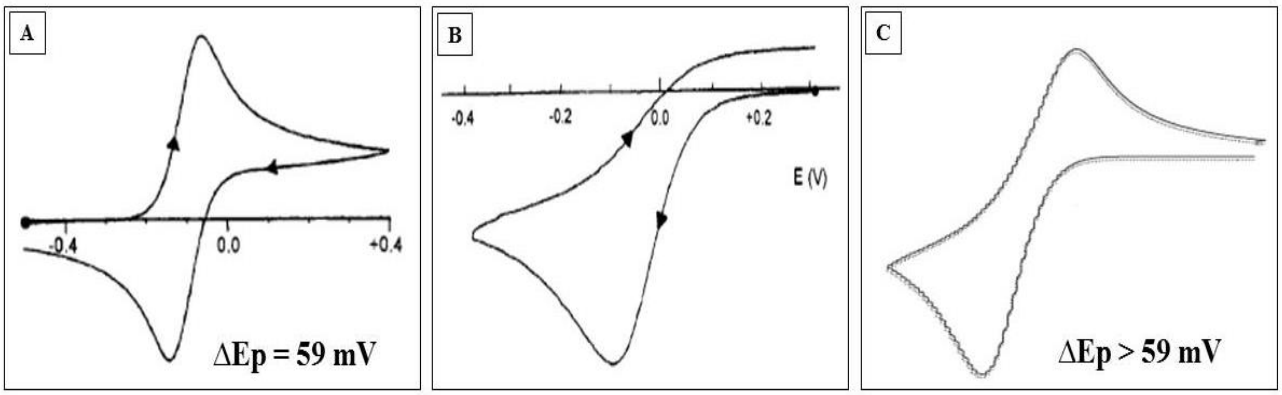

Figure 9: Cyclic voltammetry profiles for (A) reversible, (B) irreversible and (C) quasi-reversible processes

A reversible process is characterized by the shape of the cyclic voltammogram represented in Fig. 9 A). The anodic peak is the mirror image of the cathodic peak. Such electrode processes are classified to be reversible because the rate of the electron transfer is greater than the rate of the mass transport when an electrode is placed inside an electrolyte solution [28]. In cases where the electron transfer is less than that of the mass transport, then that process is defined as irreversible as indicated by Fig. 9 B. In such processes the peak-to-peak separation is very large and only the reduction peak is detected [28]. In a quasi-reversible process (Fig. 9 C), the electrode processes show a reversible behaviour at low scan rates, however it becomes irreversible at high scan rates [28].

The prepared cathode materials were dispersed in N-Methyl-2-Pyrrolidon to form a concentration of 5.0 mg mL^{-1} and sonicated for 1 h. The electrodes were prepared by casting 4 µL of the cathode materials on a glassy carbon electrode (GCE) and drying under a lamp for 48 h. A three electrode set-up was used and these electrodes were dipped into 3.0 mL of 1.0 M $LiClO_4$ electrolyte. The three electrodes were: (i) GCE modified with LFP, LMS, LFP-LMS HM, LFP-LMS-G HM, LFP-LMS SG and LFP-LMS-G SG, (ii) reference electrode – Ag/AgCl and (iii) counter electrode – platinum wire. Cyclic voltammetric experiments were carried out using CH instruments workstation (CHI760E).

2.7.9.2. Electrochemical Impedance Spectroscopy (EIS)

Electrochemical Impedance Spectroscopy (EIS) is an effective tool for studying and monitoring the functioning of batteries and fuel cells. It is also used in other application such as corrosion analysis and interfacial behaviour of different electrode systems [32]. Voltammetric techniques are used as a primary step to study the kinetics of an electrode process. However, their results are usually clouded by side effects such as the ohmic drop related to the experimental set-up or the charging currents of the double layer that occurs over a very short time-scale (order of millisecond) [33]. The problem with these side effects, more especially ohmic drop, is that the response of a reversible system becomes similar to that of a kinetically slow system. The best way to differentiate the kinetics of these reactions is to make use of an excitation function that will cover a large time domain [33]. In that way, EIS studies will be a complement to whatever that is obtained using voltammetric techniques and better explains the kinetics of an electrode process.

EIS experiments are performed by applying a sinusoidal voltage using a potentiostat across a three electrode cell containing an electrolyte solution to retain the analyte of interest [32]. The amplitude and magnitude of the fixed sinusoidal voltage is varied depending on the needs of the user. For example, biological molecules are usually subjected to low voltages to avoid denaturing, whereas this is not the case for non-biological molecules. When the voltage is applied on the electrode in a particular frequency range, current flows through the electrochemical cell and this response is recorded by the potentiostat and converted into impedance data which contains both real and imaginary component [32]. The obtained data requires a complex process of analysing which can be achieved by using designated EIS analysis software. An electrochemical cell is represented using an equivalent circuit of resistors and capacitors before analysis with the software [34]. The analysed data is usually presented in the form of a Nyquist plot or Bode plot, as shown by Fig. 10.

The Nyquist plot displays real impedance (Z') vs imaginary impedance (Z'') and is used to determine the solution resistance (R_s), charge transfer resistance (R_{ct}) and the Warburg element (W_o) of an electrochemical reaction on the electrode surface [32]. This type of plot gives insights about the electrochemical reactions on the surface of the electrode and

describes whether they occur via a kinetic or mass transfer controlled processes. The determining feature between the two processes is R_{ct} and will be large for an electrochemical system governed by kinetically controlled, whereas a significantly small R_{ct} value will be obtained for mass transfer controlled systems [34]. In addition, there is also a Bode plot which can be used to determine the capacitative or inductive effect of an electrochemical system [32]. This is a plot of impedance and phase angle against frequency as shown in Fig. 10 B.

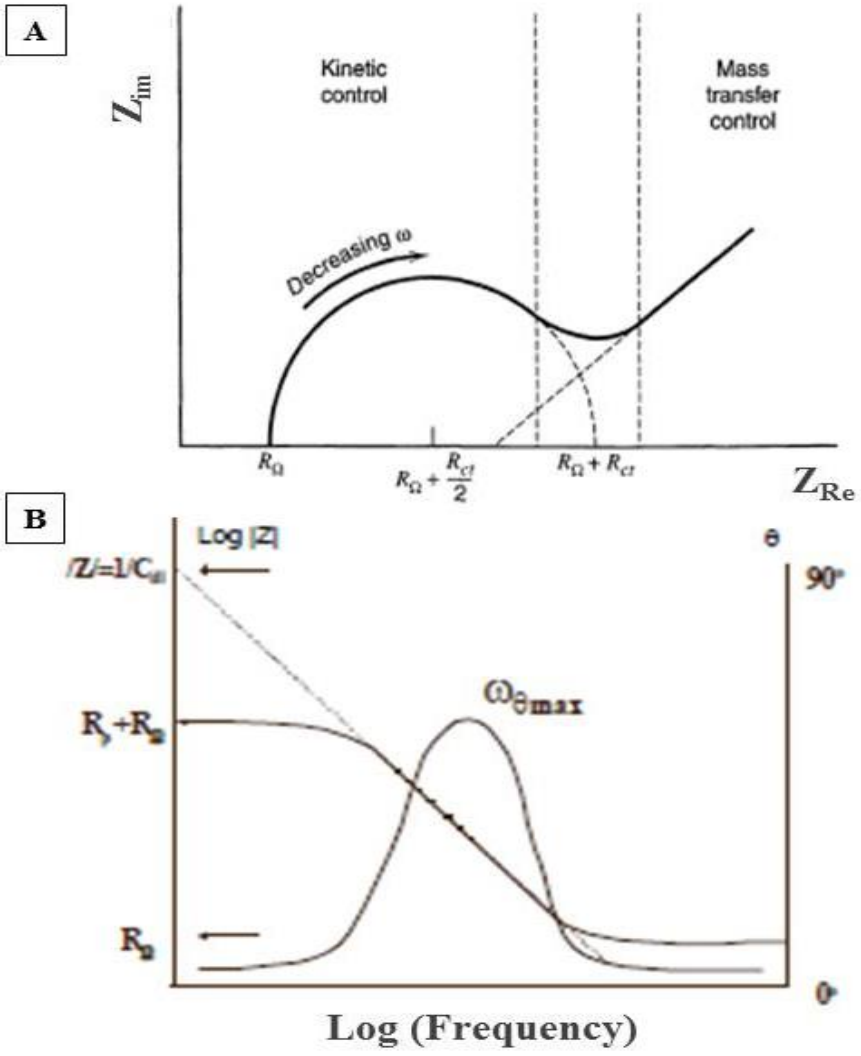

Figure 10: Electrochemical impedance depicted by (A) the Nyquist plot (taken from [34]) and (B) Bode plot (taken from [35])

REFERENCES

1. Satyavani, T., A.S. Kumar, and P.S. Rao, *Methods of synthesis and performance improvement of lithium iron phosphate for high rate Li-ion batteries: a review.* Engineering Science and Technology, an International Journal, 2016. **19**(1): p. 178-188.
2. Bensalah, N. and H. Dawood, *Review on Synthesis, Characterizations, and Electrochemical Properties of Cathode Materials for Lithium Ion Batteries.* Jounal of Material Science & Engineering, 2016. **5**(4): p. 1-22.
3. Kamarulzaman, N. and M.H. Jaafar, *Synthesis and Stoichiometric Analysis of a Li-Ion Battery Cathode Material*, in *Stoichiometry and Materials Science - When Numbers Matter*. 2012, InTech: Slavka Krautzeka 83/A, 51000 Rijeka, Croatia. p. 16.
4. Wang, F., J. Chen, C. Wang, and B. Yi, *Fast sol–gel synthesis of mesoporous Li_2MnSiO_4/C nanocomposite with improved electrochemical performance for lithium-ion batteries.* Journal of Electroanalytical Chemistry, 2013. **688**: p. 123-129.
5. Gong, Z. and Y. Yang, *Recent advances in the research of polyanion-type cathode materials for Li-ion batteries.* Energy & Environmental Science, 2011. **4**(9): p. 3223-3242.
6. Toprakci, O., H.A. Toprakci, L. Ji, and X. Zhang, *Fabrication and electrochemical characteristics of $LiFePO_4$ powders for lithium-ion batteries.* KONA Powder and Particle Journal, 2010. **28**: p. 50-73.
7. Oghbaei, M., F. Baniasadi, and S. Asgari, *Lithium iron silicate sol–gel synthesis and electrochemical investigation.* Journal of Alloys and Compounds, 2016. **672**: p. 93-97.
8. Yadav, T.P., R.M. Yadav, and D.P. Singh, *Mechanical milling: A top down approach for the synthesis of nanomaterials and nanocomposites.* Nanoscience and Nanotechnology, 2012. **2**(3): p. 22-48.
9. Arbain, R., M. Othman, and S. Palaniandy, *Preparation of iron oxide nanoparticles by mechanical milling.* Minerals Engineering, 2011. **24**(1): p. 1-9.
10. Hummers Jr, W.S. and R.E. Offeman, *Preparation of graphitic oxide.* Journal of the American Chemical Society, 1958. **80**(6): p. 1339-1339.

11. Joshi, M., A. Bhattacharyya, and S.W. Ali, *Characterization techniques for nanotechnology applications in textiles.* Indian Journal of Fibre & Textile Research, 2008. **33**: p. 304-317.
12. Bazzi, K., *Nanostrucured Lithium Iron Phosphate As Cathode Material For Lithium Ion-Batteries*. 2014, Wayne State University: Detroit, Michigan, United States. p. 160.
13. Srivastava, R., *Synthesis and Characterization Techniques of Nanomaterials.* International Journal of Green Nanotechnology, 2012. **4**(1): p. 17-27.
14. Sharma, R., D. Bisen, U. Shukla, and B. Sharma, *X-ray diffraction: A powerful method of characterizing nanomaterials.* Recent Research in Science and Technology, 2012. **4**(8): p. 77-79.
15. Paravasthu, R., *Synthesis and characterization of lithium-ion cathode materials in the system (1-xy)$LiNi_{1/3}Mn_{1/3}Co_{1/3}O_2\cdot$ $xLi_2MnO_3\cdot$ $yLiCoO_2$*. 2012, Colorado State University. Libraries: Fort Collins, Colorado. p. 82.
16. Jauncey, G., *The scattering of X-rays and Bragg's law*. Proceedings of the National Academy of Sciences, 1924. **10**(2): p. 57-60.
17. Patterson, A., *The Scherrer formula for X-ray particle size determination.* Physical review, 1939. **56**(10): p. 978.
18. Ismail, A.A., F.R. van de Voort, and J. Sedman, *Fourier transform infrared spectroscopy: Principles and Applications.* Techniques and instrumentation in analytical chemistry, 1997. **18**: p. 93-139.
19. *Introduction to fourier transform infrared spectrometry*, in *Thermo Nicolet Corporation*. 2001: Madison 53711-4495, United States of America.
20. Pavia, D.L., G.M. Lampman, G.S. Kriz, and J.A. Vyvyan, *Introduction to spectroscopy*. 4th ed. 2008, Belmont, United States of America: Books/Cole, Cengage Learning. 656.
21. *Introduction to Raman Spectroscopy*, T.E.S.I. Corp, Editor. 2013: Madison, WI United States of America.
22. Zhong, C., *Development of new electrode materials for lithium ion batteries*. 2010, University of Wollongong: University of Wollongong Library, Australia. p. 109.
23. Prime, R.B., H.E. Bair, S. Vyazovkin, P.K. Gallagher, and A. Riga, *Thermogravimetric analysis (TGA).* Thermal analysis of polymers: Fundamentals and applications, 2009: p. 241-317.

24. Li, T., A.J. Senesi, and B. Lee, *Small angle X-ray scattering for nanoparticle research.* Chemical reviews, 2016. **116**(18): p. 11128-11180.
25. *The compact solution for nanostructure analysis*. 2017, Anton Paar GmbH, Austria: Austria, Europe.
26. Schnablegger, H. and Y. Singh, *The SAXS guide: Getting acquainted with the principles*. 3rd ed. 2011, A-8054 Graz, Austria: Austria: Anton Paar GmbH. 122.
27. *SAXS analysis in structural bbiology*. 2017, Anton Paar GmbH, Austria: Austria, Europe.
28. Zanello, P., *Inorganic Electrochemistry. Theory, Practice and Application. By Piero Zanello*. 2003, Cambridge, United Kingdom: The Royal Society of Chemistry. 615.
29. Mabbott, G.A., *An introduction to cyclic voltammetry.* Journal of Chemical Education, 1983. **60**(9): p. 697-702.
30. *Basic overview of the working principle of a potentiostat/galvanostat (PGSTAT)– Electrochemical cell setup.* Metrohm Autolab. BV, 2011: p. 1-3.
31. Monk, P.M., *Fundamentals of electro-analytical chemistry*, ed. A.T.i.t.S. (AnTs). 2001, The Antrium, Southern Gate, Chichester, West Sussex PO19 8SQ, England: John Wiley & Sons. 361.
32. Randviir, E.P. and C.E. Banks, *Electrochemical impedance spectroscopy: an overview of bioanalytical applications.* Analytical Methods, 2013. **5**(5): p. 1098-1115.
33. Girault, H.H., *Analytical and physical electrochemistry*. 2004, Centre Midi, CH-1015 Lausanne, Switzerland: EPFL Press. 423.
34. Bard, A.J., L.R. Faulkner, J. Leddy, and C.G. Zoski, *Electrochemical methods: fundamentals and applications*. Vol. 2. 2001, 605 Third Avenue, New York: John Wiley & Sons, Inc. 833.
35. *Basics of Electrochemical Impedance Spectroscopy*. Application Note AC-1; Available from: https://www.researchgate.net/profile/K_Koteshwara_Reddy/post/electrochemical_impedance_spectroscopy_EIS_and_how_to_fit_the_results_with_equivalent_circuit_EC/attachment/59d62e4179197b807798c773/AS:353521699442688@1461297549908/download/App_Note_AC-1.pdf.

CHAPTER 3

Chapter Overview

This chapter discusses the results obtained from the various microscopic (HRTEM and HRSEM), spectroscopic (FTIR, XRD and EDS), thermogravimetric (TG) and electrochemical (CV, EIS) techniques used to characterise the prepared pristine cathodes, graphene oxide, graphene and hybrid cathodes.

3. Results and Discussion

3.1. Analysis of Pristine $LiFePO_4$ and Li_2MnSiO_4 Cathode Materials

3.1.1. High Resolution Scanning Electron Microscopy

The morphological features of the prepared pristine $LiFePO_4$ (LFP) and Li_2MnSiO_4 (LMS) cathode materials were studied using HRSEM as shown in Fig. 11. Both pristine materials show slightly agglomerated spherical nanoparticles having uniform sizes. These morphologies could affect the electrochemical behaviour of the materials as they are most likely to cause slow intercalation/de-intercalation of Li-ions during charge/discharge processes [1].

The EDS data of these materials is summarised in Table 2. The presence of lithium could not be confirmed because of its low atomic mass which cannot be detected by the instrument [1]. Other elements (such as O, P and Fe for LFP and O, Si and Mn for LMS) were detected from these materials. Trace sulphur elements were detected in LMS which could have been due to impurities from precursors. Pure $LiFePO_4$ was obtained without any impurities from precursors or cross contamination.

Table 2: Elemental mapping of LFP and LMS using HRSEM

LFP		LMS	
Element	Weight %	Element	Weight %
O	41.86	O	46.89
P	22.08	Si	14.92
Fe	36.06	S	0.77
		Mn	37.42
Total	100	Total	100

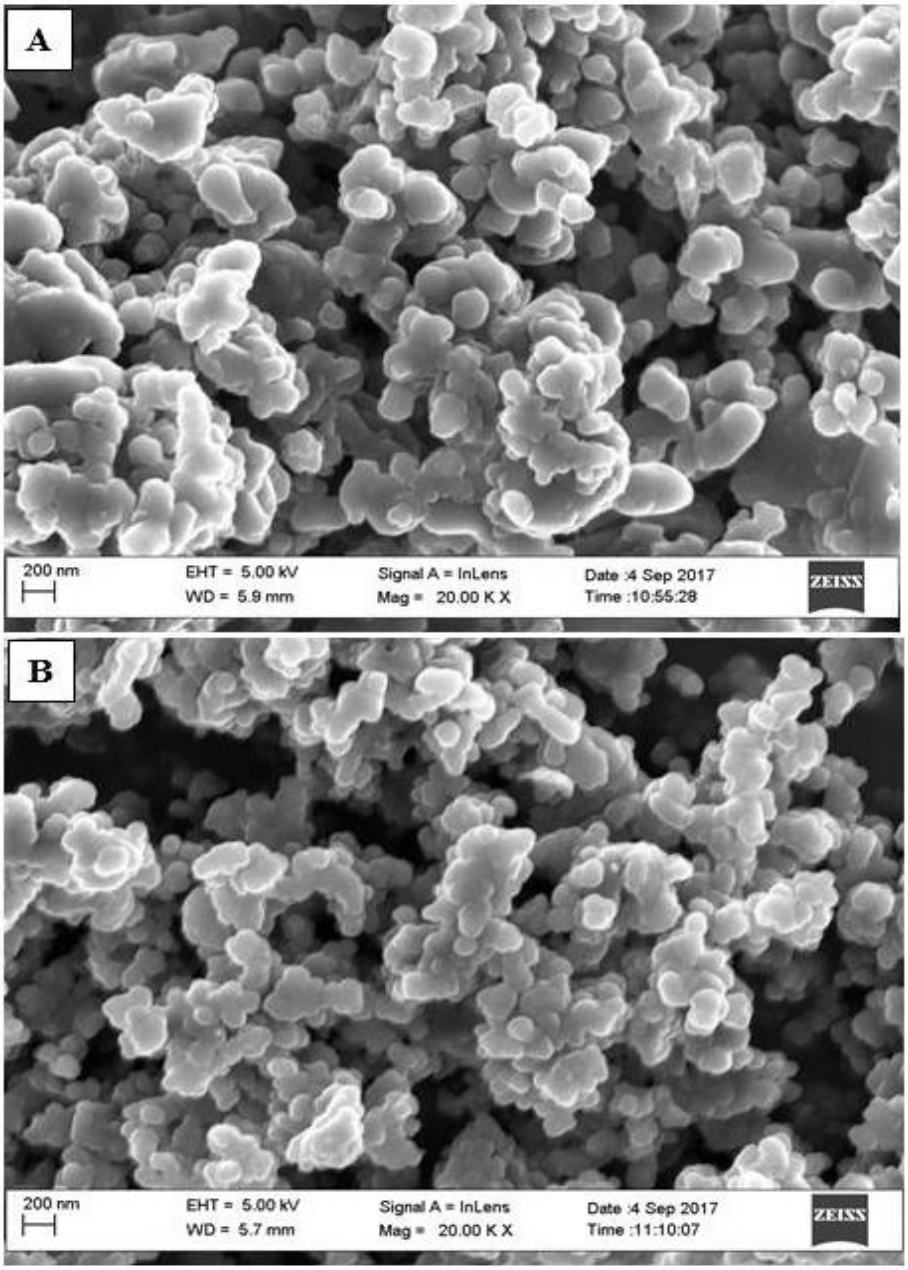

Figure 11: High resolution scanning electron microscopy images of (A) $LiFePO_4$ and (B) Li_2MnSiO_4 nanoparticles with a magnification = 20.00 K X

3.1.2. High Resolution Transmission Electron Microscopy

High resolution electron microscopy (HRTEM) is a powerful analytical technique used to study the morphology and microstructural features of nanomaterials. Figure 12 shows HRTEM images of the pristine materials at different scale views of 20 and 2 ηm for thorough

interrogation of the morphology and internal structures of these materials. The HRTEM image of LFP (Fig. 12 A) shows spherical nanoparticles that are slightly agglomerated and this is consistent with the results obtained from HRSEM. The nanoparticles have an average particle size of 35 ηm. Figure 12 C shows tiny spherical and highly agglomerated LMS nanoparticles. These nanoparticles have an average particle size of 5 ηm. However, they coalesce to form larger spherical nanoparticles having an average size of 40 ηm as show in Fig. 12. C (inset).

The presence of lattice fringes observed at low scale view (Fig. 12 B and D) is a clear indication that the nanoparticles are polycrystalline. This is further confirmed by the weak diffraction spots in the selected area electron diffraction (SAED) patterns making up concentric rings in the corresponding inset images [2]. Figure 13 shows elemental mapping of these materials and confirmed the presence of Fe, P and O in LFP and Mn, Si and O in LMS, with Cu and Ni impurities coming from the grid.

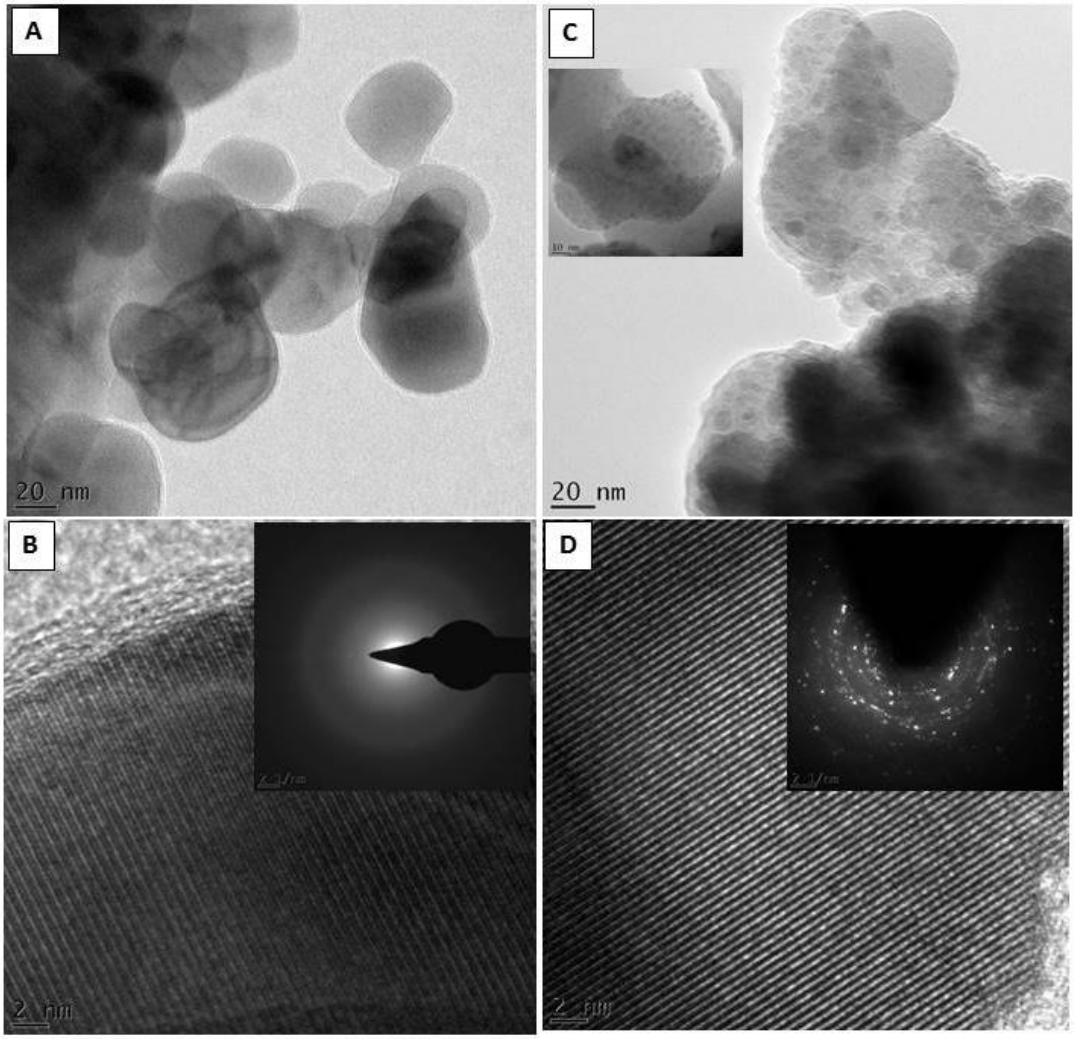

Figure 12: HRTEM images (A) and (B) for $LiFePO_4$ (at 20 and 2 ηm) and (C) and (D) for Li_2MnSiO_4 (same scale as in $LiFePO_4$). Inset: corresponding SAED pattern of (B) $LiFePO_4$ and (D) Li_2MnSiO_4

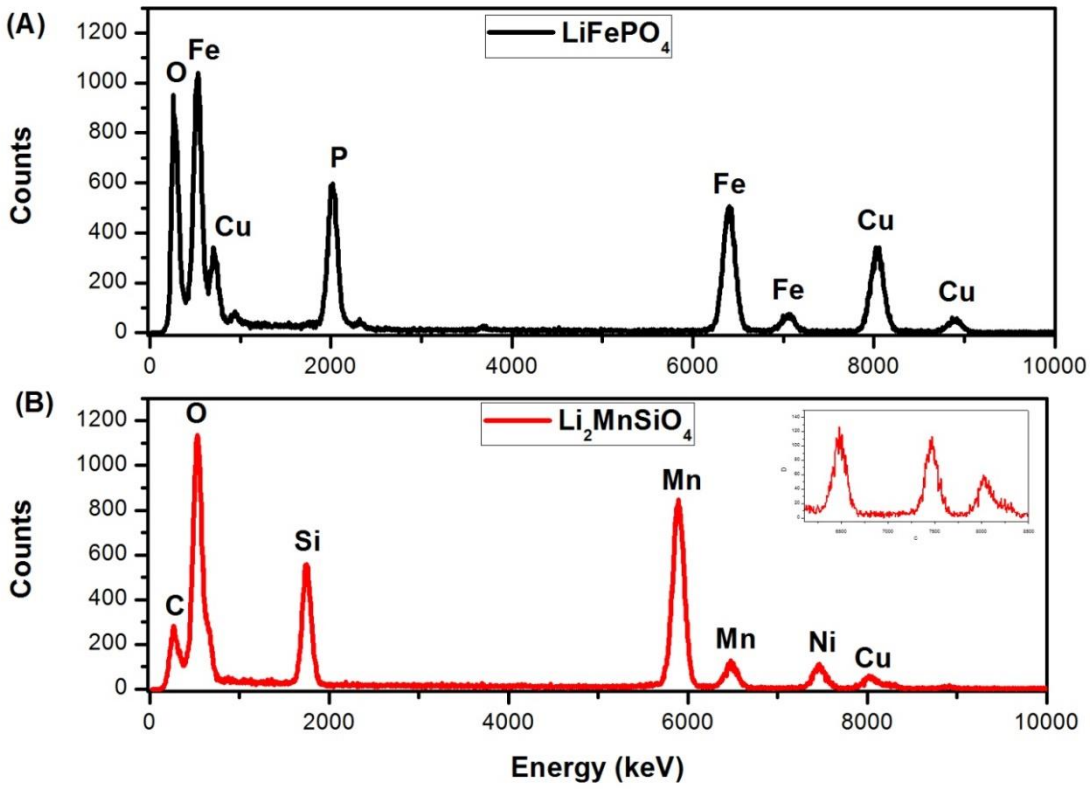

Figure 13: EDS spectra of (A) $LiFePO_4$ and (B) Li_2MnSiO_4

3.1.3. Small-Angle X-ray Scattering (SAXS) Analysis

SAXS was used to further study the morphology of the pristine cathode materials as shown by the pair-distance distribution function (PDDF) and particle size distribution curves in Fig. 14. The advantage of using SAXS is that the nanomaterials are analysed in their natural environment, therefore giving accurate results about their properties. According to the particle size distribution curve by the number of particles (SD_N), the pristine LFP is composed of nanoparticles with different sizes of 5, 14 and 25 ηm. Similarly, the pristine LMS material has nanoparticles of different sizes of 5, 12, 22, 28 and 35 ηm. These findings are an indication that the synthesized cathode materials have a distribution of small and bigger particles. The presence of small nanoparticles will provide reduced diffusion lengths therefore fast electron and Li-ion transport kinetics during the charge/di-charge processes [3].

The shape of the PDDF curve in Fig. 14 (inset) was used to get more information about the morphology of the nanomaterials [4]. The materials have a flat disc-like shape with diameters of 20 and 25 ηm for LFP and LMS, respectively. These findings are in contrast with those obtained from HRTEM. HRTEM images are only limited to a small region of the sample which is not ideal for making conclusions about the entire sample. However, in SAXS the samples are analysed in their natural environment and the obtained results are representative of the entire sample [5].

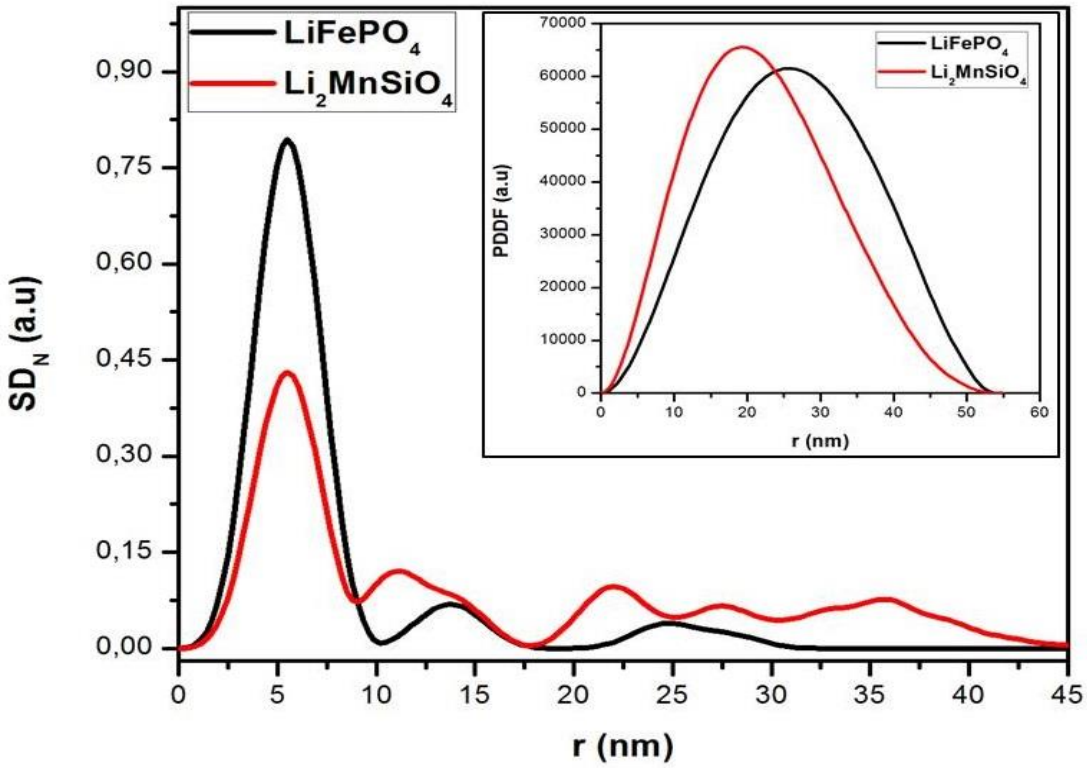

Figure 14: SAXS analysis: particle size distribution curve (by number of particles) for LFP and LMS, and corresponding PDDF curves (inset)

3.1.4. Fourier Transform Infrared (FTIR) Spectroscopy

FTIR spectroscopy is a useful analytical tool used for identification of functional groups found on the surface of nanomaterials [6]. The lower region of the spectrum (bellow 1500 cm^{-1}) is used to confirm the presence of bonds formed by inorganic molecules [7]. For this

reason, the FTIR spectra of the prepared pristine LFP and LMS cathode materials was only focused between 400 and 1400 cm^{-1} as it is shown in Fig. 15.

The FTIR spectrum of LFP (Fig. 15 A) shows two broad characteristic absorption bands. The first absorption band in the upper region of the spectrum, from 930 to 1220 cm^{-1} is assigned to the intermolecular stretching vibration modes of $[PO_4]^{3-}$ group [7, 8]. The second band in the lower region of the spectrum (550 to 660 cm^{-1}) is assigned to the intermolecular bending vibrations of $[PO_4]^{3-}$ group [7, 8]. There is also a set of two small absorption bands appearing at 457 and 502 cm^{-1} which can be attributed to the Li-ion motion [7]. Finally, the vibrational band observed at 430 cm^{-1} suggests that the pristine LFP contains traces of Li_3PO_4 impurity which is also confirmed by the X-ray diffraction patterns of the material.

Figure 15 B shows the FTIR spectrum of LMS also in the same region as LFP. The material is characterised by a series of absorption bands at 948, 884, 612 and 520 cm^{-1}, which can be attributed to the frame work of $[SiO_4]$ unit in LMS cathode material [9]. These bands are further divided into four different modes of $[SiO_4]$ denoted with *v* and numbers from one to four. The absorption band at 948 cm^{-1} is assigned to the v_3 mode. The v_1 and v_4 modes are assigned to the bands at 884 and 520 cm^{-1}, and 612 cm^{-1}, respectively [10]. In addition, the v_1 and v_3 modes represent the symmetric and asymmetric stretching mode of the Si-O bonds whereas the v_4 mode involves the symmetric and asymmetric bending vibrations of O-Si-O in $[SiO_4]$ unit [11]. The low frequency absorption band at 435 cm^{-1} is attributed to the Li-ion motion of this material [9, 10]. The material contained an impurity phase of the $[SiO_3]$ unit of Li_2SiO_3 which is assigned to the two bands appearing at 739 and 1067 cm^{-1} [9, 12].

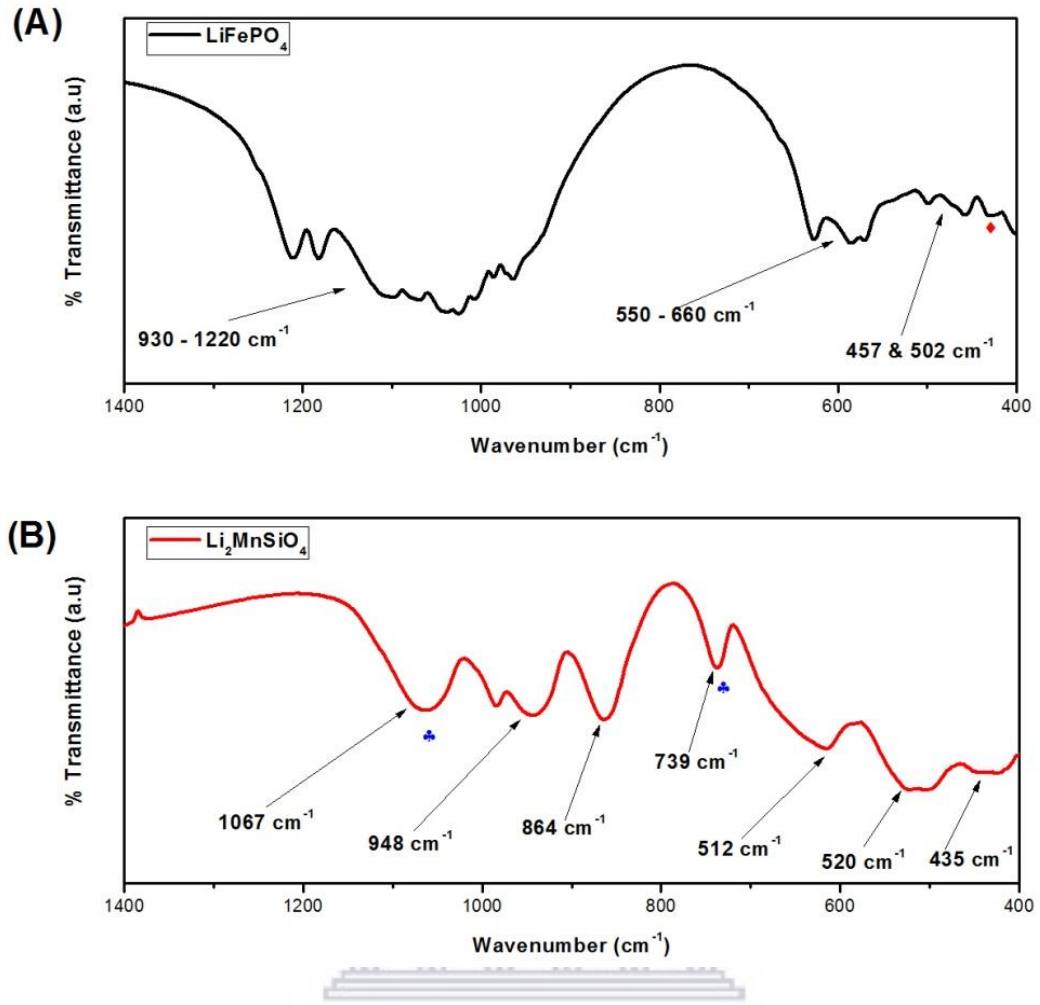

Figure 15: FTIR spectra of pristine (A) LFP and (B) LMS cathode materials in the frequency range between 400 and 1400 cm^{-1}

3.1.5. X-ray Diffraction

The crystal structure of pristine LFP and LMS cathode materials was identified using XRD. As illustrated in Fig. 16 A, the X-ray diffraction patterns of LFP were indexed to the orthorhombic olivine-type structure with *Pmna* space group [13]. In addition, the diffraction peaks are quite narrow and this is an indication of a well-crystallized phase observed with this material. However, sample contained impurities (FeP, Fe_2P and Li_3PO_4) suggesting that not all the Fe^{3+} were successfully reduced to F^{2+} during the preparation of this cathode material [14]. These findings are in agreement with those obtained from FTIR spectrum of this material (Fig. 15, Section 3.1.4). Gao and co-authors [15] also obtained the same impurities from their studies and suggested that they can be avoided by incorporating a

chelating agent, in their case gelatin. Other authors [16, 17] suggest that the preparation of this material in the presence of carbon source inhibits the formation of impurities. The obtained lattice parameters for the material are listed in Table 3**.** These results are comparable with those obtained by Tian and co-authors [18].

The X-ray diffraction patterns of LMS (Fig. 16 B) were indexed to the orthorhombic unit cell of $Pmn2_1$ group with a few impurity phases of MnO and Li_2SiO_3 [19-21]. The formation of these impurities is illustrated by Equation (12) [22-24]:

$$Li_2MnSiO_4 \rightarrow Li_2SO_3 + MnO \qquad (12)$$

The presence of these impurities in LMS is undesirable, but they are electrochemically inactive [21]. The lattice parameters of LMS are listed in Table 3 and are closely related to those obtained by Arroyo-deDompablo [25] and Hwang [26].

Table 3: The lattice parameters for pristine LFP and LMS cathode materials

Sample	*a* (Å)	*b* (Å)	*c* (Å)
$LiFePO_4$	8.566	12.053	8.596
Li_2MnSiO_4	9.392	5.397	4.660

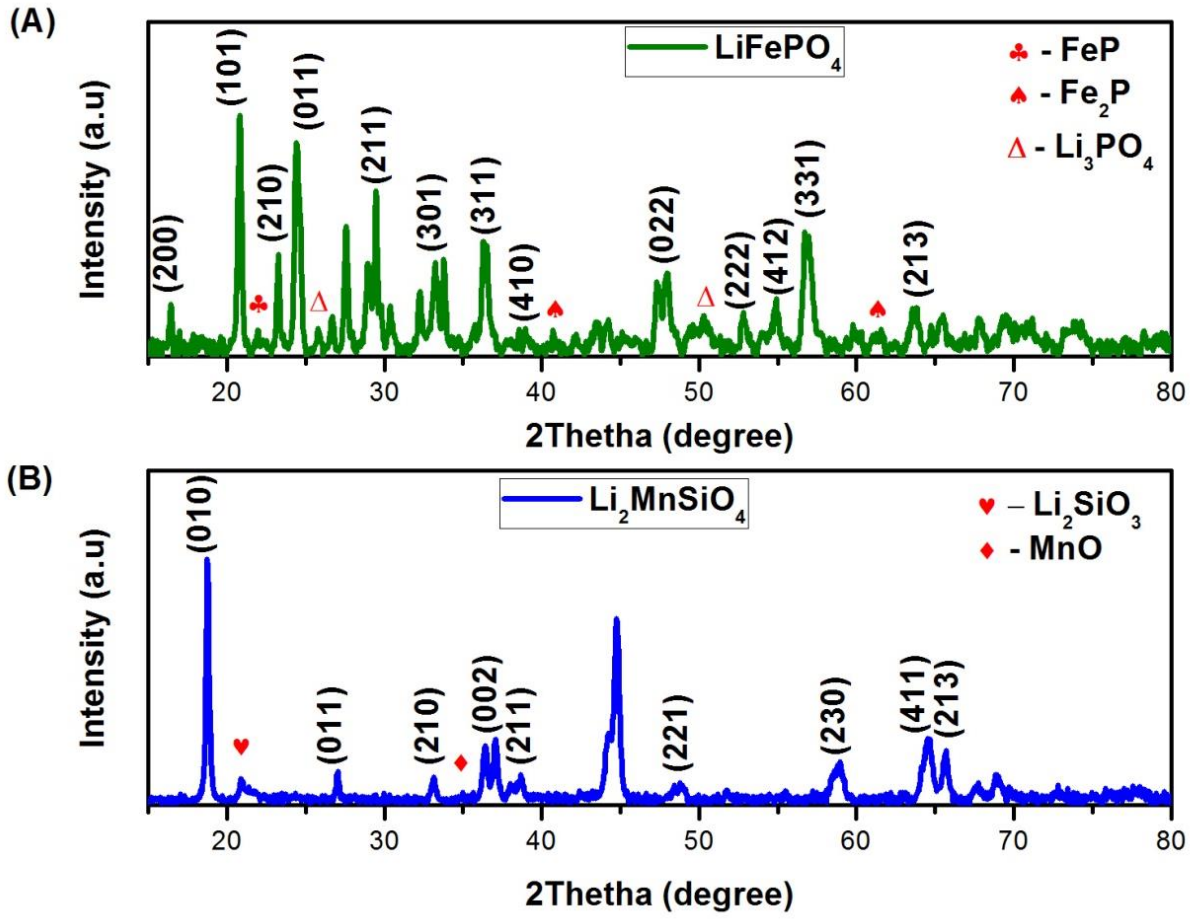

Figure 16: X-ray diffraction patterns of (A) LFP and (B) LMS cathode materials in the 2Θ range between 15 and 80 °

3.1.6. Thermogravimetric (TG) Analysis

The thermal stability of pristine LFP and LMS cathode materials was studied by TG analysis from room temperature to 900 ºC with a heating rate of 20 ºC min^{-1} and the obtained results are shown in Fig. 17. There is no significant weight loss in the LFP powder which confirms the stability of the material in this temperature range. The observed 8 % weight loss can attributed to the crystallization of the material [15]. The TG curve for LMS powder showed a single weight loss process at 710 to 790 ºC which can be attributed to oxidation or crystallization of the material. During this test this material lost 18 % of its weight. The results clearly show that LFP has better thermal stabilities than LMS which is associated with the presence of the strong covalent bond between P-O in the $[PO_4]^n$ unit [27, 28].

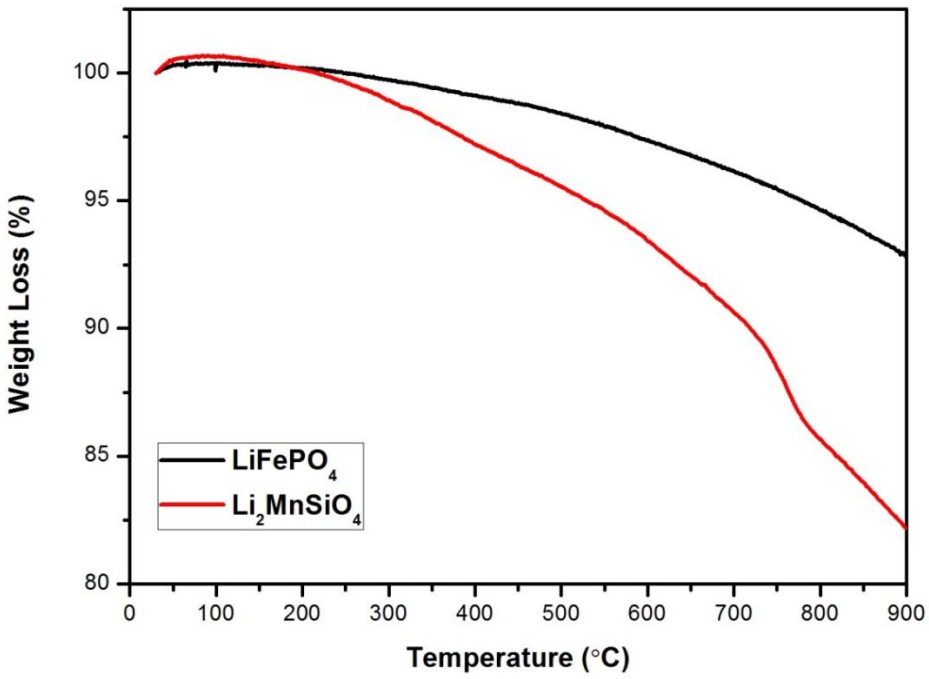

Figure 17: TG curves of the prepared pristine $LiFePO_4$ and Li_2MnSiO_4 cathode materials using a temperature programme with a heating rate of 20 ºC min^{-1} from room temperature to 900 ºC

3.1.7. Electrochemical Characterization

3.1.7.1. Cyclic Voltammetry (CV)

The redox activity of the prepared pristine LFP cathode materials was investigated using CV in 1.0 M $LiClO_4$ electrolyte. Figure 18 shows cyclic voltammograms for bare GCE and GCE electrode modified with LFP in the potential range from -1000 to 0.0 mV, at a scan rate of 05 mV s^{-1}. There is no redox activity observed for the bare GCE because there is no active material on its surface. However, the GCE modified with LFP showed only a reduction peak without its oxidation pair. The absence of the oxidation peak is associated with the used electrolyte, because this peak is observed in other electrolytes such as 1 M $LiPF_6$ in a 1:1 mixture of ethylene carbonate (EC) and dimethyl carbonate (DMC) [18]. The reduction peak is characterised by a peak potential of - 725 mV (-1.45 μA) corresponding to Fe^{3+}/F^{2+} as indicated by the reaction below:

Reduction:

$$Li^{+} + e^{-} + FePO_4 \rightarrow LiFePO_4 \qquad (13)$$

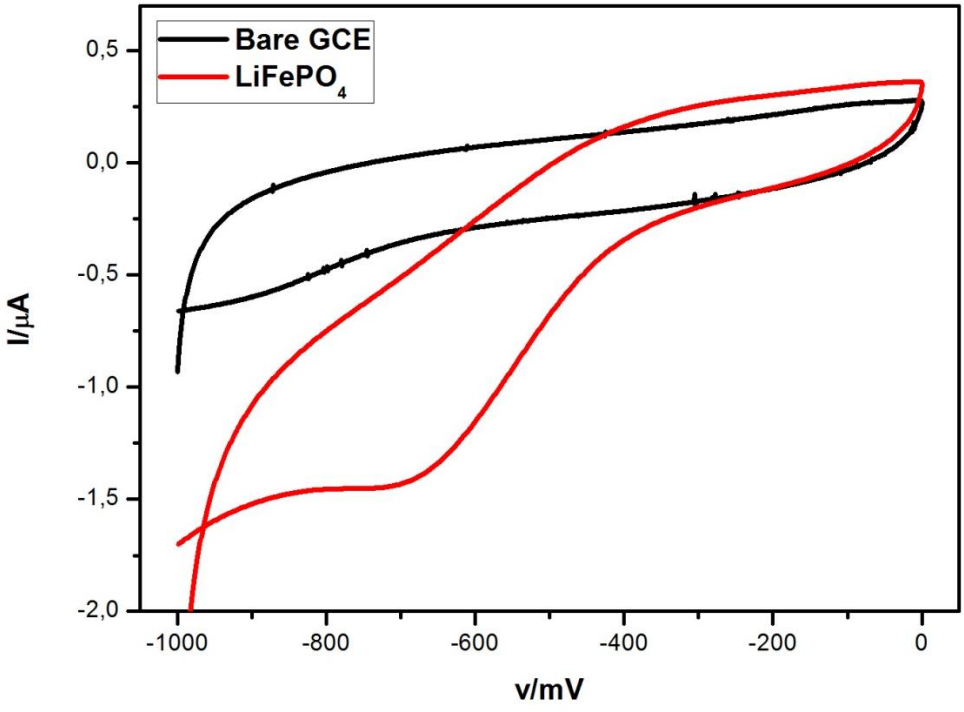

Figure 18: Cyclic voltammograms of bare GCE and GCE modified with pristine LFP cathode material in 1.0 M $LiClO_4$ at a scan rate of 05 mV s^{-1}

The pristine LFP material shows an irreversible electrochemistry, characterized by the presence of the reduction peak without its oxidation pair. The specific capacity of the material was calculated by integrating the area of the reduction peak using Origin software [29-31]. The calculation steps were as follows:

Integrated area= 7.3429×10^{-7} A V

Active mass = 2.2×10^{-5} g

$$\text{Specific Capacity (mA h g}^{-1}) = \frac{\text{Charge}}{\text{Active mass of the electrode material}} \quad (14)$$

$$\text{Charge } (Q) = \frac{\text{Integrated area}}{\text{Scan rate}} \quad (15)$$

$$= \frac{7.3429 \times 10^{-7}\ \text{A V}}{0.005\ \text{V s}^{-1}}$$

$$= 1.4686 \times 10^{-4}\ \text{A s}$$

$$\therefore \text{ Specific Capacity} = \frac{1.4686 \times 10^{-4}\ \text{A s}}{2.2 \times 10^{-5}\ \text{g}}$$

$$= 6.675\ \text{A s g}^{-1}$$

However, the capacity of a battery is expressed in mA h g^{-1} and we know that 3600 A s = 1 A h, and 1 g = 1000 mg.

$$\therefore \text{ Specific Capacity} = 6.675\ \text{A s g}^{-1} \times \left(\frac{1000\ \text{g}}{3600\ \text{A s}}\right) \text{mA h g}^{-1}$$

$$= 1.85\ \text{mA h g}^{-1}$$

Figure 19 shows the electrochemical cycling behaviour of pristine LFP cathode material at different scan rates, from 01 – 09 mV s^{-1}.

It can be observed that there is a linear relationship between scan rate and peak current. In addition, an increase in scan rate triggers a small shift in the reduction peak potential towards more negative potential values.

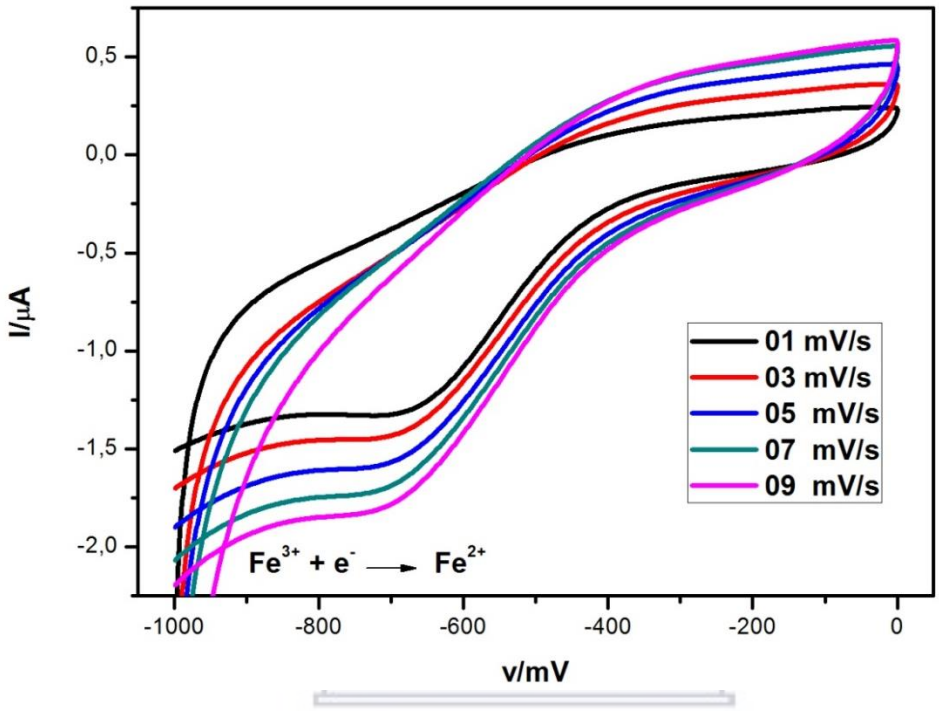

Figure 19: The effect of scan rate on the cyclic voltammogramms of pristine LFP cathode material in 1.0 M $LiClO_4$, in the potential range between -1000 – 0 mV

Figure 20 shows cyclic voltammograms of bare GCE and GCE modified with LMS recorded at a scan rate of 05 mV s^{-1}, in 1.0 M $LiClO_4$ electrolyte. The bare GCE does not show any electrochemistry (no peaks in the CV curves) because there is nothing coated on the electrode surface. However, the appearance of redox peaks signified that the electrode modified with LMS is electrochemically active. These redox peaks are characterised by the peak potentials at 340 mV and 114 mV corresponding to the oxidation (Mn^{2+}/Mn^{3+}) and reduction (Mn^{3+}/Mn^{2+}) of Mn in LMS, respectively. The redox reactions are illustrated by Equations 16 and 17 below:

Oxidation:

$$Li_2MnSiO_4 \rightarrow LiMnSiO_4 + Li^+ + e^- \quad (16)$$

Reduction:

$$LiMnSiO_4 + Li^+ + e^- \rightarrow Li_2MnSiO_4 \quad (17)$$

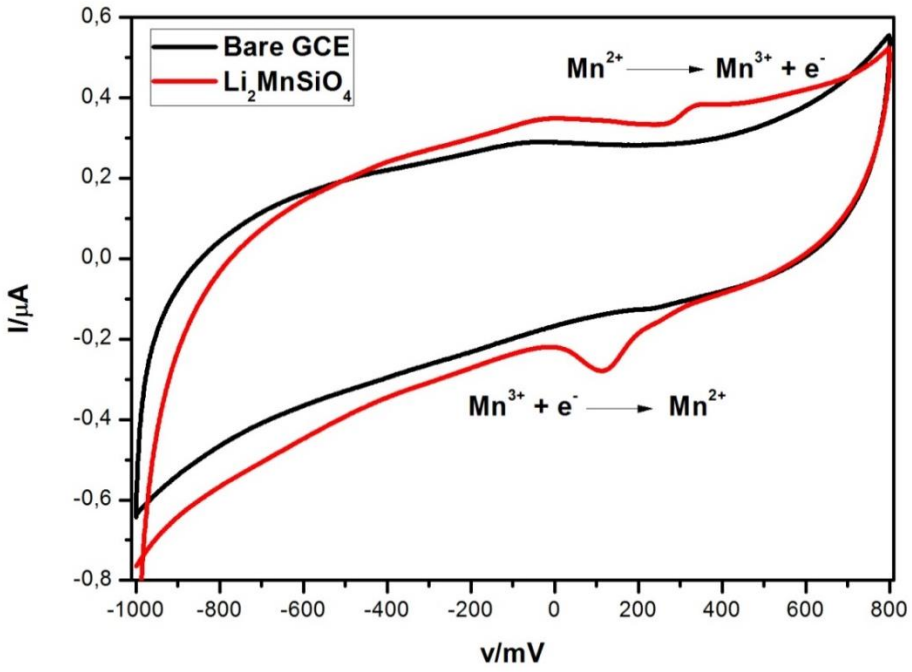

Figure 20: Cyclic voltammograms of bare GCE and GCE modified with LMS in 1.0 M $LiClO_4$ in the potential range from -1000 to 800 mV, at a scan rate of 05 mV s^{-1}

The peak separation and the current ratio I_{pa}/I_{pc} were calculated to diagnose the reversibility of the redox reaction for this material as show by the calculation bellow:

$$E^{o} = \frac{E_{pa} + E_{pc}}{2} \quad (18)$$

$$= \frac{340\,\text{mV} + 114\,\text{mV}}{2}$$

$$= 227\ \text{mV}$$

$$\Delta E_p = E_{pa} + E_{pc}$$

$$= 340\ \text{mV} - 114\ \text{mV}$$

$$= 226\ \text{mV}$$

$$\frac{I_{pa}}{I_{pc}} = \frac{|0.39\ \mu\text{A}|}{|-0.28\ \mu\text{A}|} \quad (19)$$

$$= 1.39$$

There is a large separation between the anodic and the cathodic peak potentials characterised by the E^{o} value of 227 mV. The ΔE_p value of 226 mV is higher than 59 mV and the I_{pa}/I_{pc} ratio is 1.39, which suggests that the redox reactions of LMS are quasi-reversible. The specific capacity of pristine LMS was also calculated the same way as LFP as indicated below:

Integrated area = 3.906×10^{-7} A V

Active mass $= 2.0 \times 10^{-5}$ g

$$\text{Specific Capacity (mA h g}^{-1}) = \frac{\text{Charge}}{\text{Active mass of the electrode material}}$$

$$\text{Charge } (Q) = \frac{\text{Integrated area}}{\text{Scan rate}}$$

$$= \frac{3.906 \times 10^{-7}\ \text{A V}}{0.005\ \text{V s}^{-1}}$$

$$= 7.812 \times 10^{-5}\ \text{A s}$$

$$\therefore \text{ Specific Capacity} = \frac{7.812 \times 10^{-5}\ \text{A s}}{2.0 \times 10^{-5}\ \text{g}}$$

$$= 3.906\ \text{A s g}^{-1}$$

$$\therefore \text{ Specific Capacity} = 3.906\ \text{A s g}^{-1} \times \left(\frac{1000\ \text{g}}{3600\ \text{A s}}\right) \text{mA h g}^{-1}$$

$$= 1.09\ \text{mA h g}^{-1}$$

The calculated specific capacities of 1.85 and 1.09 mA h g^{-1} for LFP and LMS, respectively are lower than their theoretical values of 170 and 330 mA h g^{-1}. However, these values are expected to be higher for the hybrid cathode material.

Table 4: Redox parameters for pristine LFP and LMS cathode materials obtained from CV

Electrode material	E_{pa} (mV)	I_{pa} (μA)	E_{pc} (mV)	I_{pc} (μA)	ΔE_p (mV)	E^o (mV)	I_{pa}/I_{pc}
LFP	-	-	725	-1.45	-	-	-
LMS	340	0.39	114	-0.28			1.39

The electrochemical cycling behaviour of the pristine LMS cathode material was studied using cyclic voltammograms at different scan rates as shown in Fig. 21. There is a linear relationship observed between the scan rates and peak currents of the material. An increase in scan rate results to an increase in the peak current. There are no significant changes/shifts in the peak potentials for both anodic and cathodic peaks. The difference between the peak potentials, ΔE_p was calculated to be 218 mV and this value is larger than 59 mV which is an ideal Nernstian process. This is attributed to kinetic limitations that occur during electrochemical processes of the material.

Furthermore, the intensity of the peak currents was used to calculate the ratio of peak currents (I_{pa}/I_{pc}) to further diagnose the reversibility of the LMS system. The calculated I_{pa}/I_{pc} = 1.29, thus higher than the ideal value of 1 observed for reversible systems. Therefore, the LMS cathode material follows a quasi-reversible behaviour which is supported by higher values of ΔE_p (218 mV) and I_{pa}/I_{pc} (1.29) compared to those of an ideal reversible behaviour.

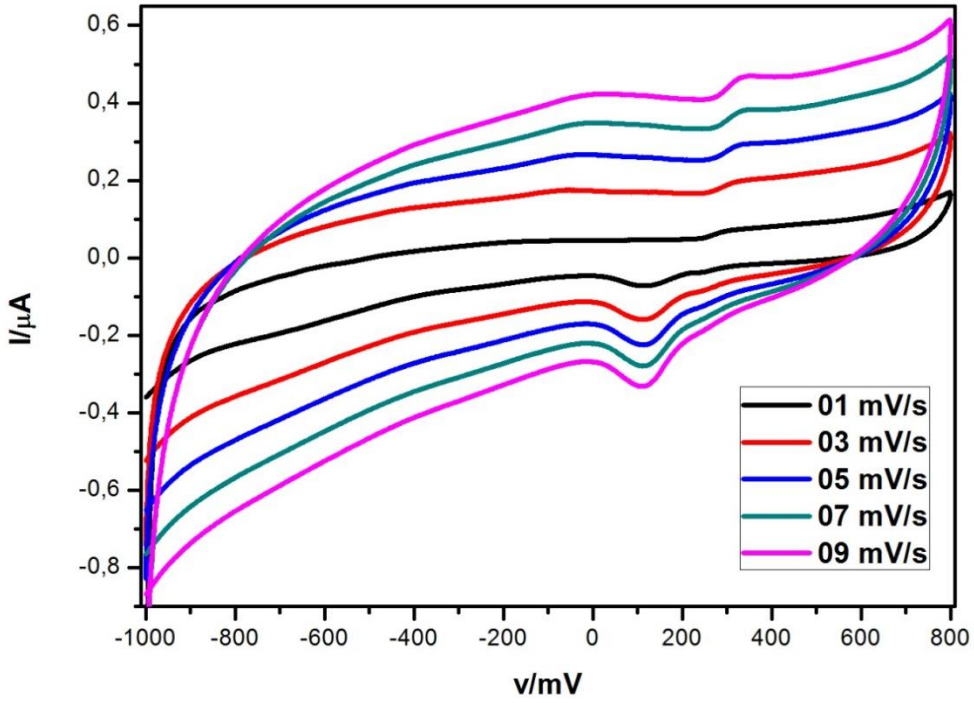

Figure 21: The effect of scan rate on the cyclic voltammogramms of pristine LMS cathode material in 1.0 M $LiClO_4$, in the potential range between -1000 – 800 mV

3.1.7.2. Electrochemical Impedance Spectroscopy (EIS)

EIS studies were carried out to further interrogate the electrochemistry of the synthesised pristine cathode materials, as shown by the Nyquist and Bode plots in Fig. 22 and 23, respectively. The Nyquist plots for both pristine materials only showed an inclined line without a semi-circle as shown by Fig. 22 A (inset). This is an indication that these materials have a capacitive behaviour [32]. The obtained Nyquist plots were simulated using Zview software according to the modified Randles equivalent circuit as shown by Fig. 22 B. In this model, R_s was the solution resistance, C - the capacitor, R_{ct} - the charge transfer resistance and W_s - the Warburg diffusion. The obtained values for these parameters were tabulated in Table 5. The LFP exhibited a smaller (4.68 Ω) R_s value compared to LMS (17.85 Ω). However, its R_{ct} value (2813 Ω) is higher than that of LMS (2008 Ω) which shows a slow transfer of electrons at the surface of the electrode. Furthermore, the capacitance and Warburg diffusion are almost the same for both materials. However, pristine LMS material

has a slightly higher capacitance (7.41 x 10^{-6} F) and Warburg diffusion (1.75 x 10^{5} $\Omega s^{-1/2}$) which is an indication of a more capacitive behaviour of the material compared to LFP.

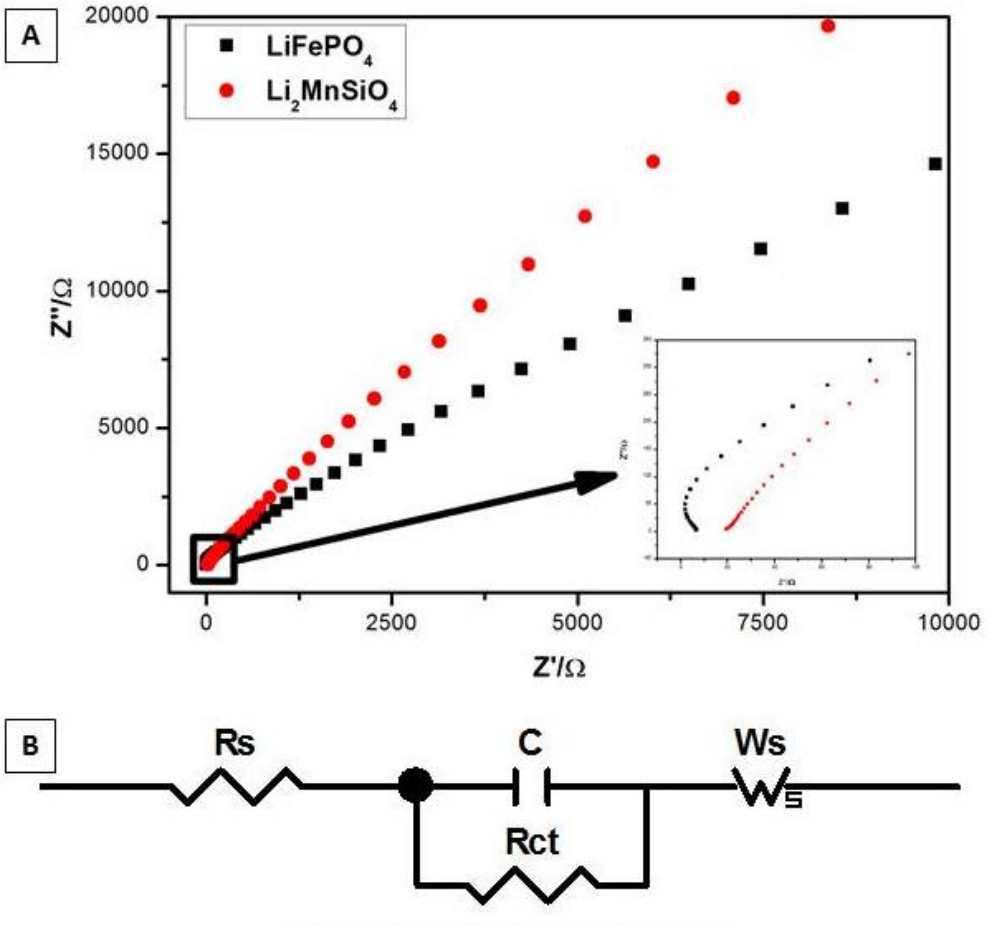

Figure 22: (A) Nyquist plot and (B) equivalent circuit used for fitting the EIS data for the pristine cathode materials

The Bode plots (Fig. 23) further describes the electrochemistry of these materials. The impedance and phase angle values generated at low frequency region from these plots suggests that the pristine LFP material (4.39 Ω and 87.8 º) has better conductivity and fast kinetics than LMS (4.27 Ω and 74.3 º). Therefore, the low impedance observed for LFP signifies that the material has a greater electron flow as opposed to LMS and this in good agreement with the Nyquist plot results.

Table 5: Fitted parameters for the pristine LFP and LMS cathode materials

Material	R_s/Ω	C/F	R_{ct}/Ω	$W_s/\Omega\ s^{-1/2}$
LFP	4.68	1.17×10^{-6}	2813	1.65×10^{5}
LMS	17.85	7.41×10^{-6}	2008	1.75×10^{5}

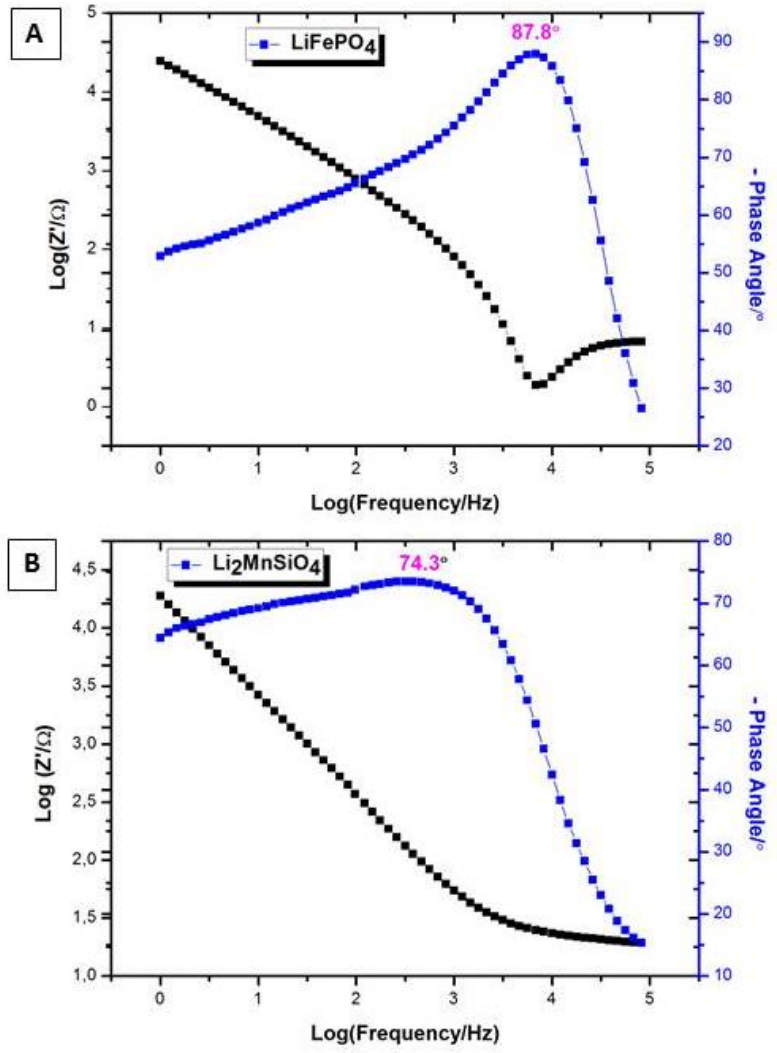

Figure 23: Bode plots for pristine (A) LFP and (B) LMS cathode materials

The diffusion of Li-ions is of particular interest in electrochemical studies of Li-ion battery materials because it is a rate determining step. The Warburg domain at low frequency region of the Nyquist plot were used to determine the kinetics for the rate determining step by calculating the diffusion coefficient form the following Equation [31].

$$Z' = R_s + R_{ct} + \sigma\omega^{-1/2} \quad (20)$$

where Z' is the real impedance, σ is the Warburg coefficient, ω is the angular frequency and the other parameters have their usual meaning. A plot of Z' vs $\omega^{-1/2}$ was generated from Equation (20) which gave a slope = σ and intercept = (R_s + R_{ct}) as shown in Fig. 24 for both pristine materials. The obtained values of σ were 73526.28 and 65908.11 Ω $s^{-1/2}$ corresponding to the pristine LFP and LMS cathode materials, respectively.

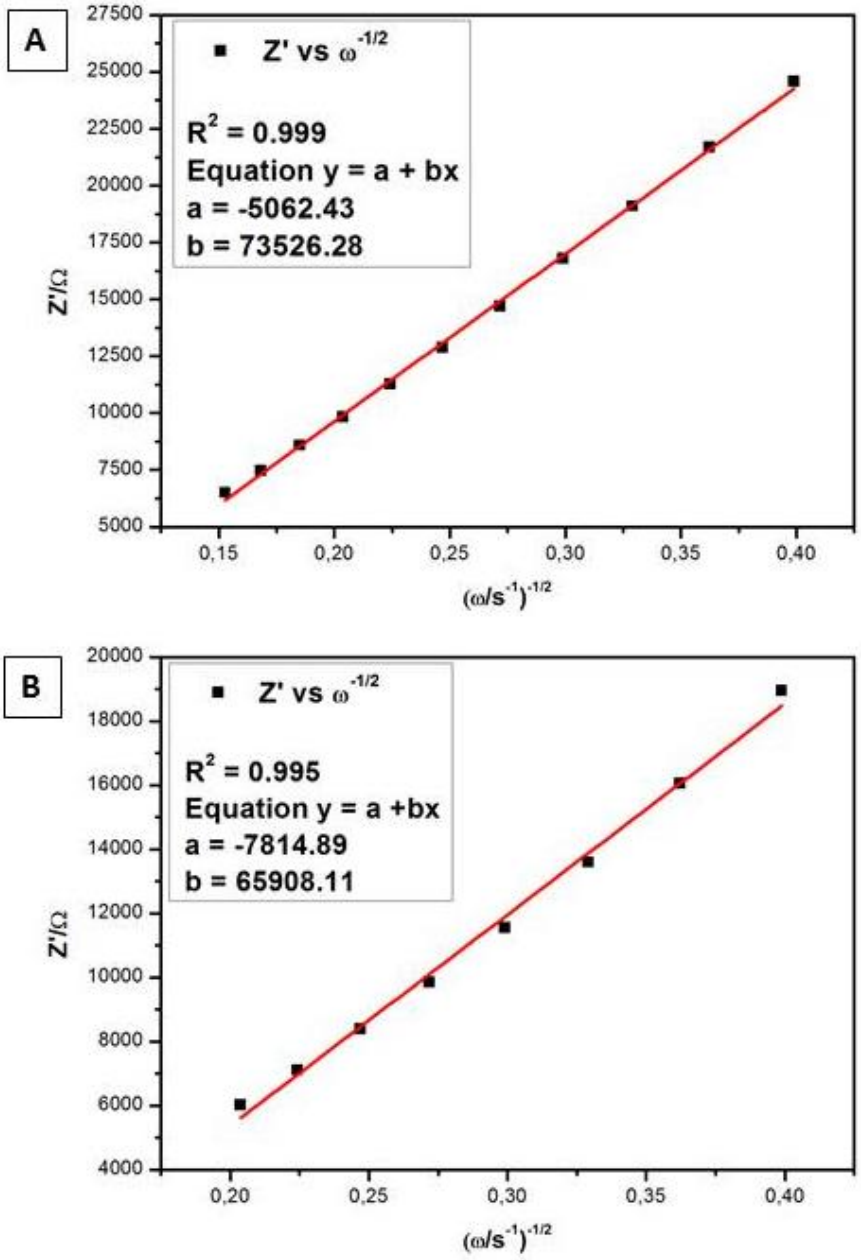

Figure 24: Z' vs $\omega^{-1/2}$ plots of (A) LFP and (B) LMS cathode materials

The diffusion coefficients were then calculated from the obtained σ values and other parameters using the following Equations [31]:

$$\sigma = \frac{RT}{\sqrt{2}n^2F^2A}\left(\frac{1}{D_o^{1/2}C_o} + \frac{1}{D_r^{1/2}C_r}\right) \qquad (21)$$

It can be assumed that $D_o = D_r = D_{app}$ and $C_o = C_r = C$ from Equation (21) which is further simplified to get D [31].

$$\sigma = \frac{RT}{\sqrt{2}n^2F^2A}\left(\frac{1}{D^{1/2}C} + \frac{1}{D^{1/2}C}\right) \tag{22}$$

$$D_{app} = \left(\frac{\sqrt{2}RT}{\sigma n^2F^2AC}\right)^2 \tag{23}$$

where R is the gas constant = 8.314 J mol^{-1}, T is the temperature = 298.15 K, n in the number of electrons transferred, F is the Faraday's constant = 96485 C mol^{-1}, A is the area of the GCE = 0.071 cm^2, C is the concentration of Li-ions = 3.486 x 10^{-5} and 6.215 x 10^{-5} mol cm^{-3} for LFP and LMS, respectively and the other parameters still have the same meanings. The calculated diffusion coefficients were 4.282 x 10^{-12} and 1.677 x 10^{-12} cm^2 s^{-1} for LFP and LMS, respectively. It can be observed that the pristine LFP cathode has a higher diffusion coefficient compared to LMS which is an indication of better kinetics exhibited by this material. Electrochemical studies have revealed that indeed the two pristine cathode materials complement each other's properties and are expected to produce a hybrid which offers better performances than these materials.

3.2. Analysis of Graphene Nanosheets

3.2.1. High Resolution Scanning Electron Microscopy

Morphological studies of graphene oxide and graphene nanosheets were performed using HRSEM and HRTEM as indicated by the images in Fig. 25 and 26, respectively. Figure 25 A shows that graphene oxide has many layers that are uniformly stacked on top of each other and resemble an accordion-like structure. The nanosheets had a few wrinkles on its edges and this made it easy to distinguish between the individual nanosheets. After reduction with $NaBH_4$ to form graphene, the number of layers was significantly reduced as it can be seen in Fig. 25 B. The reduced number of layers is evidence that the graphene oxide nanosheets were exfoliated by the reduction process to successfully form graphene nanosheets with wrinkles on its edges.

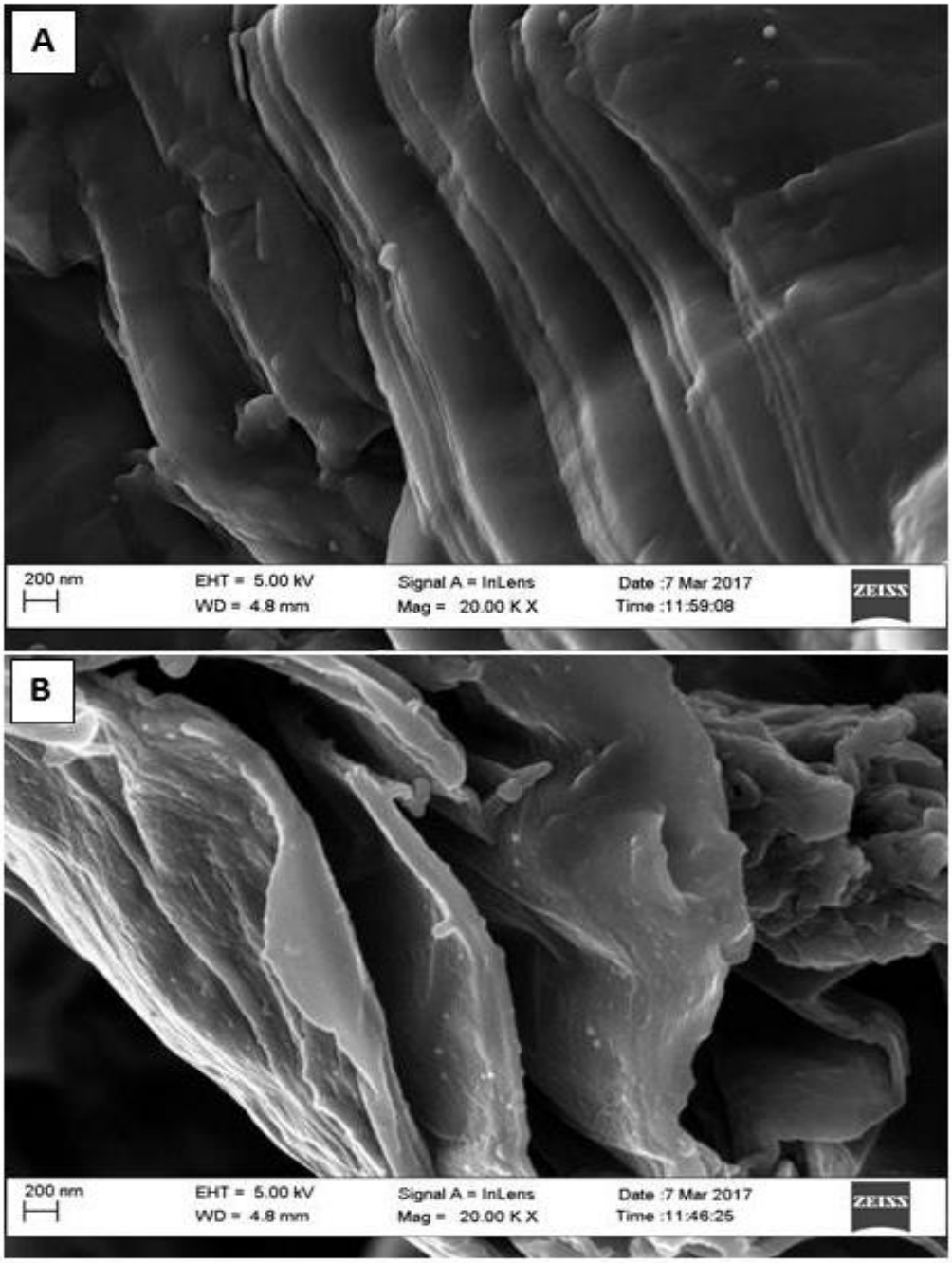

Figure 25: HRSEM images of (A) graphene oxide and (B) graphene

3.2.2. High Resolution Transmission Electron Microscopy

Figure 26 shows the HRTEM images of graphene oxide and graphene nanosheets. The dark region observed in Fig. 26 A represents densely populated layers of graphene oxide, whereas the clear-grey region represents less number of layers at the edges of these nanosheets. Graphene, Fig. 26 B has fewer layers than graphene oxide which is indeed proof that the

reduction process was successfully carried out. These results are in good agreement with those obtained from HRSEM (Fig. 25 A and B). Figure 26 B and C shows HRTEM images of graphene oxide and graphene at low scale view (2 ηm), respectively. The absence of lattice fringes from these images is a clear indication that the surface of the nanosheets is amorphous. Furthermore, the images also show a highly disordered microstructure without any crystallinity on the structure of these carbon based materials. The inset images in Fig. 26 B and D are the SAED images of the graphene oxide and graphene, respectively. The few concentric rings further confirm the amorphous nature of these samples.

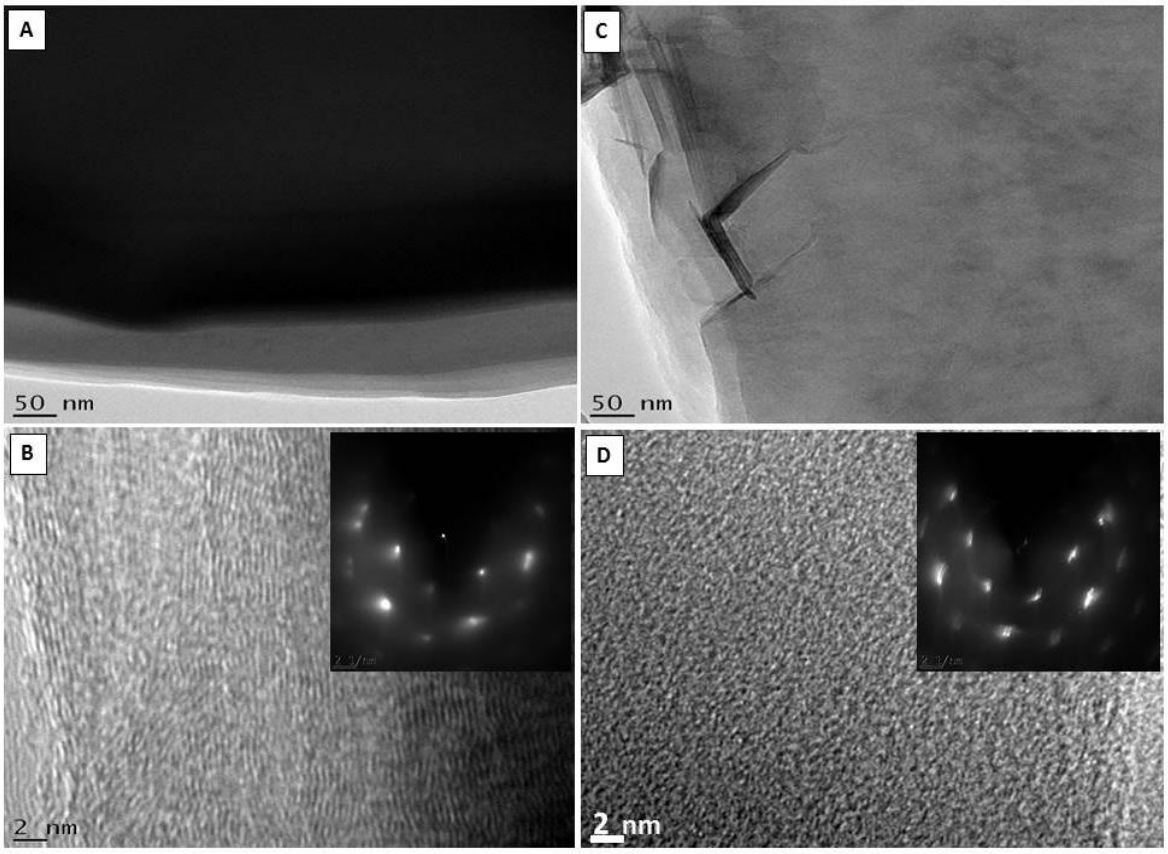

Figure 26: HRTEM images taken at different scales for graphene oxide (A) 50 ηm and (B) 2 ηm, and graphene (C) 50 ηm and (D) 2 ηm. The inserts in (B) and (D) are the SEAD images of graphene oxide and graphene, respectively

EDS analysis of the prepared nanosheets (Fig. 27) was performed using HRTEM in order to determine their chemical composition. It can be observed that both samples consisted of the expected C and O elements. The presence of Cu and Ni are caused by the copper-nickel grid used during sample analysis. The Cl and K impurities that were picked up in the graphene

oxide sample are residues of the precursors in the sample. The presence of Si impurity in graphene is caused by cross contamination during sample preparation.

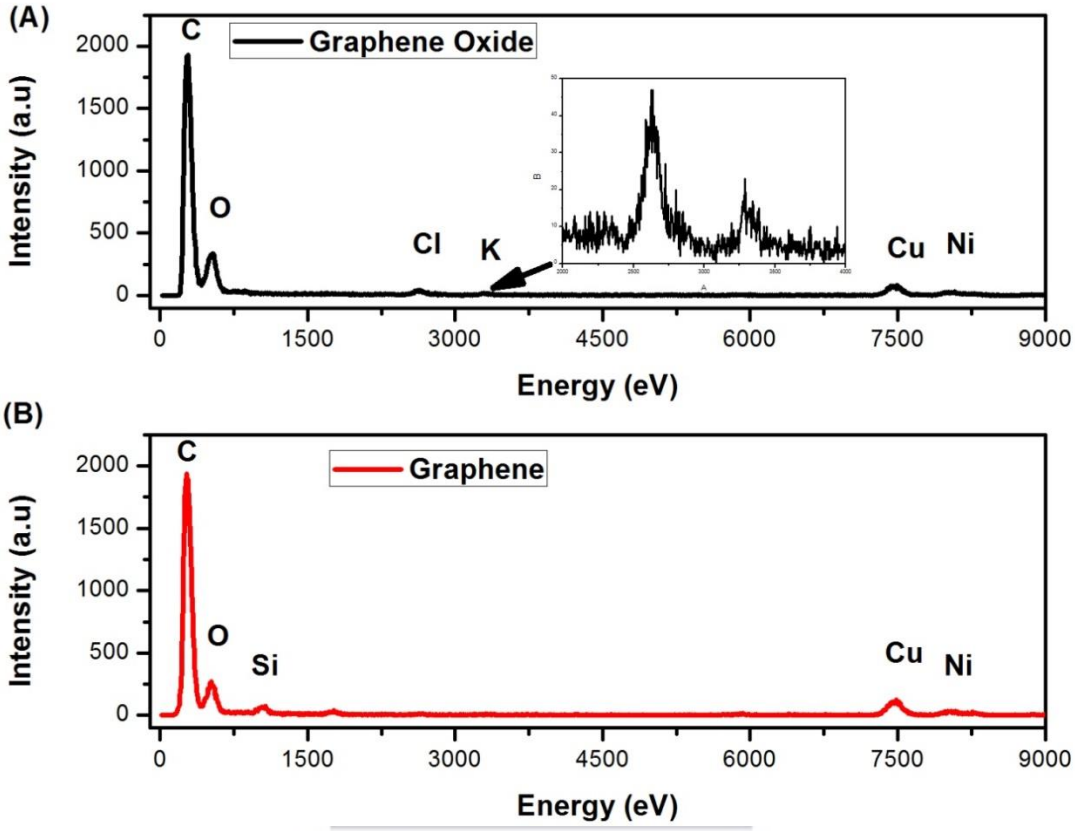

Figure 27: EDS analysis of (A) graphene oxide and (B) graphene using HRTEM

3.2.3. Fourier Transform Infrared Spectroscopy

The molecular structure of commercial graphite, synthesised graphene oxide and graphene samples were investigated using FTIR spectroscopy as shown in Fig. 28. Graphene oxide was synthesized via a modified Hummer's method by oxidizing the graphite powder with $KMnO_4$ as stipulated in Chapter 2, Section 2.5 [33]. The appearance of prominent bands in the FTIR spectrum of graphene oxide signifies that the oxidation process was successful. The spectrum for graphene oxide is characterized by a broad O-H stretching vibration band at 3398 cm^{-1}, small carboxyl C=O stretching band at 1728 cm^{-1}, aromatic vibrational framework at 1635 cm^{-1}, epoxy C-O stretching vibrations at 1177 cm^{-1} and alkoxy C-O stretching vibrations at 1059 cm^{-1}. The presence of O-H groups on the edges on the nanosheets provides good

dispersibility of the nanosheets in water as opposed to graphene nanosheets which are not easily dispersed in water due to the absence of this group [34, 35].

The structural framework of graphene oxide and graphene are comparable. The successful reduction of graphene oxide to form graphene is indicated by the decrease in the intensity and shifting of absorption bands which resemble the absence of most oxygen-containing groups in graphene [36, 37]. Graphene is characterised by a weak hydroxyl (-O-H) stretching vibration band at 3363 cm^{-1}, carbonyl (-C=O) stretching band at 1678 cm^{-1}, intense carboxyl (-COOH) stretching vibration band at 1473 cm^{-1} and the sharp band at 999 cm^{-1} which is attributed to accumulation of oxygen atoms on the edges on the sheets [38, 39].

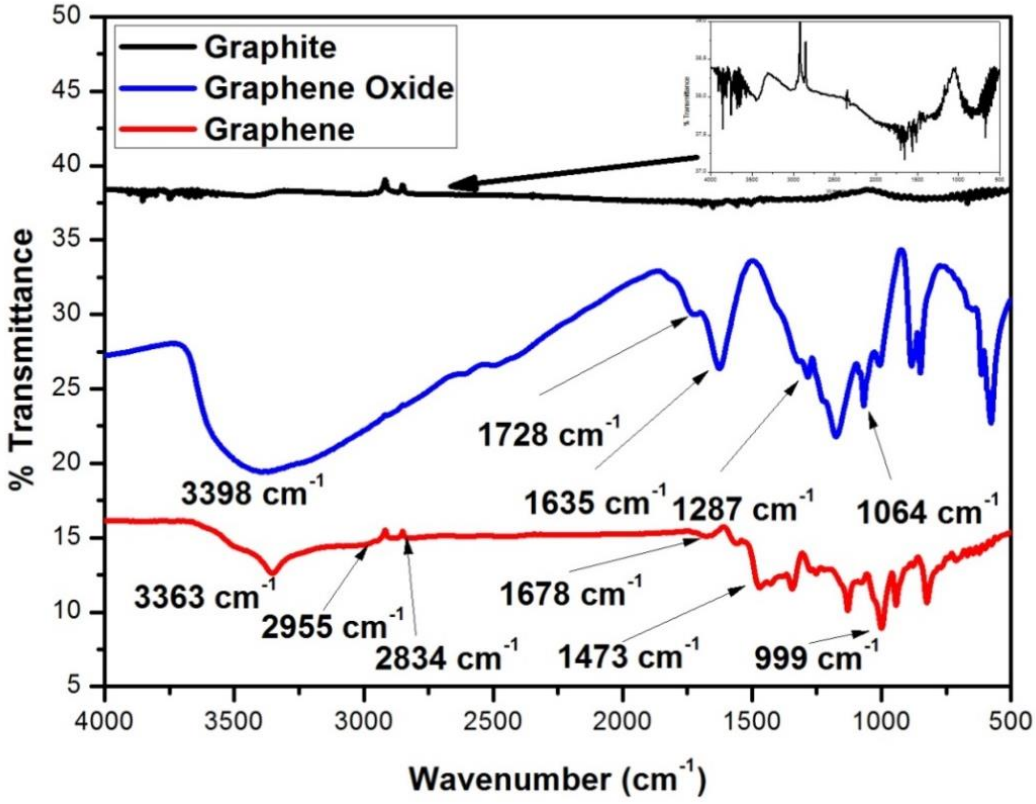

Figure 28: FTIR spectra of graphite, graphene oxide and graphene

3.2.4. Raman Spectroscopy

Raman spectroscopy is an essential analytical tool used for investigating the order and disorder in the structure of carbonaceous materials [40]. The main feature in the Raman

spectra of these materials are the D and G band which appear around 1300 and 1600 cm^{-1}, respectively. The D band is assigned to the breathing mode of k-point phonons of A_{1g} symmetry from the aromatic rings which show the defects in these materials, whereas the G band is assigned to the E_{2g} phonons from the stretching of C sp^2 atoms in both the rings and chains [34, 40].

Figure 29 shows the Raman spectra of graphene oxide and its transformation to graphene. The Raman spectrum for graphene oxide (Fig. 29 A**)** shows a broad D band at 1352 cm^{-1} and G band at 1597 cm^{-1}. The two bands are slightly shifted to lower frequency regions for graphene (Fig. 29 B), as a result the D and G bands appear at 1335 and 1560 cm^{-1}, respectively. The shift in the two bands is attributed to the decrease in the number of layers in the graphene structure which is a clear indication that the reduction process was a success [6, 41]. These results confirm the fewer number of nanosheets that were observed for graphene in both HRSEM and HRTEM techniques. The intensity ratio of the D and the G bands (I_D/I_G) were calculated to further study the transformation from graphene oxide to graphene. The I_D/I_G for graphene was calculated to be 1.23 which is higher than 1.01 for graphene oxide. The large I_D/I_G for graphene indicates that most oxygen-containing groups were removed during reduction with $NaBH_4$ [6].

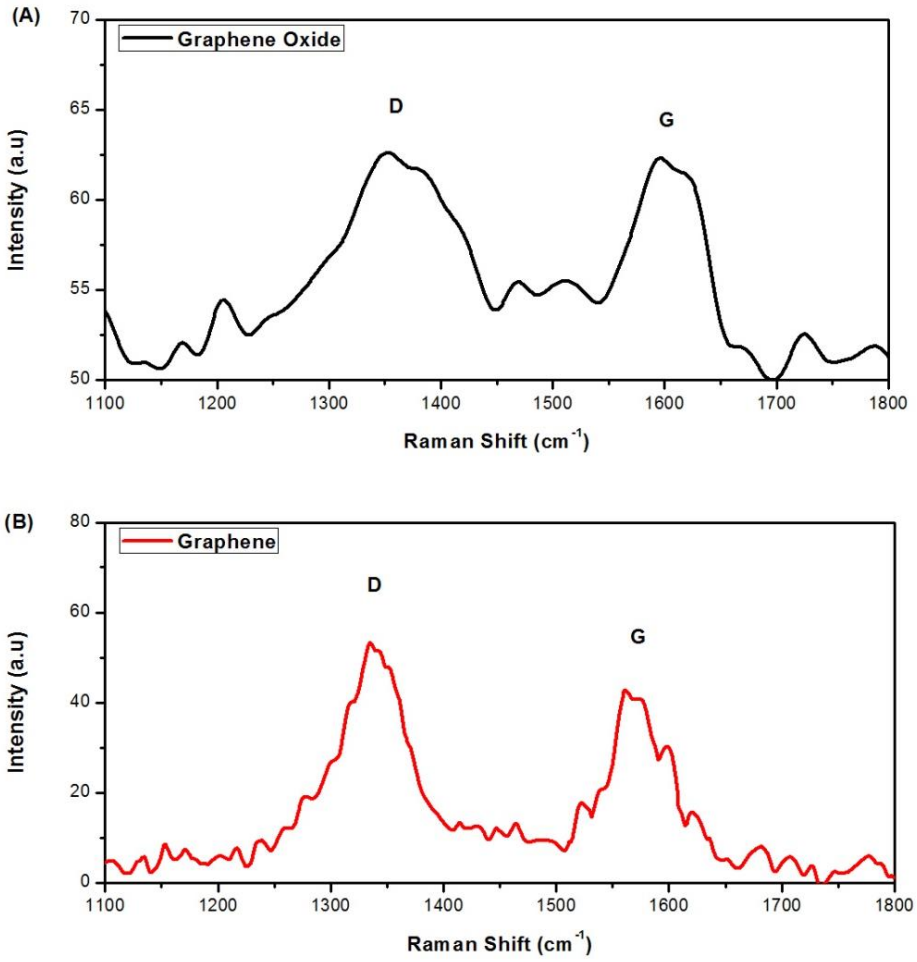

Figure 29: Raman spectra of (A) graphene oxide and (B) graphene

3.2.5. X-ray Diffraction

Figure 30 shows structural studies of graphene oxide and graphene nanosheets using XRD. The XRD pattern of graphene oxide has two sharp peaks at 6 º and 42 º 2Θ values, where the first peak is indexed to the (001) and the latter (100) planes. The broad peak between 15 and 40 º can be indexed to the (002) plane and indicates the amorphous nature of the graphene oxide nanosheets. The broad peak also shows that there is no order in the arrangement carbon atoms in the graphene oxide nanosheets. The decrease in the intensity of the (001) and the sharpening of the (002) planes is related to the ordered carbon structure of graphene which indicates the successful reduction of graphene oxide.

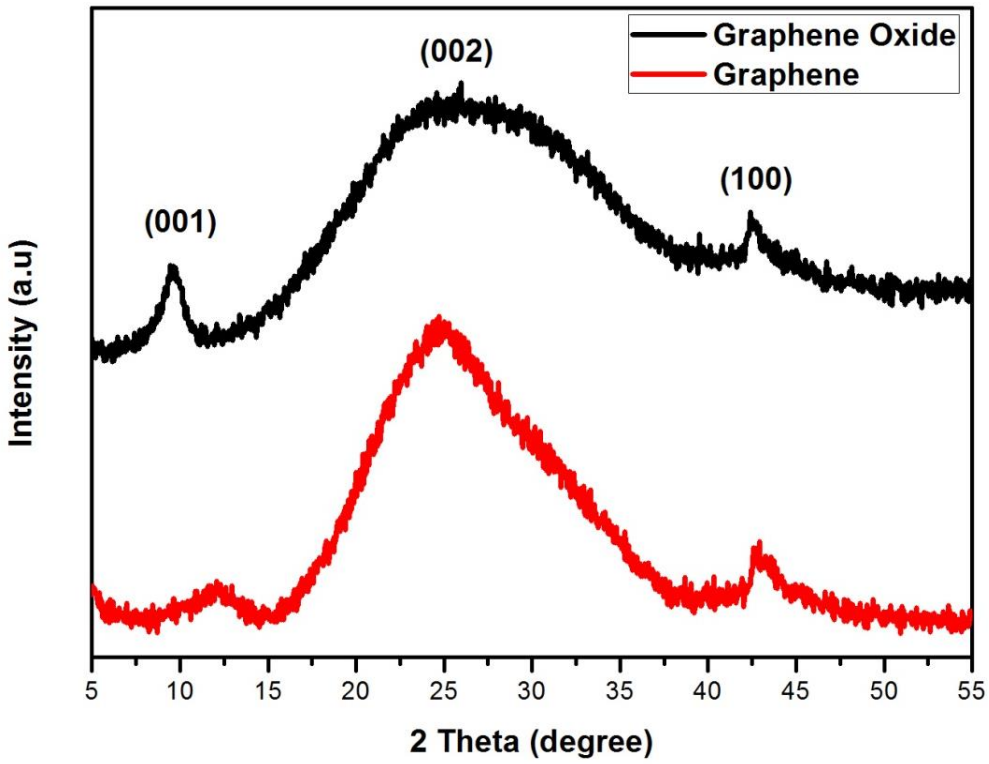

Figure 30: XRD patterns of graphene oxide and graphene nanosheets

3.2.6. Thermogravimetric (TG) Analysis

The thermal stability of graphene oxide and graphene nanosheets were directly determined using TG analysis from room temperature to 900 ºC as shown in Fig. 31. The TG curve for graphene oxide shows four weight loss processes: the first weight loss (~15 %) can be observed from room temperature to 120 ºC and is attributed to evaporation of adsorbed water molecules on edges on these nanosheets. The second and the third weight loss appeared between 150 and 300 ºC, and can be ascribed to the decomposition of labile oxygen-containing functional groups such as carboxylic and anhydride [39, 42]. The last degradation step above 300 ºC can be attributed to the removal of stable oxygen-containing functional groups such as phenol, quinone and carbonyl [42].

The TG curve of graphene shows three degradation steps: from room temperature to 120 ºC and 240 to 450 ºC (indicated by the inset) can be ascribed to the removal of adsorbed water molecules and a few oxygen-containing groups found on the edges of the nanosheets. The

last step above 450 ºC can be attributed to the removal of stable oxygen-containing groups. The TG curve clearly shows that graphene has the smallest weight loss (38 %) compared to graphene oxide (69 %), therefore the material shows higher thermal stabilities in the given temperature range.

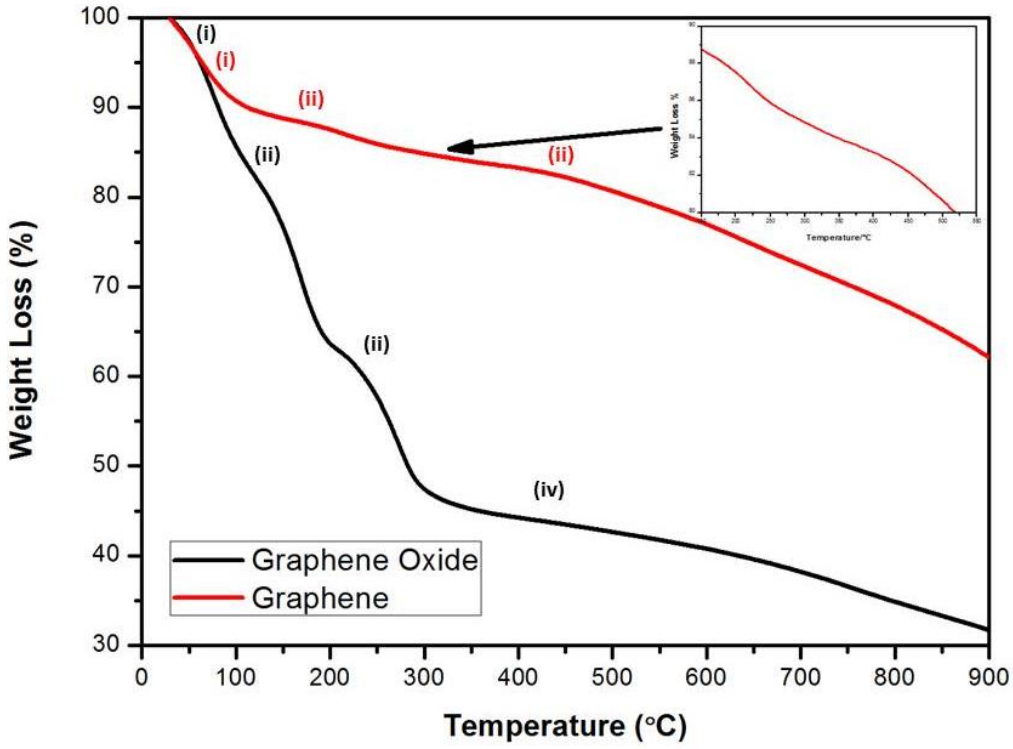

Figure 31: TG curves of graphene oxide and graphene (inset shows the second degradation step for graphene)

3.3. Characterisation of $LiFePO_4$-Li_2MnSiO_4 and graphenised $LiFePO_4$-Li_2MnSiO_4 hybrid cathode materials

3.3.1. High Resolution Scanning Electron Microscopy

HRSEM was used to study the morphology of the synthesised hybrid cathode materials as shown in Fig. 32. The hybrid materials prepared via the hand milling method (Fig. 32 A and B) shows agglomerated spherical nanoparticles. These materials were prepared in an open-air environment and the presence of moisture and oxygen contributed towards agglomeration of these nanoparticles. The *in situ* sol-gel-prepared hybrid cathode materials show evenly distributed spherical nanoparticles with minimal agglomeration. These nanoparticles were uniformly distributed because of better mixing offered by the sol-gel approach and the use of a moisture-free environment.

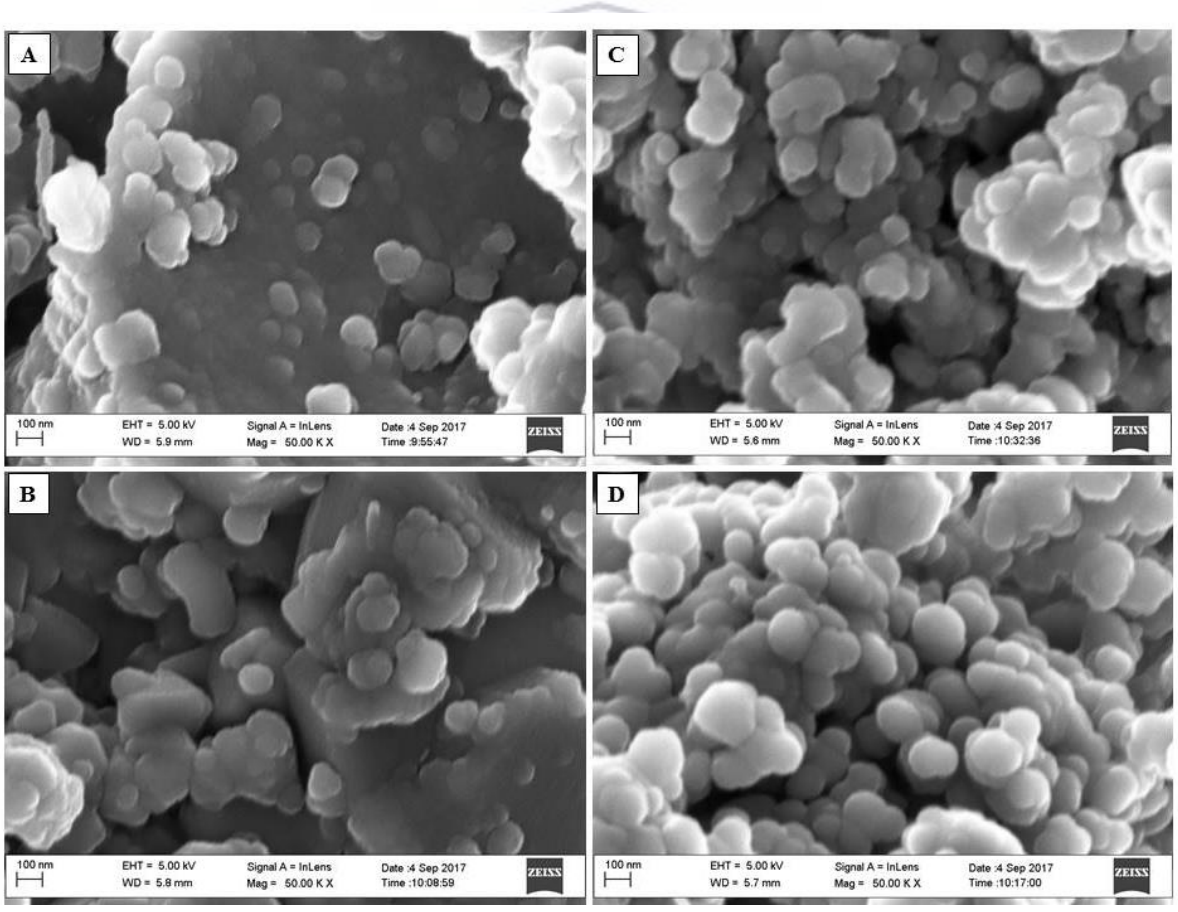

Figure 32: HRSEM image for (A) LFP-LMS HM, (B) LFP-LMS-G HM, (C) LFP-LMS SG and (D) LFP-LMS-G SG at a magnification of 100.00 KX

Table 6 shows elemental mapping of the synthesised cathode materials and there were no impurities observed in all the samples.

Table 6: Elemental mapping of the synthesised hybrid cathode materials

	LFP-LMS HM	**LFP-LMS-G HM**	**LFP-LMS SG**	**LFP-LMS-G SG**
Element	**Weight %**			
O	40.0	40.42	40.39	35.85
Si	2.04	1.58	2.51	0.84
P	10.34	13.04	17.9	16.59
Mn	31.12	25.4	11.35	18.09
Fe	16.5	19.56	27.86	28.64
Total	100	100	100	100

3.3.2. High Resolution Transmission Electron Microscopy

The HRTEM images in Fig. 33 confirmed similar results obtained from HRSEM. The LFP-LMS HM and LFP-LMS-G HM hybrid materials were highly agglomerated which made it difficult to measure their particle size. The LFP-LMS SG and LFP-LMS-G SG hybrid materials revealed spherical nanoparticles with particle sizes of 45 and 25 ηm, respectively. The presence of graphene nanosheets contributed towards the dispersion and particle size reduction in LFP-LMS-G SG. As it is shown by Fig. 33 D, the graphene nanosheets are not clearly observed at high scale view because of their low content (6 % weight) and good mixing offered by the sol-gel technique. However, the hand milling technique showed poor mixing between graphene nanosheets and LFP-LMS nanoparticles as evidenced by regions where the nanosheets are folded in one place whereas the nanoparticles are clustered in another as shown by Fig. 33 B.

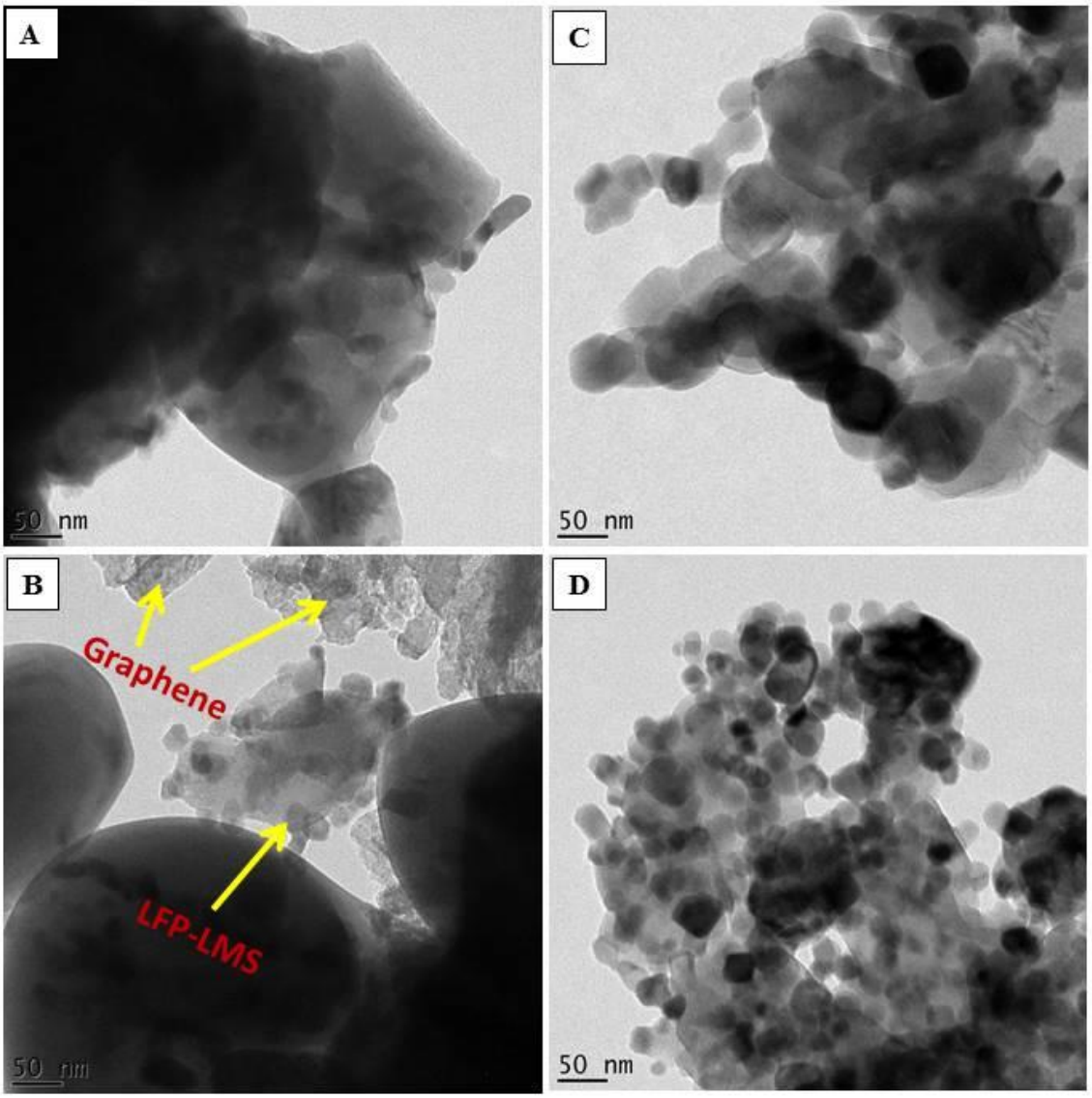

Figure 33: HRTEM images of (A) LFP-LMS HM, (B) LFP-LMS-G HM, (C) LFP-LMS SG and (D) LFP-LMS-G SG at a scale view of 50 ηm

The microstructural properties of the hybrid cathode materials were interrogated using HRTEM at low scale view (2 ηm) as indicated by Fig 34. All the hybrid cathode materials showed lattice fringes which are associated with the crystallinity of these materials. Furthermore, the graphenised hybrid cathode materials (Fig. 34 B and D) revealed that the nanoparticles were coated with graphene nanosheets.

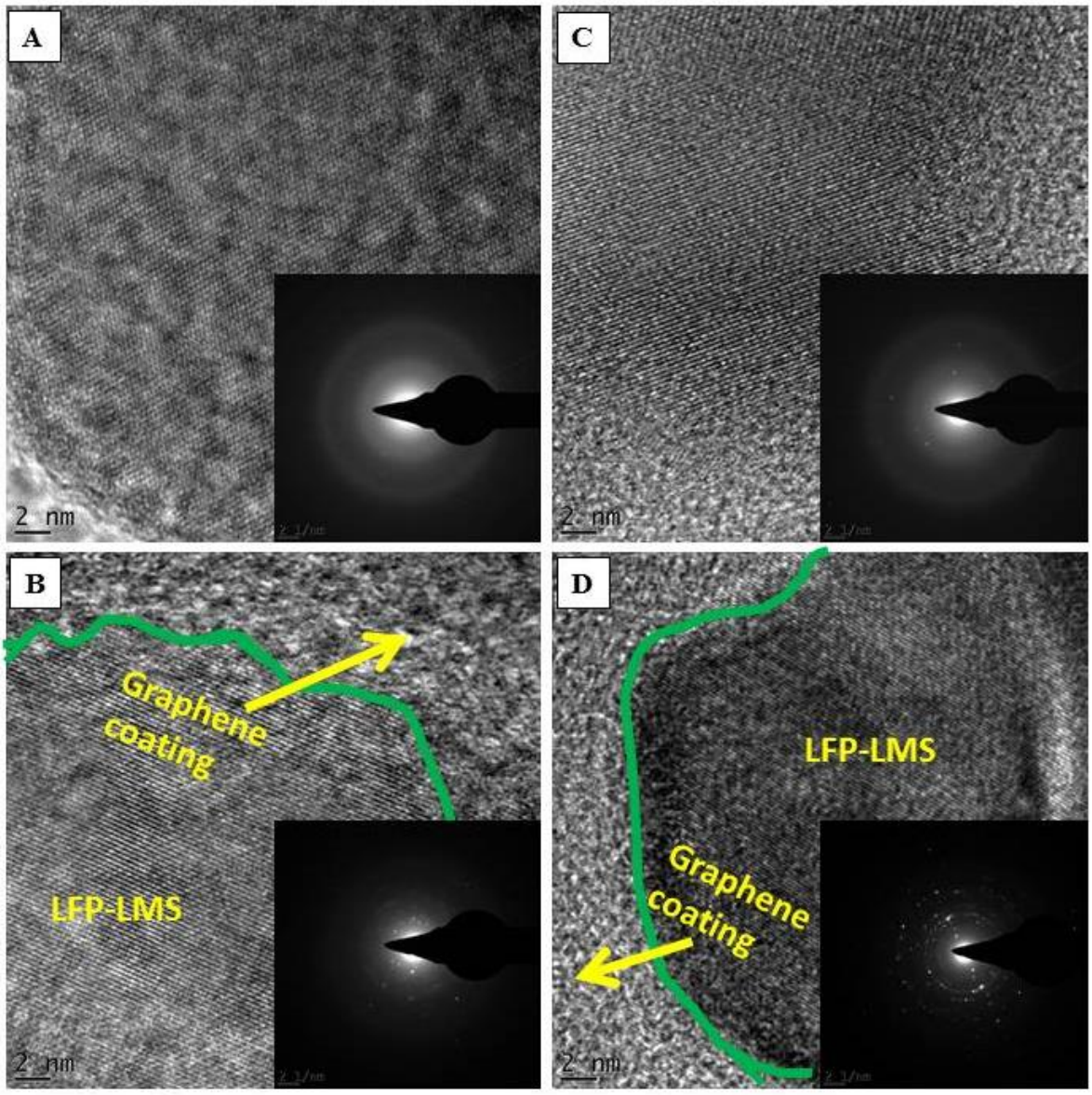

Figure 34: HRTEM images of (A) LFP-LMS HM, (B) LFP-LMS-G HM, (C) LFP-LMS SG and (D) LFP-LMS-G SG at low scale view of 2 ηm. The inserts are the SAED images corresponding to these hybrid cathode materials

Elemental mapping of the hybrid materials was confirmed again using EDS from HRTEM as indicated in Fig. 35. These finding are in agreement with the theory that there is better mixing with the *in situ* sol-get method compared to hand milling method. There is an almost even distribution of Fe and Mn in all the *in situ* sol-gel-prepared materials (Fig. 35 C and D) which is not the case in the materials prepared using the hand milling approach (Fig. 35 A and B. Again, the high content of O is attributed to oxygen in the PO_4 and SiO_4 groups.

The presence of Cu and Ni is caused by the copper-nickel grid used for analysis of the samples. There were also a few impurities of S and Ca in LFP-LMS HM and LFP-LMS SG, respectively.

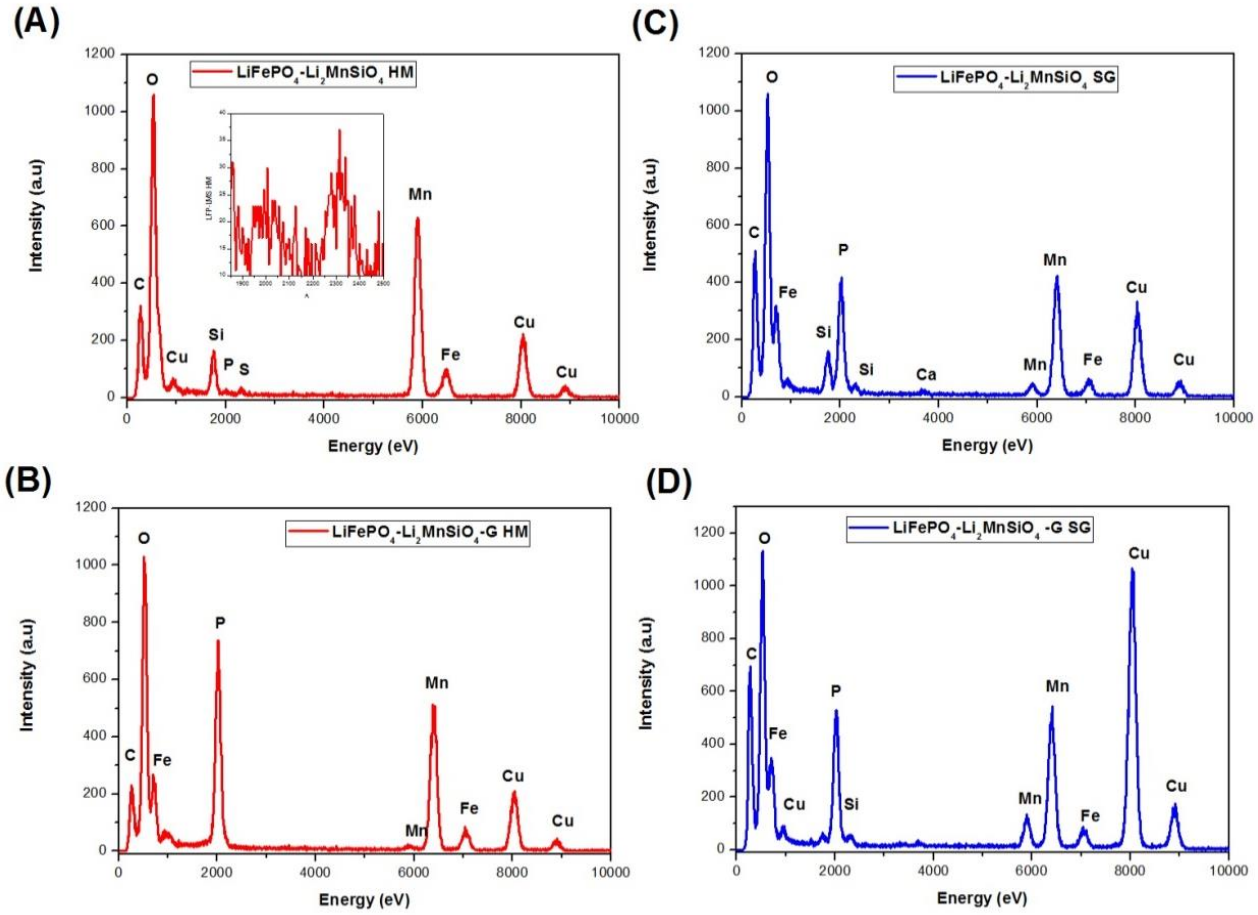

Figure 35: EDS spectra of all the synthesised hybrid cathode materials: where (A) and (B) represents the hand milling method and (C) and (D) the *in situ* sol-gel method

3.3.3. Small Angle Scattering X-Ray (SAXS)

The morphology and particle size distribution of the synthesised hybrid materials were further confirmed using SAXS as shown in Fig. 36. The slightly bell shaped peak of the pair-distance distribution function (PDDF) curves (Fig. 36 A) confirmed that these materials have an oblate/lamellar shape (described as spherical in HRSEM and TEM) having diameters of 36, 30, 37 and 23 ηm for LFP-LMS HM, LFP-LMS-G HM, LFP-LMS SG and LFP-LMS-G SG, respectively. Indeed, the presence of graphene in both hybrid materials played a

significant role in particle size reduction, more especially in the LFP-LMS-G SG. The particle size distribution curves (Fig. 36 B) show that the hybrid cathode materials had a distribution in their particle sizes from 5 to 65 ηm.

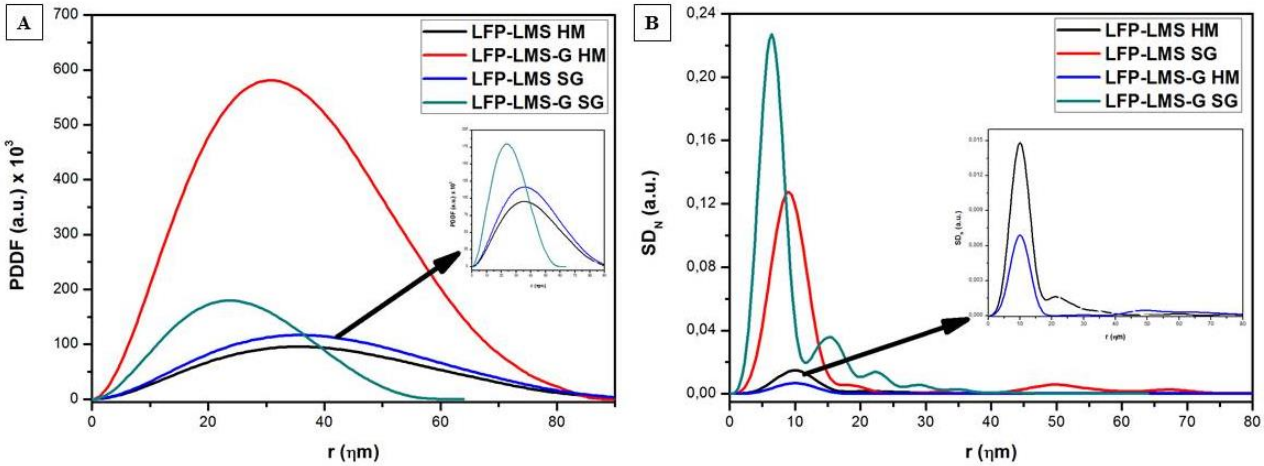

Figure 36: SAXS data: (A) PDDF (insert: the shape of the seemingly broad curves without the influence of LFP-LMS-G HM) and (B) particle size distribution curves (inset: zoomed area of the curves) of the prepared hybrid cathode materials

3.3.4. Fourier Transform Infrared Spectroscopy (FTIR)

Figure 37 shows the FTIR spectra of the LFP-LMS HM, LFP-LMS-G HM, LFP-LMS SG and LFP-LMS-G SG hybrid cathode materials. The hybrid cathode materials show a set of three bands in the region between 400 and 1600 cm^{-1}. In the low wavenumber region, the band at 455 cm^{-1} is attributed to the local Li-ion environment or rather Li-ion motion form $LiFePO_4$ and Li_2MnSiO_4 in the hybrid materials [9, 43]. The second band appearing between 535 and 665 cm^{-1} is ascribed to the bending vibrations of the $[PO_4]^{3-}$ unit of $LiFePO_4$ as well as the ν_1 and ν_4 modes of $[SiO_4]$ in Li_2MnSiO_4 [10]. In the high wavenumber region, the band between 940 and 1240 cm^{-1} was observed and is due to the stretching vibrations of $[PO_4]^{3-}$ and the ν_1, and ν_4 modes of $[SiO_4]$ [8, 9]. The LFP-LMS HM and LFP-LMS-G HM hybrid cathode materials contained Li_2SiO_3 impurity observed at 862 cm^{-1}. However, this impurity was not observed in LFP-LMS SG and LFP-LMS-G SG hybrid cathodes.

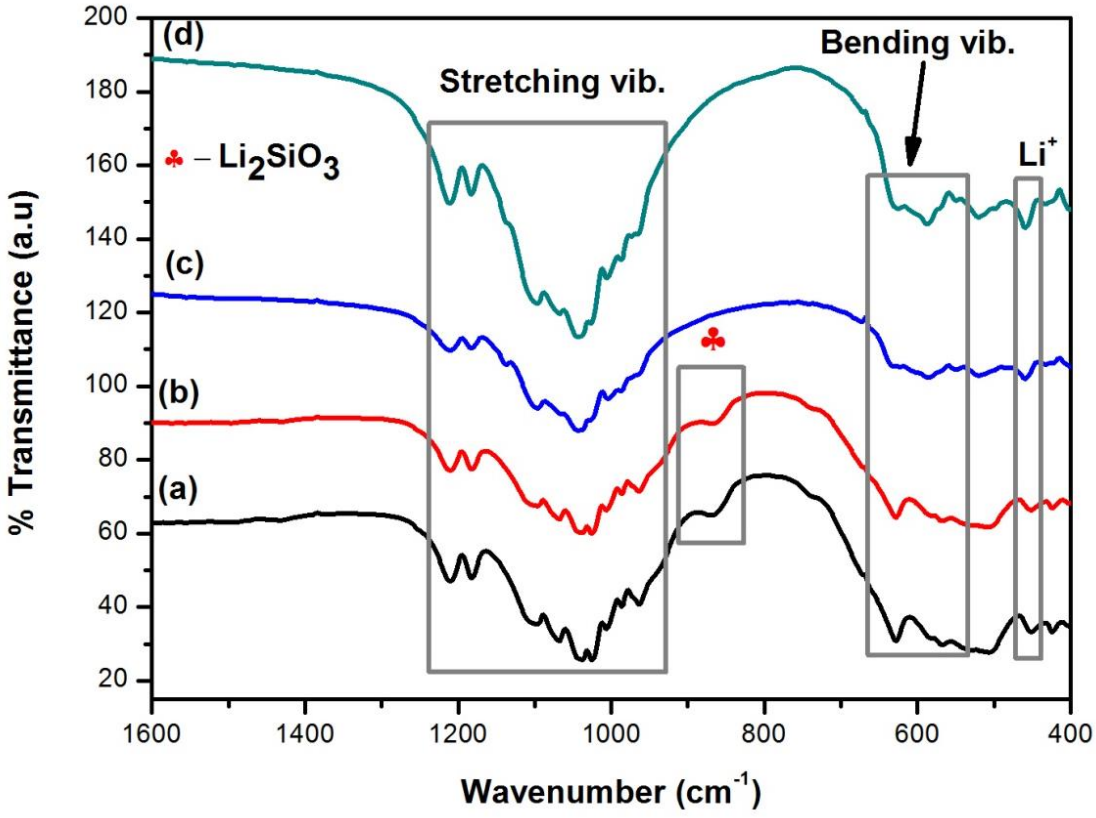

Figure 37: FTIR spectra of (a) LFP-LMS HM, (b) LFP-LMS-G HM, (c) LFP-LMS SG and (d) LFP-LMS-G SG

3.3.5. X-Ray Diffraction

The structure of the hybrid cathode materials was studied using X-ray diffraction in the 2Θ range from 10 to 80 º as shown in Fig. 38. The sharp diffraction peaks are a clear indication that the powder samples have a crystalline structure. There are no obvious changes in the diffraction peak positions of the LFP-LMS HM and LFP-LMS-G HM (Fig. 38 A and B) with respect to those of the pristine materials (Fig. 16, Section 3.1.5). However, there are changes observed in the diffraction patterns of LFP-LMS SG and LFP-LMS-G SG shown by the disappearance of two intense peaks at 2Θ = 19 and 44 º. An explanation for the disappearance of these diffraction peaks in the hybrid material is that the pristine LMS was calcined separately before being incorporated into the hybrid cathodes. Therefore, calcining the material again at high temperatures during the preparation of the hybrid might have caused structural changes; hence the disappearance of the two peaks. These results suggest that the hybrid cathode materials prepared using the *in situ* sol-gel method had diffraction patterns

similar to those of LFP more than LMS. The hybrid cathodes prepared using the hand milling approach on the other hand showed a pattern that resembles the presence of both pristine cathode materials.

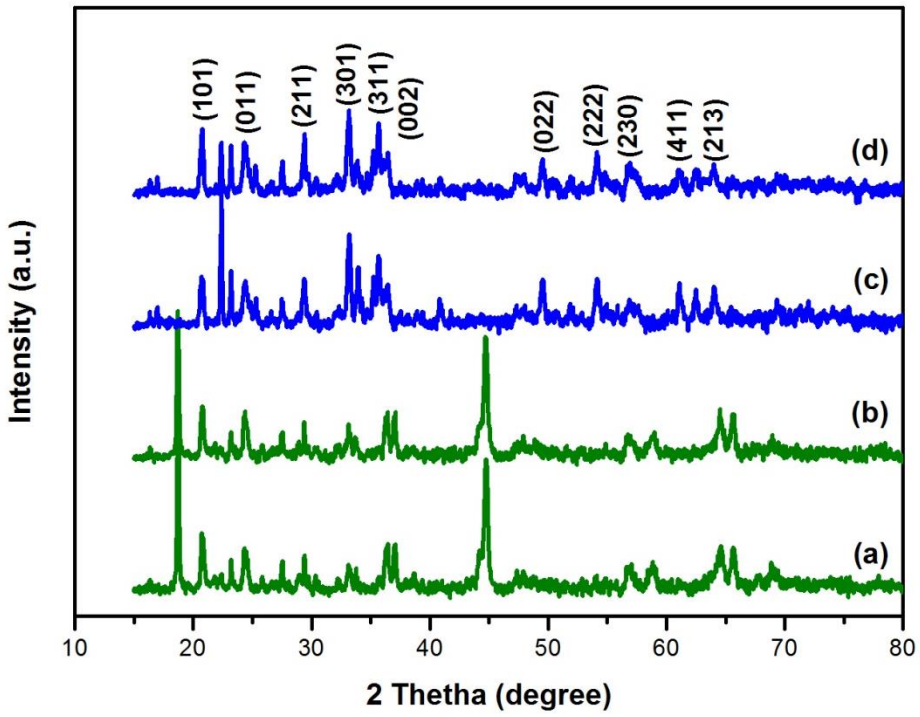

Figure 38: X-Ray diffraction patterns of (a) LFP-LMS HM, (b) LFP-LMS-G HM, (c) LFP-LMS SG and (d) LFP-LMS-G SG

3.3.6. Thermogravimetric (TG) Analysis

Figure 39 shows the TG analysis of the different hybrid cathode materials under N_2 atmosphere from room temperature to 900 ºC. As can be seen from this Figure, the total weight loss of LFP-LMS HM, LFP-LMS-G HM, LFP-LMS SG and LFP-LMS-G SG were 5.9 %, 9.9%, 4.5 % and 3.4 %, respectively. The LFP-LMS-G SG has the highest thermal stability with only just 3.4 % weight loss which is ascribed to the crystallization of this material [15]. In contrast, LFP-LMS-G HM showed inferior thermal stabilities compared to other materials with a weight loss of 9.9 %. It can be observed that both hand-mill-prepared hybrid cathode materials showed weight gain from room temperature to approximately 450 ºC compared to those prepared via the *in situ* sol-gel approach which only showed a weight

decrease with an increase in temperature. The hand-mill-prepared hybrid cathodes were prepared in open-air environment therefore the weight gain could be caused by the reaction of absorbed moisture and the N_2 atmosphere inside the furnace.

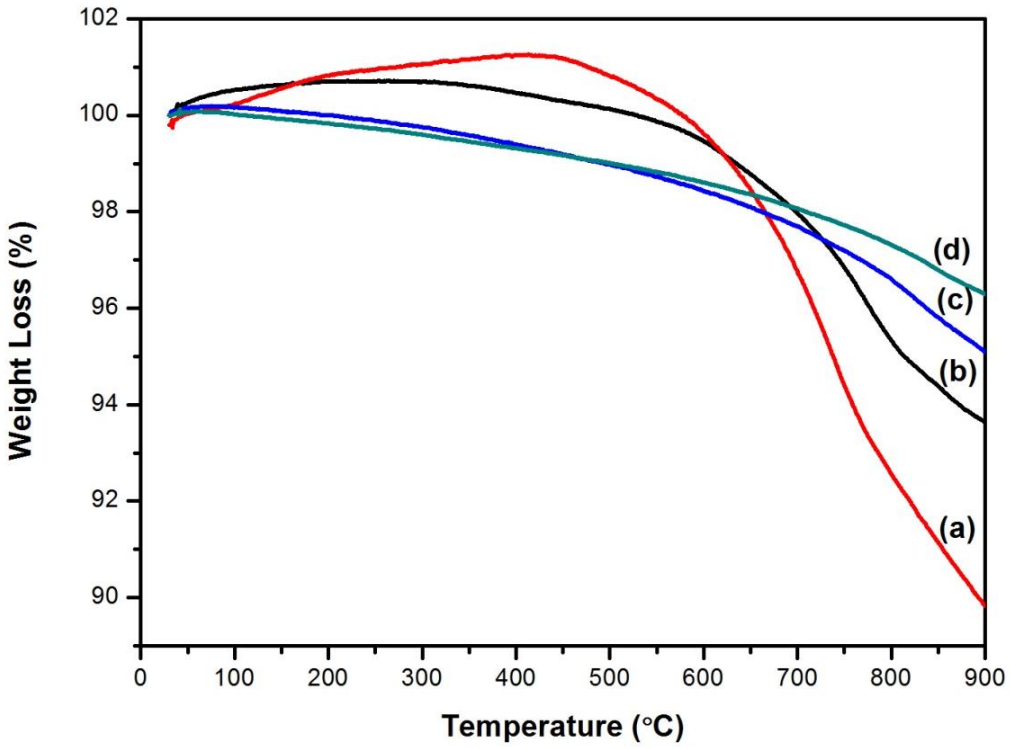

Figure 39: TG curves of the synthesised (a) LFP-LMS-G HM, (b) LFP-LMS HM, (c) LFP-LMS SG and (d) LFP-LMS-G SG hybrid cathode materials

3.3.7. Electrochemistry

3.3.7.1. Cyclic Voltammetry

The electrochemical behaviour of the synthesised hybrid cathode materials; LFP-LMS HM, LFP-LMS-G HM, LFP-LMS SG and LFP-LMS-G SG were studied using cyclic voltammetry and the results are shown in Fig. 40. Figure 40 A shows three redox peaks observed for during the oxidation and reduction scans of LFP-LMS HM and LFP-LMS-G HM in the given potential window between -1000 and 800 mV. The absence of the oxidation peak in iron is associated with the used electrolyte. The peak potentials corresponding to these peaks are shown in Table 7. It is clear that the graphenised hybrid cathode material has a high current compared to LFP-LMS hybrid cathode. The high current of this material is associated with an

improved capacity attributed to the presence of graphene. The capacity values for these materials were calculated the same way as the pristine materials and are tabulated in Table 8.

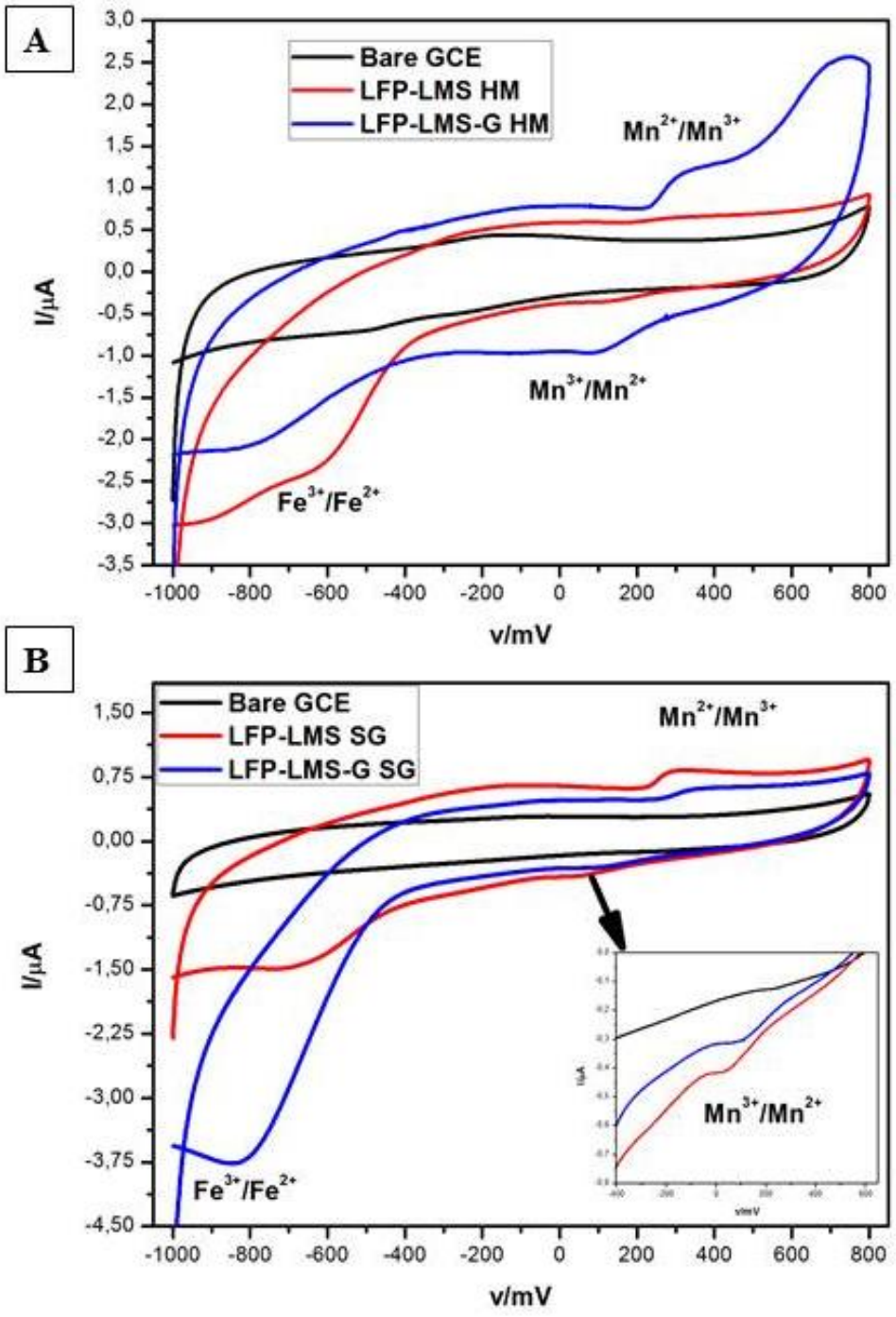

Figure 40: Cyclic voltammograms of (A) hybrid cathodes prepared via the hand milling and (B) *in situ* sol-gel methods in 1.0 M $LiClO_4$ in the potential window between -1000 and 800 mV, at a scan rate of 05 mV s^{-1}

Table 7: The observed peaks characterised by these peak potentials and currents for the prepared hybrid cathode materials

Materials	E_{pa}/mV	I_{pa}/μA	E_{pc1}/mV	I_{pc1}/μA	E_{pc2}/mV	I_{pc2}/μA
LFP-LMS HM	285	0.64	108	-0.36	-800	-2.09
LFP-LMS-G HM	331	1.20	78	-0.96	-646	-2.40
LFP-LMS SG	348	0.61	35	-0.42	-702	-1.49
LFP-LMS-G SG	295	0.82	89	-0.31	-840	-3.76

Figure 40 B shows cyclic voltamogramms for LFP-LMS and LFP-LMS-G hybrid cathode materials prepared using the *in situ* sol-gel approach. These materials show the same shape and number of peaks as those prepared via the hand milling method. The corresponding peak potentials and calculated capacities for these materials are also presented in Tables 7 and 8, respectively. The results clearly show that both graphenised LFP-LMS hybrid cathode materials offer higher capacities than those of LFP-LMS hybrid cathodes and this is associated with the presence of graphene nanosheets in these samples. The LFP-LMS-G SG hybrid cathode showed the highest specific capacity of 4.056 mA h g^{-1} compared to LFP-LMS-G HM with 3.408 mA h g^{-1}. These results clearly show that the *in situ* sol-gel method yielded better performing hybrid cathodes than the hand milling method.

Table 8: Calculated capacities for the hybrid cathode materials

Materials	Specific capacity/mA h g^{-1}
LFP-LMS HM	2.804
LFP-LMS-G HM	3.408
LFP-LMS SG	2.524
LFP-LMS-G SG	4.056

The cyclic voltammograms of LFP-LMS-G HM and LFP-LMS-G SG at different scan rates (01 to 09 mV s^{-1}) are shown in Fig. 41. Both graphenised hybrid cathodes exhibit an irreversible behaviour supported by the differences between peak potentials which increases with an increase in scan rates. On the contrary, the reduction peak of iron in LFP-LMS-G HM (Fig 41 A) is less pronounced compared to that of LFP-LMS-G SG (Fig 41 B) which is associated with the different methods used for preparation of these hybrid cathodes. As a result, the more pronounced reduction peak of iron in LFP-LMS-G SG overshadows the redox pair of manganese in this hybrid cathode.

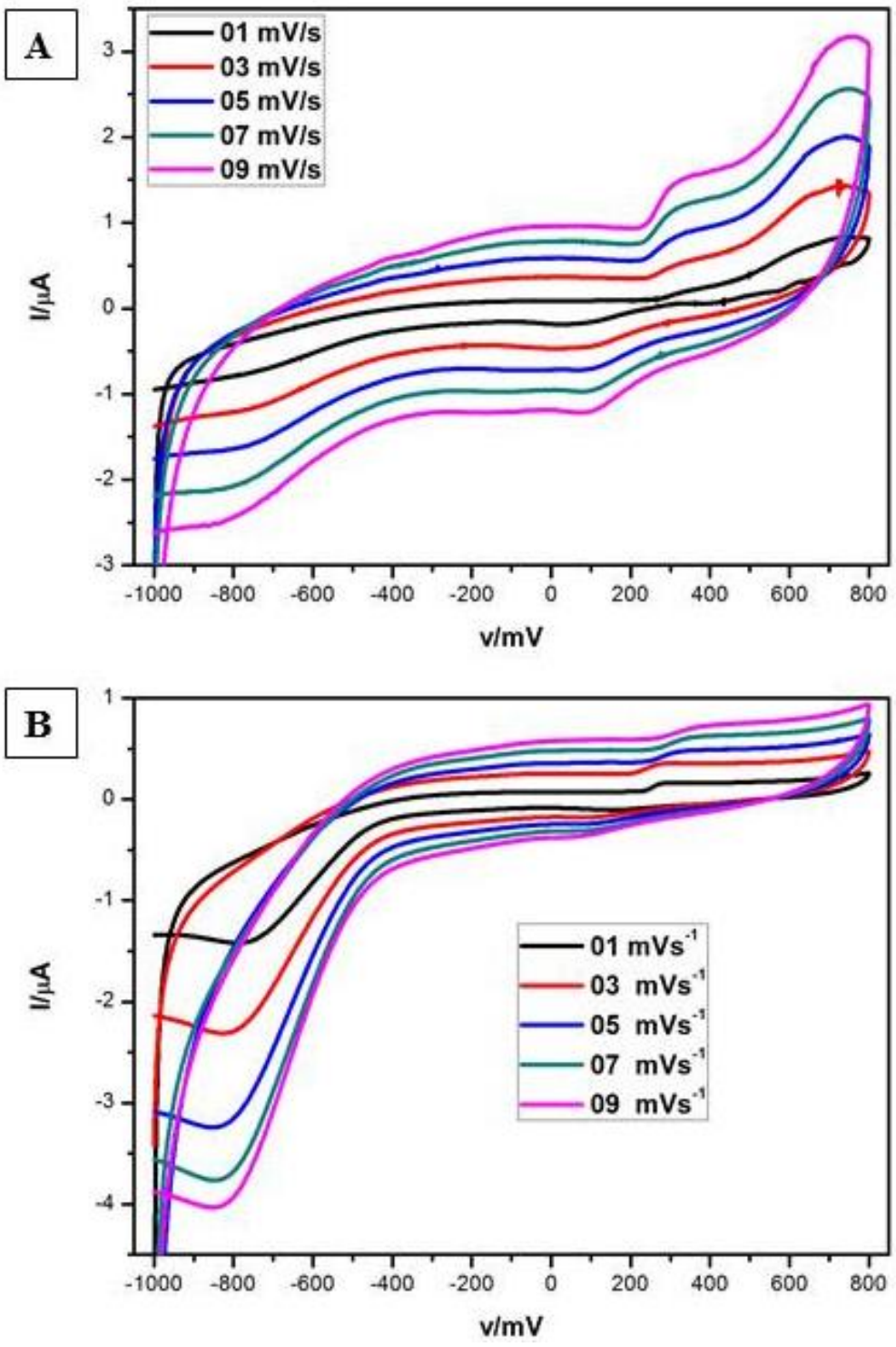

Figure 41: Cyclic voltammograms for (A) LFP-LMS-G HM and (B) LFP-LMS-G SG hybrid cathodes in 1.0 M $LiClO_4$ at different scan rates between 01 - 09 mV s^{-1}

3.3.7.2. Electrochemical Impedance Spectroscopy

EIS studies for the hybrid cathode materials were discussed using the Nyquist plots (Fig. 42) and Bode plots (Fig. 43). The Nyquist plots for these materials are represented in Fig. 42 A and B and it can be clearly observed that these plots only show an inclined line without any semi-circle (see inset graphs), which is characteristic of a capacitive behaviour. This line is attributed to the Warburg impedance associated with Li-ion diffusion in the bulk electrode, which suggests that the kinetics of the intercalation/de-intercalation process is controlled by the diffusion process [31]. These plots were best fitted using the modified Randles equivalent circuits shown in Fig. 42 C and D, which corresponds to the unmodified and graphenised hybrid cathodes, respectively. The obtained values for the fitted parameters are shown in Table 9. It can be observed that both graphenised hybrid cathodes show a low solution resistance and low charge transfer resistance which is an indication that these materials have fast kinetics compared to the unmodified hybrid cathodes. Further comparison between the two graphenised cathodes shows that the one prepared via the *in situ* sol-gel method has the fastest kinetics, which can be attributed to small particle size and coating with graphene nanosheets.

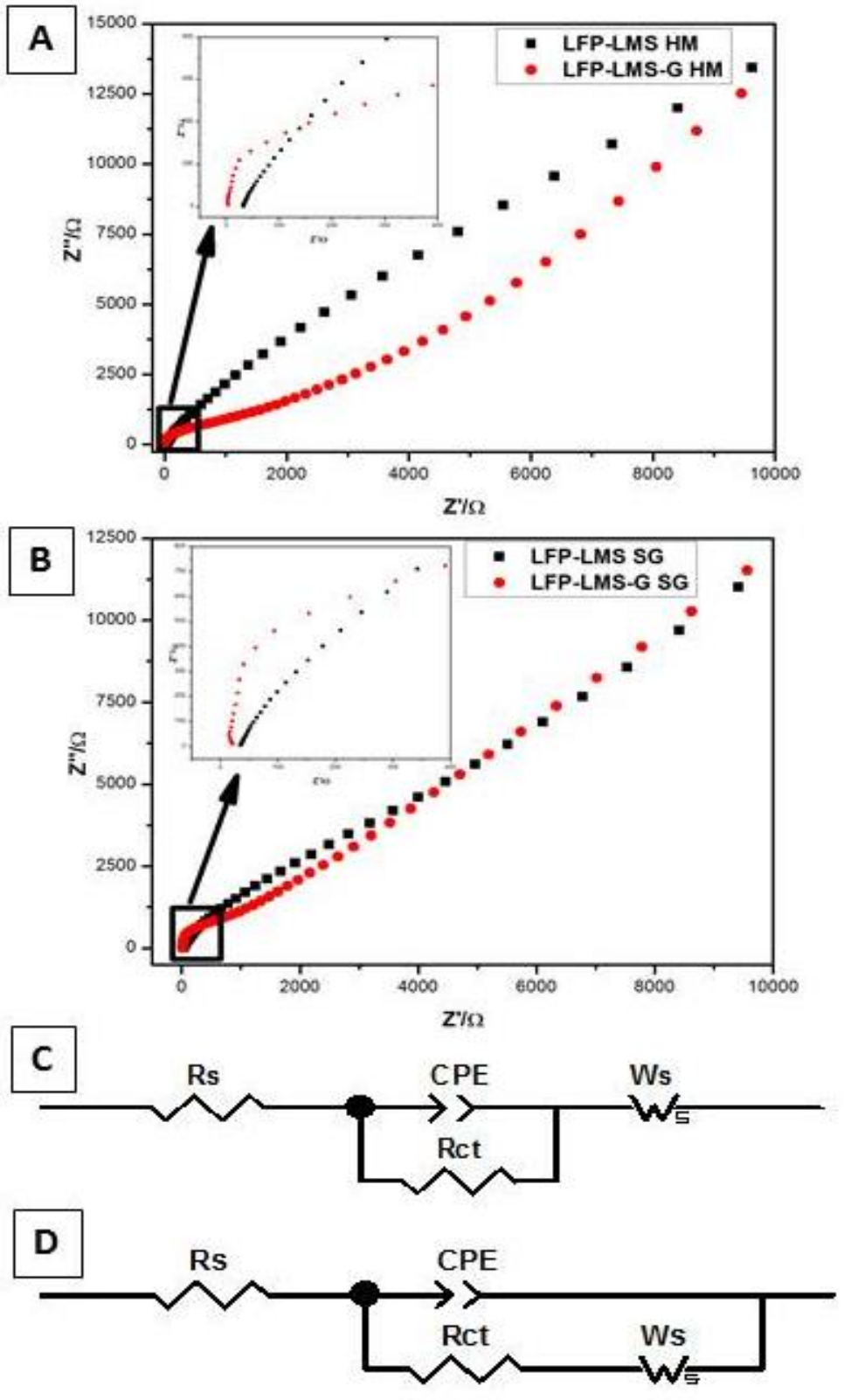

Figure 42: Nyquist plots for hybrid cathode materials prepared via (A) the hand milling method and (B) *in situ* sol-gel method and the corresponding Randles equivalent circuits (C) and (D) for the LFP-LMS and LFP-LMS-G hybrid cathode materials, respectively

Table 9: The fitted parameters of the Randles equivalent circuit for the hybrid cathode materials

Material	R_s/Ω	*CPE*/F	R_{ct}/Ω	$W_s/\Omega\ s^{-1/2}$
LFP-LMS HM	28.01	5.09×10^{-6}	54589	0.147
LFP-LMS-G HM	5.42	4.98×10^{-8}	586.3	0.857
LFP-LMS SG	31.56	5.11×10^{-6}	3954	0.913
LFP-LMS-G SG	2.73	2.24×10^{-9}	389.5	0.632

The high performance of the graphenised hybrid cathodes is further highlighted using the Bode plots as shown in Fig. 43. The LFP-LMS-G HM exhibited a higher phase angle max. at 96.6 º and low impedance of 3.97 Ω compared to the phase angle max. at 69.4 º and impedance of 4.24 Ω for LFP-LMS HM. In addition, the LFP-LMS-G SG had the highest phase angle max. at 113.9 º with a slightly high impedance of 4.44 Ω compared to LFP-LMS SG with a phase angle max at 66.4 º and impedance of 4.11 Ω. The LFP-LMS-G HM hybrid shows fast kinetics while the LFP-LMS-G SG has conducting properties attributed to low impedance and higher phase angle max., respectively.

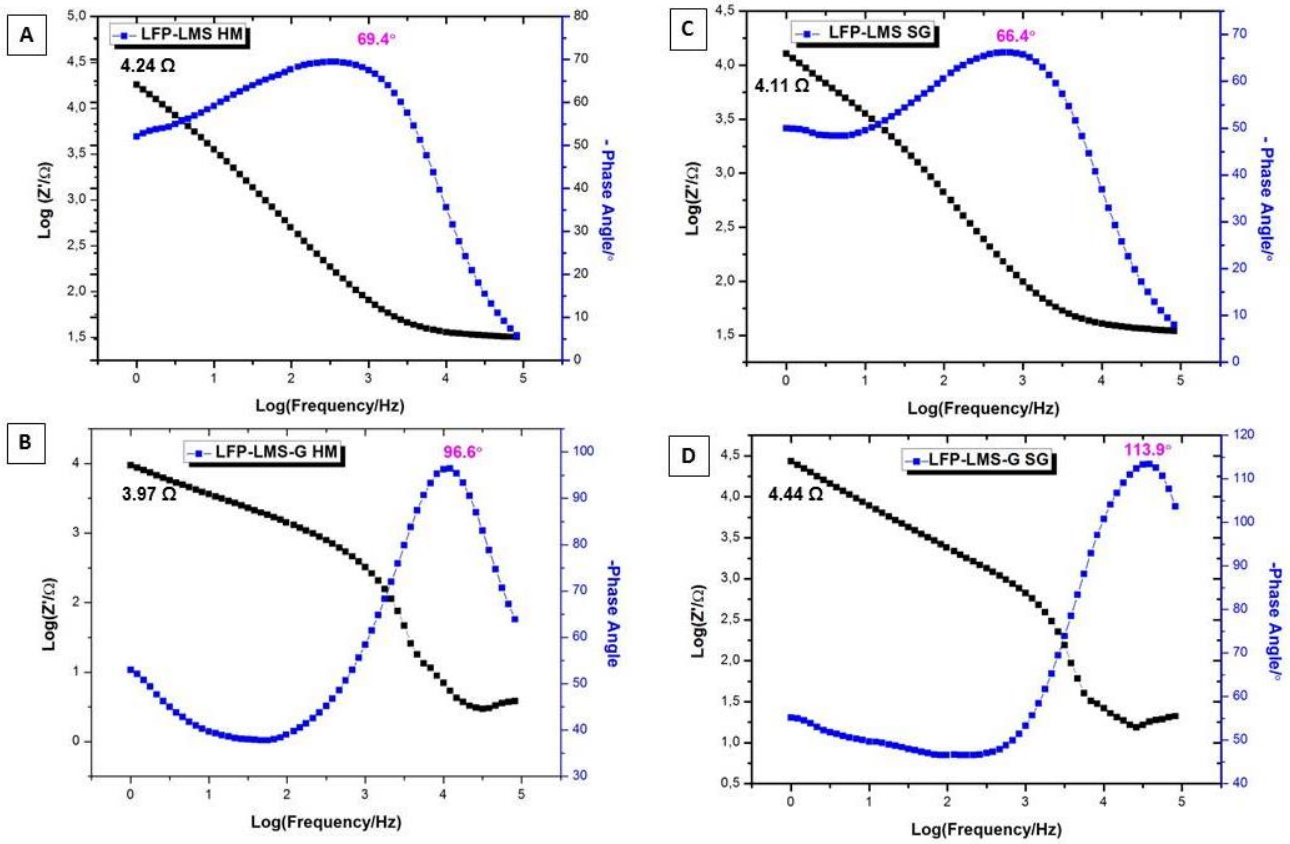

Figure 43: Bode plots for (A) LFP-LMS HM, (B) LFP-LMS-G HM, (C) LFP-LMS SG and (D) LFP-LMS-G SG hybrid cathode materials

The kinetics of these hybrid cathodes were determined using the plots of Z' vs $\omega^{-1/2}$ as shown by Fig. 44. The slope of these plots gave the Warburg coefficients (σ) which were used to calculate the apparent diffusion coefficients (D_{app}) using the following Equation:

$$D_{app} = \left(\frac{\sqrt{2}RT}{\sigma n^2 F^2 AC} \right)^2 \qquad (24)$$

where A is the area of the GCE = 0.071 cm^2, C is the concentration of Li-ions = 4.943 x 10^{-5}, 4.943 x 10^{-5}, 4.472 x 10^{-5} and 4.707 x 10^{-5} mol cm^{-3} for LFP-LMS HM, LFP-LMS-G HM, LFP-LMS SG and LFP-LMS-G SG, respectively. The obtained σ values from Z' vs $\omega^{-1/2}$ are shown in Fig. 44 and Table 10. The D_{app} for the graphenised LFP-LMS is higher than that of LFP-LMS hybrid cathode prepared via the hand milling method. However, graphenised LFP-LMS has a slightly lower D_{app} compared to LFP-LMS prepared via the *in situ* sol-gel method.

The slow diffusion of Li-ions in graphenised LFP-LMS might be caused by 1-D paths in the structure of LFP in the hybrid.

Table 10: Kinetic parameters of LFP-LMS HM, LFP-LMS-G HM, LFP-LMS SG and LFP-LMS-G SG obtained from EIS plots of these electrodes at 298.15 K

Cathode Material	$\sigma/\Omega\ s^{-1/2}$	$D_{app}/cm^2\ s^{-1}$
LFP-LMS HM	54196.24	2.450×10^{-13}
LFP-LMS-G HM	21380.71	1.574×10^{-12}
LFP-LMS SG	34129.80	7.547×10^{-13}
LFP-LMS-G SG	72038.91	1.529×10^{-13}

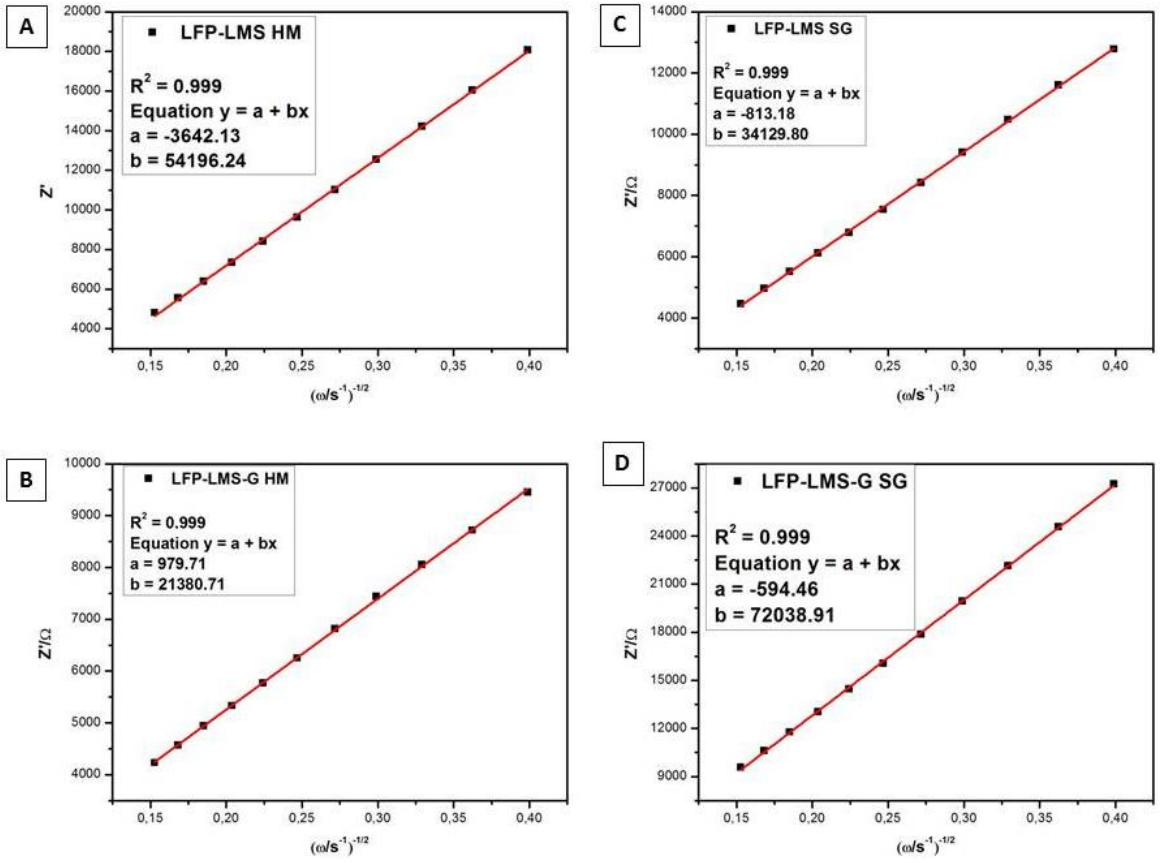

Figure 44: Z' vs $\omega^{-1/2}$ curves for (A) LFP-LMS HM, (B) LFP-LMS-G HM, (C) LFP-LMS SG and LFP-LMS-G SG

REFERENCES

1. Babbar, P., B. Tiwari, B. Purohit, A. Ivanishchev, A. Churikov, and A. Dixit, *Charge/discharge characteristics of Jahn–Teller distorted nanostructured orthorhombic and monoclinic Li_2MnSiO_4 cathode materials.* RSC Advances, 2017. **7**(37): p. 22990-22997.
2. Egerton, R.F., *Physical principles of electron microscopy: An introduction to TEM, SEM, and AEM*. 2005, 233 Spring Street, New York, NY 10013, United States of America: Springer Science + Business Media Inc. 202.
3. Chen, R., T. Zhao, X. Zhang, L. Li, and F. Wu, *Advanced cathode materials for lithium-ion batteries using nanoarchitectonics.* Nanoscale Horizons, 2016. **1**(6): p. 423-444.
4. Schnablegger, H. and Y. Singh, *The SAXS guide: Getting acquainted with the principles*. 3rd ed. 2011, A-8054 Graz, Austria: Austria: Anton Paar GmbH. 122.
5. Li, T., A.J. Senesi, and B. Lee, *Small angle X-ray scattering for nanoparticle research.* Chemical reviews, 2016. **116**(18): p. 11128-11180.
6. Ramachandran, R., M. Saranya, V. Velmurugan, B.P. Raghupathy, S.K. Jeong, and A.N. Grace, *Effect of reducing agent on graphene synthesis and its influence on charge storage towards supercapacitor applications.* Applied Energy, 2015. **153**: p. 22-31.
7. Miao, C., P. Bai, Q. Jiang, S. Sun, and X. Wang, *A novel synthesis and characterization of $LiFePO_4$ and $LiFePO_4$/C as a cathode material for lithium-ion battery.* Journal of Power Sources, 2014. **246**: p. 232-238.
8. Mohan, E.H., V. Siddhartha, R. Gopalan, T.N. Rao, and D. Rangappa, *Urea and sucrose assisted combustion synthesis of $LiFePO_4$/C nano-powder for lithium-ion battery cathode application.* AIMS Materials Science, 2014. **1**(4): p. 191-201.
9. Luo, S., M. Wang, and W. Sun, *Fabricated and improved electrochemical properties of Li_2MnSiO_4 cathodes by hydrothermal reaction for Li-ion batteries.* Ceramics International, 2012. **38**(5): p. 4325-4329.
10. Xie, M., R. Luo, R. Chen, F. Wu, T. Zhao, Q. Wang, and L. Li, *Template-Assisted Hydrothermal Synthesis of Li_2MnSiO_4 as a Cathode Material for Lithium Ion Batteries.* ACS applied materials & interfaces, 2015. **7**(20): p. 10779-10784.

11. Zaghib, K., A. Ait Salah, N. Ravet, A. Mauger, F. Gendron, and C.M. Julien, *Structural, magnetic and electrochemical properties of lithium iron orthosilicate.* Journal of Power Sources, 2006. **160**(2): p. 1381-1386.
12. Zhang, Z., X. Liu, L. Wang, Y. Wu, H. Zhao, and B. Chen, *Synthesis of Li_2FeSiO_4/C nanocomposite via a hydrothermal-assisted sol–gel process.* Solid State Ionics, 2015. **276**: p. 33-39.
13. Liu, Y., C. Cao, and J. Li, *Enhanced electrochemical performance of carbon nanospheres–$LiFePO_4$ composite by PEG based sol–gel synthesis.* Electrochimica Acta, 2010. **55**(12): p. 3921-3926.
14. Gong, H., H. Xue, T. Wang, and J. He, *In-situ synthesis of monodisperse micro-nanospherical $LiFePO_4$/carbon cathode composites for lithium-ion batteries.* Journal of Power Sources, 2016. **318**: p. 220-227.
15. Gao, M., N. Liu, Z. Li, W. Wang, C. Li, H. Zhang, Y. Chen, Z. Yu, and Y. Huang, *A gelatin-based sol–gel procedure to synthesize the $LiFePO_4$/C nanocomposite for lithium ion batteries.* Solid State Ionics, 2014. **258**: p. 8-12.
16. Kim, J.-K., J.-W. Choi, G.S. Chauhan, J.-H. Ahn, G.-C. Hwang, J.-B. Choi, and H.-J. Ahn, *Enhancement of electrochemical performance of lithium iron phosphate by controlled sol–gel synthesis.* Electrochimica Acta, 2008. **53**(28): p. 8258-8264.
17. Zhao, X., D.-H. Baek, J. Manuel, M.-Y. Heo, R. Yang, J.K. Ha, H.-S. Ryu, H.-J. Ahn, K.-W. Kim, and K.-K. Cho, *Electrochemical properties of magnesium doped $LiFePO_4$ cathode material prepared by sol–gel method.* Materials Research Bulletin, 2012. **47**(10): p. 2819-2822.
18. Tian, Z., Z. Zhou, S. Liu, F. Ye, and S. Yao, *Enhanced properties of olivine $LiFePO_4$/graphene co-doped with Nb^{5+} and Ti^{4+} by a sol–gel method.* Solid State Ionics, 2015. **278**: p. 186-191.
19. Wang, M., M. Yang, L. Ma, X. Shen, and X. Zhang, *Structural evolution and electrochemical performance of Li_2MnSiO_4/C nanocomposite as cathode material for li-ion batteries.* Journal of nanomaterials, 2014. **2014**: p. 4.
20. Belharouak, I., A. Abouimrane, and K. Amine, *Structural and electrochemical characterization of Li_2MnSiO_4 cathode material.* The Journal of Physical Chemistry C, 2009. **113**(48): p. 20733-20737.
21. Gummow, R.J. and Y. He, *Mesoporous manganese-deficient lithium manganese silicate cathodes for lithium-ion batteries.* RSC Advances, 2014. **4**(23): p. 11580-11584.

22. Dominko, R., M. Bele, A. Kokalj, M. Gaberscek, and J. Jamnik, *Li_2MnSiO_4 as a potential Li-battery cathode material.* Journal of Power Sources, 2007. **174**(2): p. 457-461.

23. Aravindan, V., K. Karthikeyan, S. Ravi, S. Amaresh, W.S. Kim, and Y.S. Lee, *Adipic acid assisted sol–gel synthesis of Li_2MnSiO_4 nanoparticles with improved lithium storage properties.* Journal of Materials Chemistry, 2010. **20**(35): p. 7340-7343.

24. Zhang, Q., Q. Zhuang, S. Xu, X. Qiu, Y. Cui, Y. Shi, and Y. Qiang, *Synthesis and characterization of pristine Li_2MnSiO_4 and Li_2MnSiO_4/C cathode materials for lithium ion batteries.* Ionics, 2012. **18**(5): p. 487-494.

25. Arroyo-deDompablo, M., R. Dominko, J. Gallardo-Amores, L. Dupont, G. Mali, H. Ehrenberg, J. Jamnik, and E. Moran, *On the energetic stability and electrochemistry of Li_2MnSiO_4 polymorphs.* Chemistry of Materials, 2008. **20**(17): p. 5574-5584.

26. Hwang, C., T. Kim, J. Shim, K. Kwak, K.M. Ok, and K.-K. Lee, *Fast ultrasound-assisted synthesis of Li_2MnSiO_4 nanoparticles for a lithium-ion battery.* Journal of Power Sources, 2015. **294**: p. 522-529.

27. Huang, Z., P. Luo, and D. Wang, *Preparation and characterization of core-shell structured $LiFePO_4$/C composite using a novel carbon source for lithium-ion battery cathode.* Journal of Physics and Chemistry of Solids, 2017. **102**: p. 115-120.

28. Jiang, J. and J.R. Dahn, *ARC studies of the thermal stability of three different cathode materials: $LiCoO_2$; $Li[Ni_{0.1}Co_{0.8}Mn_{0.1}]O_2$; and $LiFePO_4$, in $LiPF_6$ and LiBoB EC/DEC electrolytes.* Electrochemistry Communications, 2004. **6**(1): p. 39-43.

29. Hlongwa, N.W., *Nanoparticles-infused lithium manganese phosphate coated with magnesium-gold composite thin film-a possible novel material for lithium ion battery olivine cathode*. 2014, University of the Western Cape: Bellville, Cape Town, South Africa p. 90.

30. Ndipingwi, M.M., *Designing next generation high energy density lithium-ion battery with manganese orthosilicate-capped alumina nanofilm*. 2015, Universirty of the Western Cape: Bellville, Cape Town, South Africa. p. 109.

31. Ikpo, C.O., *Development of high performance composite lithium ion battery cathode systems with carbon nanotubes functionalised with bimetallic inorganic nanocrystal alloys*. 2011, University of Western Cape: Bellville, Cape Town, South Africa. p. 156.

32. Huang, X., J. Tu, C. Zhang, and J. Xiang, *Net-structured NiO–C nanocomposite as Li-intercalation electrode material.* Electrochemistry Communications, 2007. **9**(5): p. 1180-1184.

33. Hummers Jr, W.S. and R.E. Offeman, *Preparation of graphitic oxide.* Journal of the American Chemical Society, 1958. **80**(6): p. 1339-1339.
34. Shahriary, L. and A.A. Athawale, *Graphene oxide synthesized by using modified hummers approach.* Int. J. Renew. Energy Environ. Eng, 2014. **2**(01): p. 58-63.
35. Hanifah, M., J. Jaafar, M. Aziz, A. Ismail, M. Rahman, and M. Othman, *Synthesis of graphene oxide nanosheets via modified hummers' method and its physicochemical properties.* Jurnal Teknologi, 2015. **74**(1): p. 189-192.
36. Kellici, S., J. Acord, J. Ball, H.S. Reehal, D. Morgan, and B. Saha, *A single rapid route for the synthesis of reduced graphene oxide with antibacterial activities.* RSC Advances, 2014. **4**(29): p. 14858-14861.
37. Çiplak, Z., N. Yildiz, and A. Çalimli, *Investigation of graphene/Ag nanocomposites synthesis parameters for two different synthesis methods.* Fullerenes, Nanotubes and Carbon Nanostructures, 2015. **23**(4): p. 361-370.
38. Aslam, M., M. Kalyar, and Z. Raza, *Synthesis and structural characterization of separate graphene oxide and reduced graphene oxide nanosheets.* Materials Research Express, 2016. **3**(10): p. 105036.
39. Ren, P.-G., D.-X. Yan, X. Ji, T. Chen, and Z.-M. Li, *Temperature dependence of graphene oxide reduced by hydrazine hydrate.* Nanotechnology, 2010. **22**(5): p. 055705.
40. Wang, G., J. Yang, J. Park, X. Gou, B. Wang, H. Liu, and J. Yao, *Facile synthesis and characterization of graphene nanosheets.* The Journal of Physical Chemistry C, 2008. **112**(22): p. 8192-8195.
41. Yaragalla, S., A. Meera, N. Kalarikkal, and S. Thomas, *Chemistry associated with natural rubber–graphene nanocomposites and its effect on physical and structural properties.* Industrial Crops and Products, 2015. **74**: p. 792-802.
42. Haubner, K., J. Murawski, P. Olk, L.M. Eng, C. Ziegler, B. Adolphi, and E. Jaehne, *The route to functional graphene oxide.* ChemPhysChem, 2010. **11**(10): p. 2131-2139.
43. Miao, C., P. Bai, Q. Jiang, S. Sun, and X. Wang, *A novel synthesis and characterization of $LiFePO_4$ and $LiFePO_4$/C as a cathode material for lithium-ion battery.* Journal of Power Sources, 2014. **246**: p. 232-238.

CHAPTER 4

4. Conclusion and Recommendations

4.1. Conclusion

Blending of individual cathode materials has unique advantages over the use of a single cathode material in Li-ion battery applications. This study focused on the preparation and characterisation of graphenised lithium iron phosphate-lithium manganese silicate (LFP-LMS-G), and lithium iron phosphate-lithium manganese silicate (LFP-LMS) which were prepared using two different methods; hand milling and *in situ* sol-gel. The precursors for the hybrid cathodes; $LiFePO_4$ (LFP), Li_2MnSiO_4 (LMS) and graphene nanosheets were prepared and characterized using various analytical techniques in order to probe their chemical, electrochemical and physical properties.

Both pristine LFP and LMS cathode materials were prepared using the sol-gel approach and the obtained nanoparticles were spherical in shape with minimal agglomeration. These nanoparticles had an average size of 35 and 40 nm corresponding to LFP and LMS, respectively. The LFP had an orthorhombic structure with *Pmna* space group and also showed impurity phases of FeP, Fe_2P and Li_3PO_4. Similarly, the LMS also had an orthorhombic structure with P$mn2_1$ space group and a few impurities of Li_2SiO_3 and MnO which were confirmed using both XRD and FTIR. Furthermore, graphene nanosheets were successfully prepared using the modified Hummer's method. This was evidenced by the fewer number of layers observed in HRSEM and HRTEM images of graphene in comparison to those of graphene oxide. In addition, Raman studies revealed that most oxygen-containing group were removed during the reduction of graphene oxide, therefore successfully forming graphene. Thermal stabilities of these materials were also investigated using thermogravimetric analysis from room temperature to 900 ºC under N_2 atmosphere. It was found that graphene showed higher thermal stabilities attributed to only 38 % weight loss compared to 69 % weight loss for graphene oxide. These precursors were blended together using the two different methods to form LFP-LMS-G and LFP-LMS hybrid cathode materials.

Morphological studies revealed that the LFP-LMS-G had smaller particle sizes compared to LFP-LMS in both preparation methods, which is attributed to the presence of graphene

nanosheets during the preparation of these hybrid cathodes. However, LFP-LMS-G prepared via the hand milling approach showed bigger particles (30 ηm) than those prepared using the *in situ* sol-gel approach (23 ηm). This is because the *in situ* sol-gel approach offered better mixing and reaction conditions compared to the hand milling method where the precursors were mixed using a pestle and mortar in an open air environment. Thermogravimetric analysis of the prepared hybrid cathode materials revealed that both hybrid cathodes prepared via the *in situ* sol-gel method were more stable than those prepared using the hand milling method. Again, this further confirms the better mixing offered by this technique.

Electrochemical studies showed successful blending of the pristine cathode materials as evidenced by the presence of iron and manganese redox peaks in the cyclic voltammograms of the hybrid cathode materials. Even though the small contents of graphene were not picked up with XRD, FTIR and Raman spectroscopy the graphenised hybrid cathodes showed better electrochemical properties compared to those without graphene from both approaches. The calculated specific capacities were 4.056, 2.524, 3.408 and 2.804 mA h g^{-1} for LFP-LMS-G SG, LFP-LMS SG, LFP-LMS-G HM and LFP-LMS HM, respectively. These results confirm that the graphenised lithium iron phosphate-lithium manganese silicate hybrid cathode material prepared via *in situ* sol-gel method performed better than that those of the hand milling method. In conclusion, even though these hybrid cathode materials were developed for Li-ion battery applications electrochemical impedance spectroscopy studies revealed that they have a capacitive behaviour. This behaviour is shown by the presence of an inclined line without a semi-circle in the Nyquist plots of these hybrid cathodes.

4.2. Recommendations

This study looked at two different methods that can be used to prepare graphenised lithium iron phosphate-lithium manganese silicate and future works in this research could look at other preparation methods and check the properties and performance of the developed hybrid cathode materials. Furthermore, these studies can also focus on studying the different ratios of the $LiFePO_4$, Li_2MnSiO_4 and graphene that are used to prepare the hybrid cathode materials. Thereafter, the prepared hybrid cathode materials would be used to fabricate coin cells for further electrochemical interrogations.